

A Navigation System for an Ultrathin Scanning Fiber
Bronchoscope in the Peripheral Airways

Timothy Soper

A dissertation submitted in partial fulfillment
of the requirements for the degree of

Doctor of Philosophy

University of Washington

2009

Program Authorized to Offer Degree: Bioengineering

University of Washington
Graduate School

This is to certify that I have examined this copy of a doctoral dissertation by

Timothy Soper

and have found that it is complete and satisfactory in all respects,
and that any and all revisions required by the final
examining committee have been made.

Chair of the Supervisory Committee:

Eric J. Seibel

Reading Committee:

Eric J. Seibel

David R. Haynor

Paolo Vicini

Date:

In presenting this dissertation in partial fulfillment of the requirements for the Doctoral degree at the University of Washington, I agree that the Library shall make its copies freely available for inspection. I further agree that extensive copying of this dissertation is allowable only for scholarly purposes, consistent with "fair use" as prescribed in the U.S. Copyright Law. Requests for copying or reproduction of this dissertation may be referred to Bell and Howell Information and Learning, 300 North Zeeb Road, Ann Arbor, MI 48106-1346, to whom the author has granted "the right to reproduce and sell (a) copies of the manuscript in microform and/or (b) printed copies of the manuscript made from microform."

Signature_____

Date_____

University of Washington

Abstract

A Navigation System for an Ultrathin Scanning Fiber Bronchoscope in the Peripheral Airways

by Timothy Soper

Chair of the Supervisory Committee:

Professor Eric J. Seibel
Mechanical Engineering

Transbronchial biopsy of peripheral lung nodules is hindered by inability to access lesions endobronchially due to the large diameter of conventional bronchoscopes. An ultrathin scanning fiber endoscope (SFE) has recently been developed to advance image-guided biopsy several branching generations deeper into the peripheral airways. With this new technology, high-resolution, full-color images can be acquired at video frames rates from within the small peripheral airways that extend out to these peripheral nodules. However, navigating a potentially complex 3D path to the region of interest presents a significant challenge to the bronchoscopist, whose working knowledge of the airway anatomy is limited to the more central lung. To promote minimally invasive and accurate biopsy of peripheral nodules using this new device, a guidance system was developed to track the SFE within the airway anatomy and direct the bronchoscopist to region of interest via a user interface. Assisted navigation is broken into preoperative and intraoperative stages. From a preoperative planning session, the bronchoscopist identifies the lesion location and defines a path to navigate to the desired biopsy site. During bronchoscopy, an electromagnetic sensor tracks the position and pose of the SFE, which is displayed on the preoperative CT image. At each bifurcation, the predefined path directs the bronchoscopist to the region of interest

where biopsy is performed. This dissertation outlines the guidance system development and its validation in live animal experiments. First, image analysis software was developed to construct a virtual airway model from CT image data, providing an anatomical map. Assisted navigation was tested using electromagnetic tracking (EMT) within a rigid airway model. In considering future navigation within a live subject, an analysis of airway deformation was performed. Lung motion due to breathing was quantified and modeled using deformable registration of multiple CT scans acquired at various levels of lung inflation. In conjunction with EMT-based localization, image-based tracking (IBT) also permitted localization of the SFE by registration between real and virtual bronchoscopic images. Ultimately, a hybrid tracking strategy was adopted by combining EMT and IBT tracking. At each video frame, the position of the SFE is approximated by the position sensor and then optimized using the video images themselves to reconcile localization errors introduced by EMT system registration and deformation of the anatomy. The hybrid tracking system presented in this dissertation is a novel approach to SFE localization within peripheral airways. As part of this strategy, a means of respiratory motion compensation is integrated to account for large excursions undergone by peripheral lung regions during breathing. Preliminary *in vivo* swine studies verify that the SFE can be adequately tracked within peripheral airways, providing guidance that is crucial for navigation and biopsy of peripheral lesions. The greater clinical impact of a trackable SFE may be earlier and more accurate diagnosis of peripheral lesions, resulting in reduced financial cost and compromise to patient health.

TABLE OF CONTENTS

List of Figures	v
List of Tables	ix
Chapter 1: Introduction	1
1.1 Significance	1
1.2 Statement of Aims	3
1.3 Dissertation Overview	4
Chapter 2: Background	7
2.1 Clinical Management of SPNs	9
2.1.1 CT Surveillance	10
2.1.2 PET Imaging	10
2.1.3 Tissue Biopsy	11
2.1.4 Bronchoscopy in the Diagnosis of Small, Peripheral SPNs	14
2.2 The Scanning Fiber Endoscope	15
2.2.1 SFE Distal Tip Components	15
2.2.2 The Complete SFE System	16
2.2.3 Advantages of SFE for Evaluation of SPNs	17
2.3 Bronchoscopic Navigation	19
2.3.1 Radiological Imaging	20
2.3.2 Subsurface Interrogation	21
2.3.3 Electromagnetic Tracking	22

2.3.4	Virtual Guidance	23
2.4	A Navigation System for SFE in Peripheral Airways	24
Chapter 3:	Construction of a Virtual Airway Model	26
3.1	Airway Segmentation	26
3.1.1	Background	26
3.1.2	Methods	30
3.1.3	Results	38
3.2	Virtual Surface Generation	38
3.3	Centerline Analysis	41
3.3.1	Methods	43
3.4	Discussion	49
Chapter 4:	User Interface Design	52
4.1	Preoperative Planning	52
4.1.1	Image Interaction	55
4.1.2	Manual Segmentation	55
4.1.3	Path Definition	56
4.2	Discussion	58
Chapter 5:	Electromagnetic Navigation within a Rigid Lung Model	61
5.1	Background	61
5.2	Evaluation of EMT Accuracy	62
5.2.1	Results	64
5.3	Navigation of a Dried Sheep Lung	65
5.3.1	Results	65
5.4	Discussion	67

Chapter 6:	Modeling Respiratory Motion	69
6.1	Mechanics of Respiration	70
6.2	Non-rigid Registration	72
6.2.1	Optical Flow and the Demons Algorithm	73
6.3	Experimental Methods	76
6.3.1	Image Acquisition	76
6.3.2	Deformable Registration Framework	76
6.3.3	Experimental Variants	79
6.4	Results	80
6.4.1	Registration Parameter Optimization	80
6.4.2	Measuring Deformation	83
6.4.3	Modeling Lung Deformation	84
6.5	Discussion	90
Chapter 7:	Image-Based Guidance	93
7.1	Background	94
7.2	Camera Calibration	95
7.2.1	Methods	97
7.2.2	Results	98
7.3	Video Preprocessing	100
7.3.1	Frame Rejection	102
7.4	Similarity Metrics	103
7.4.1	Optimization	108
7.4.2	Light Source Calibration	109
7.5	Simulated Tracking of <i>In-Vivo</i> Video Images in Swine	111
7.5.1	Simulation Framework	112
7.5.2	Evaluation of Simulated Tracking Accuracy	112

7.5.3	Results	113
7.6	Conclusions	117
7.7	Discussion	117
7.7.1	Study Limitations	118
Chapter 8:	Hybrid Tracking	121
8.1	SFE-EMT System Registration	122
8.1.1	Results	125
8.2	CT Image – World Registration	127
8.3	Hybrid Tracking Model	129
8.3.1	The Kalman Filter	130
8.3.2	Hybrid Tracking Using an Error-State Kalman Filter	132
8.4	Respiratory Motion Compensation	133
8.4.1	Computing Respiratory Phase	135
8.4.2	Results	136
8.5	Conclusions	140
Chapter 9:	Conclusions and Future Work	147
9.1	Future Work	149
9.1.1	Image Analysis and Path-Planning Software	150
9.1.2	Real Time Tracking	151
9.1.3	Intraoperative Guidance	153
9.1.4	Distortion correction	154
9.1.5	SFE Design	155
Bibliography		161

LIST OF FIGURES

2.1	CT slice containing a peripheral solitary pulmonary nodule.	8
2.2	Flexible bronchoscopy in the diagnosis of a solitary pulmonary nodule. . .	12
2.3	Functional schematic of the scanning fiber endoscope distal tip.	17
2.4	Input voltage signal used to generate the spiral scan pattern.	18
2.5	The complete SFE system.	18
3.1	The processing pipeline for preoperative MDCT.	27
3.2	Block diagram of the adaptive 3D region growing segmentation stage. . . .	34
3.3	Results of adaptive 3D region growing.	34
3.4	A 1D example of grayscale reconstruction of an airway.	36
3.5	Bank of morphological reconstruction kernels of various radii.	38
3.6	Morphological analysis of airway regions.	39
3.7	Final segmentation results for four different chest CT scans.	40
3.8	Bronchoscopic video frames and corresponding virtual reconstructions using various degrees of surface smoothing.	42
3.9	Detection of endpoints in the segmented airway tree.	45
3.10	Examples of airway centerline extraction techniques.	46
3.11	Example of a B-spline	48
3.12	B-Spline approximation of the airway centerlines	49
4.1	The preoperative planning utility after loading the CT image of a patient. . .	54
4.2	Selection of a 3D path to an identified nodule.	57
4.3	Manual path extension to reach an peripheral lesion.	58

4.4	A maximum intensity projection image of the distance map of every part of the lung to the nearest identified airway.	60
5.1	The 3D Guidance medSAFE system (Ascension Technology Corporation, Burlington, VT)	63
5.2	The EMT accuracy is measured by FLE using a tracked stylus.	65
5.3	The dried (rigid) sheep lung model encased in a plexiglass box (a) and localization of the sensor slot on a slice of the acquire CT image (b)	66
5.4	Tracking session within the rigid lung model.	67
6.1	Respiratory physiology and the muscles involved in inspiration and expiration.	71
6.2	Radiographic outlines of a lung at various volumes.	72
6.3	A 1D example illustrating the optical flow between a fixed image F and moving image G	75
6.4	The deformable demons registration framework.	77
6.5	Preprocessing of the fixed and moving images prior to deformable registration.	78
6.6	Inverse and transitive registration errors with and without histogram matching and symmetric demons forces.	83
6.7	Inverse and transitive registration error as a function of the degree of smoothing.	84
6.8	Registration result of the fixed and moving images	85
6.9	Slices of the center lung depict the deformation \vec{U}_{max} between images E_1 and A_1	86
6.10	The mean value of the intrinsic phase ϕ is computed for each deformation field.	87

6.11	The mean model prediction error of each deformation field \vec{U}_ϕ	88
6.12	Surface renderings of the airways compare the predicted and computed deformations at an intermediate respiratory phase.	90
7.1	Example of CT-video Registration from a conventional PENTAX bronchoscope (EB-1970K).	94
7.2	A diagram of the camera, world, and pixel coordinate spaces.	97
7.3	Landmark detection and distortion correction of an SFE calibration frame.	99
7.4	Diagram of point light source illumination of a surface point coincident with a pinhole camera	102
7.5	Preprocessing stages of SFE video images	103
7.6	Rejection of obscured video images is denoted by a red outline in select frame sequences.	104
7.7	Differential surface analysis of real and virtual bronchoscopic images.	107
7.8	Plot of IBT of the SFE during session 1 of a live pig experiment	115
7.9	Example of divergent tracking resulting from large interframe motion.	116
7.10	Collage of CT-video registration results at selected frames using each of the similarity metrics.	116
8.1	The sensor-mounted distal SFE tip and free-hand calibration diagram.	125
8.2	The results of SFE-EMT registration are shown from two separate free-hand calibration procedures.	127
8.3	Localization of corresponding landmarks in both real and virtual anatomies is the basis of registration between world and CT image coordinates.	128
8.4	World to CT image rigid point registration is performed using corresponding landmarks.	129

8.5	Registration error between the real anatomy (<i>black</i>) and the virtual anatomy (<i>gray</i>) is modeled by a secular error δ	130
8.6	Hybrid tracking strategy using respiratory motion compensation.	136
8.7	Computing respiratory phase ϕ from an externally mounted position sensor.	137
8.8	Hybrid tracking results compared to independent EMT and IBT for sessions 1-3	142
8.9	Hybrid tracking results compared to independent EMT and IBT for session 4	143
8.10	Hybrid tracking results with and without RMC for sessions 1-3	144
8.11	Hybrid tracking results with and without RMC for session 4	145
8.12	Hybrid z -axis tracking results are plotted over frames at the end of session 4 within peripheral airways using all three methods.	145
8.13	Selected frames illustrate the localization accuracy using each of the hybrid tracking methods.	146
8.14	Comparison of the airway deformation U computed from the Kalman filter and the deformation $\vec{U}_{max}(x_I)$ acquired from deformable registration of CT images over the SFE path.	146
9.1	A simulated intraoperative guidance interface.	157
9.2	Nonparametric distortion correction procedure.	158
9.3	Example SFE images before and after nonparametric distortion correction.	159
9.4	Demonstration of the first generation tip-bending mechanism.	159
9.5	The new 0.30 mm 5 DoF Ascension sensor	160

LIST OF TABLES

2.1	Number of airways and average airway diameter for each branching generation.	19
3.1	Processing times for the individual processing stages given a CT image with 0.5 mm resolution and a volume of $228 \times 206 \times 486$	51
6.1	Mean lung displacements (in mm) computed between the baseline CT scan at full inspiration and scans taken over the entire respiratory cycle.	84
6.2	Prediction error (in mm) of the linear lung motion model for each CT scan acquired.	89
7.1	Intrinsic camera parameters of the SFE and EB-1970K bronchoscope.	100
7.2	RMS Positional and orientational tracking error E^{key} between IBT output and manually registered key frames.	114
7.3	Number of tracking failures experienced during each tracking session using each of the three similarity metrics.	114
8.1	The translation t_{sc} , rotation angles θ_{sc} , and mean registration errors E_x and E_θ are provided for two SFE-EMT registration procedures.	126
8.2	Average statistics for each of the SFE tracking methodologies.	139

LIST OF ABBREVIATIONS

CCD	charge-coupled device
CT	computed tomography
DoF	degrees of freedom
dwNMI	dark-weighted normalized mutual information
EBUS	endobronchial ultrasound
EMT	electromagnetic tracking
FB	flexible bronchoscopy
FDG	fluorodeoxyglucose
FLE	fiducial localization error
FRC	functional residual capacity
FRE	fiducial registration error
HU	Hounsfield Units
IBT	image-based tracking
ITK	Image Segmentation and Registration Toolkit
MDCT	multi-detector computed tomography
mwSGA	magnitude-weighted surface gradient alignment
NMI	normalized mutual information
PET	positron emission tomography
RV	residual volume
SFE	scanning-fiber endoscope

SGA surface gradient alignment
TBB transbronchial biopsy
TRE target registration error
TTNA transthoracic needle aspiration
VATS video-assisted thoracoscopic surgery
VTK Visualization Toolkit

ACKNOWLEDGMENTS

First, I would like to sincerely thank my advisor, Dr. Eric Seibel, for his role in supporting and encouraging this research. Throughout my graduate career, he has participated whole-heartedly in all aspects of this project and has always lent a hand and provided much needed encouragement at daunting points along the way. He is, in every way, in stark contrast to the proverbial "absentee advisor." While he has certainly contributed to my professional and academic development, I am most impressed with the personal investment he makes in his students. Eric has always made time for impromptu meetings and maintains an open-door policy (actually a no-door policy). As our lab director, he has continually put others needs above his own and has always led by example. Throughout my time in graduate school, I have seen Eric engage myself and others in the lab in ways that were above and beyond the status quo. He has worked until early morning hours preparing and cleaning the CT room as part of my pig experiments, he has taken all of us out to dinner on several occasions, offered up free use of his cabin, and even provided his expert goalie services as part of a lab soccer team. Even here, though most would refer to an advisor by title, I prefer to use his first name as it reflects the personal rapport he has maintained with us as members in the lab. Outside the office, I've witnessed Eric apply the same level of dedication, patience, and humility in raising a family. In this regard, I consider him, not only as an advisor, but as someone I would gladly emulate in all aspects of life.

Second, I would like to sincerely thank Dr. David Haynor for his support in this project. Dr. Haynor contributed significantly to the intellectual novelty and gave a direct hand in advising me on many of the technical aspects of this research. I have had the privilege of meeting with Dr. Haynor in coffee shops strewn all over Seattle to discuss a number of

topics. He provided essential insights into the mathematical formulation of our bronchoscopic guidance system. But he also supported this project in ways that went far beyond the academic realm. He too was present for a number of late-night animal experiments during which he was asked to come to the hospital at a moments notice. When experimental CT scanning was nearly terminated by the hospital administration, Dr. Haynor went to bat for us to ensure this project could continue. Without doubt, the outcome of this research is directly owing to Dr. Haynor's contributions.

A debt of gratitude is also owed to a number of lab members and collaborators who helped me along the way. First, none of this work could have been completed without the hard work and dedication of the engineering staff. The efforts of Rich Johnston, David Melville, and Cameron Lee provided me with a truly amazing piece of technology in the scanning fiber endoscope. Although many of my requests were no doubt hassles, all three were always very accommodating. I even received sympathy after breaking a probe during a demonstration, though some moderate level of penance was offered in the form of mopping the lab floor; a one-time tradition that has yet to be enacted, though it is still often referred to in jest. This group has also spent countless hours advising me on how to use the endoscope and to help me understand how it worked. Rich has always been available for "white board" time, to carefully explain the science behind our technology.

Wayne Lamm, our animal technician, was extremely helpful for each of the pig experiments. He coordinated all of the animal work and assisted me with each of the bronchoscopies, often late into the night. He often found practical solutions to problems using our scope in a live animal. I am also very thankful for the assistance of Robb Glenny and Susan Bernard who were present for many of the experiments and were critical in formalizing the experimental protocols. I would also like to thank Mario Ramos, our helpful CT technician, who made scheduling experiments extremely easy and convenient.

I am extremely thankful for the support of my family over my years of study. My

wife, Jennifer, whom I met in my third year, has encouraged me and supported me for many years: even during periods of more intensive work, when I'm sure I had a less than pleasant disposition. Her patience, willingness to listen, and ability to keep me grounded contributed significantly to my progress as a graduate student and helped me to maintain a level of sanity during stressful times. I am truly blessed to have her in my life. My parents have also been a source of continual support and encouragement. I will forever appreciate their interest and involvement in all aspects of my life. They have always been there for me, and for that I will always be grateful. I will always remember my dad helping me to build a wooden transport tray for pigs after a Thanksgiving dinner.

Finally, I give glory to God and to Jesus Christ from whom all things are given. My time in graduate school has taught me a number of things, and though I am older, and hopefully wiser, I still yearn for wisdom, knowledge, and love that is beyond the things of this world.

“No eye has seen,
no ear has heard,
no mind has conceived,
what God has prepared for those who love Him”
– but God has revealed it to us by His Spirit.

1 Corinthians 2:9-10

DEDICATION

To Booger

Chapter 1

INTRODUCTION

1.1 Significance

Computed tomography (CT) scans report a high incidence of pulmonary nodules within the peripheral lungs of patients suspected of having lung cancer. Positive diagnosis of these lesions and future therapeutic planning requires histological analysis of representative tissue. When possible, bronchoscopy is the preferred method by which to biopsy the identified nodules as it is most minimally invasive. Bronchoscopy involves inspection of the internal airway surface via the insertion of a flexible endoscope, or bronchoscope through the trachea and into the affected lung. Tissue samples are then collected by inserting a biopsy tool such as a cytological brush, biopsy needle, or forceps down the hollow working channel of the bronchoscope.

Unfortunately, peripheral airways are often too small to accommodate the diameter of conventional bronchoscopes (~ 5 mm OD). At this size, bronchoscopes are typically limited to the first four airway generations at most, amounting to roughly 2^4 or 16 airways. Many nodules fall outside this accessible airway space and thus force the bronchoscopist to acquire lung tissue blindly by extending the biopsy tools further into the lung, beyond the view of the bronchoscope's distal tip. Multiple samples must be obtained and there is little certainty that tissue is acquired from the lesion or that it is more broadly indicative of any underlying pathology. As a result, bronchoscopic findings are often inconclusive and other, more invasive diagnostic measures, such as transthoracic needle aspiration must be

considered.

Our laboratory has recently constructed an ultrathin (~ 1.6 mm) scanning-fiber endoscope (SFE) that can be extended further into the peripheral lung where pulmonary nodules are common (10 branching generations). This offers a more minimally invasive means of biopsying lesions in patients that would otherwise require further observation or more invasive staging procedures. However, despite the fact that this technology can navigate small peripheral airways, the branching at this level is exponentially more complex. Ten generations of airway branching amounts to a potential total of 2^{10} or 1,024 airways. Unlike in the central lung where limited branching and relative anatomical homogeneity make maneuvering of the bronchoscope quite simple, the extensive branching and tortuous geometry of the peripheral airways present a significant obstacle to the bronchoscopist who must navigate the SFE out to distal regions of the lung. To promote biopsy of peripheral lung lesions using the SFE, the goal of this research is to provide a means bronchoscopic guidance, both to navigate to a region of interest as well as to accurately target a lesion potentially smaller than 1 cm in size.

The guidance system developed in this work consists of the SFE, an electromagnetic position sensor mounted to the SFE distal tip, and a virtual user interface. Prior to bronchoscopy, image analysis software automatically segments the airways from the preoperative CT and generates a virtual model of the airways. A preoperative planning utility allows the bronchoscopist to locate a target lesion and define a 3D path leading to the site. During bronchoscopy, the electromagnetic sensor tracks the position of the SFE as it maneuvers through multiple generations of airway branching. The location of the SFE is mapped onto a display of the preoperative CT image and virtual airway model as a means of directing the bronchoscopist as well as permitting visualization of subsurface structures relative to the prescribed SFE location. However, due to tracking error and deformation of the airway anatomy, registration between the electromagnetic tracking system and the preoperative CT image is imprecise. To improve intraoperative localization and subsequent guidance of the SFE, image-based guidance was incorporated by matching a virtual bronchoscopic view

to each frame of the real bronchoscopic video. A model of respiratory motion was finally added which further improved tracking accuracy in breathing airways.

Construction of this guidance system poses many engineering challenges. First, a number of image processing schemes are required for conversion of CT image data to a virtual anatomical model of the airways. This further requires that a graphical user interface (GUI) be designed to permit interaction with the CT image and its virtual reconstructions. During bronchoscopy, the intraoperative tracking of the SFE through the airway anatomy requires precise registration between the physical SFE position as measured by the electromagnetic sensor and the CT coordinates in which the virtual airway map is defined. Within a live subject, the guidance system must compensate for misalignment between the real and virtual CT anatomies caused by respiratory motion. Given this set of design criteria, a set of three specific aims are defined as essential research components in the construction of a bronchoscopic guidance system.

1.2 Statement of Aims

Specific Aim 1:

Develop software components for both image analysis of preoperative CT scans as well as a graphical user interface for path planning and intraoperative guidance. As part of image analysis, it is necessary to demonstrate robust automated segmentation of the airways down to the diameter of the SFE and subsequent modeling of both the airway surfaces and centerlines. The path planning software is used to demonstrate virtual interaction with the derived airway model to define a target lesion and a 3D path leading to the region beginning from the trachea.

Specific Aim 2:

Quantify and model the registration error introduced by respiratory motion of the lung. Accurate measurement of the airway displacements is critical for evaluating tracking errors

and determining biopsy accuracy. Modeling of the lung deformation presents an avenue for motion compensation to reduce registration error caused by breathing. Here, we care to show that recovery of this error is possible down to the size of a small nodule (5 mm).

Specific Aim 3:

Develop and perform *in vivo* validation of combined electromagnetic and image-based tracking of the SFE within peripheral airways under normal breathing conditions. The tracking system is ultimately validated through demonstration of stable and accurate localization of the SFE over an entire bronchoscopy within a live animal under normal breathing conditions.

1.3 Dissertation Overview

A general overview of each chapter in the dissertation is given below:

In Chapter 2, the clinical management of lung cancer and pulmonary lesions is reviewed. Relevant background of flexible bronchoscopy is given with regard to present diagnostic yield and performance limitations in biopsy of peripheral lesions as a result a large overall diameter. A novel ultrathin scanning fiber endoscope is introduced for potential biopsy and intervention of peripheral lung nodules. A general groundwork is laid for current techniques in bronchoscopic tracking and specific challenges relevant to guidance of the SFE are outlined.

In Chapter 3, image processing techniques are presented for extraction of a virtual airway model from a preoperative CT. Among the processing steps discussed are airway segmentation, virtual surface generation, and centerline analysis. Algorithmic modifications to past work are described and results from scans of both human and porcine CT data sets are presented.

In Chapter 4, the guidance user interface is presented. Features of a preoperative planning utility illustrate how the bronchoscopist can visualize and interact with the virtual

airway model and plot a route through the airways to a prescribed region of interest. During bronchoscopy the guidance utility tracks and displays the position of the bronchoscope on the virtual model while a highlighted path directs steering of the SFE at each bifurcation.

In Chapter 5, an electromagnetic tracking system is used for real time localization during bronchoscopy. Techniques for characterizing tracking accuracy and registration performance are described. Initial experiments are performed to test localization accuracy within a rigid lung model.

In Chapter 6, we quantify the registration error between the real and virtual airways as a result of breathing. First a deformable registration framework was developed to calculate deformation between CT images at various phases of respiration. To help mitigate registration error due to breathing, a model of respiratory motion was constructed and validated using the acquired CT images.

In Chapter 7, a number of image-based tracking algorithms were tested on video sequences of the airways using the SFE. A video preprocessing pipeline was first developed to account for eccentricities in the images acquired by the SFE. Tracking performance was evaluated for a number of similarity metrics that were used to align the virtual bronchoscopic perspective with acquired video frames. A new similarity metric is presented, using differential surface analysis, that improves robustness of image-based tracking.

In Chapter 8, a new hybrid tracking strategy is proposed, which combines electromagnetic and image-based tracking. To begin, a robust and convenient free-hand calibration technique was devised to register the SFE and electromagnetic tracking system. Following, intraoperative localization of the SFE was evaluated using a number of simulated tracking scenarios using recorded bronchoscopic video and sensor data. The tracking error between the EMT sensor and image-based tracking outputs were modeled using an error-state Kalman filter. Respiratory motion compensation was achieved by including an estimate of the respiratory phase acquired from an abdominally mounted position sensor. Tracking results using the improved hybrid approach are presented.

In Chapter 9, conclusions of this dissertation are presented and future work is recom-

mended for both the SFE and guidance system that is critical to clinical translation of this technology.

Chapter 2

BACKGROUND

Lung cancer is the leading cause of all cancer related deaths. The survival rate following diagnosis is less than 15% after 5 years [128] and in 2008, over 166,000 people are estimated to have died from respiratory cancers in the U.S. alone. This poor prognosis is attributed to the fact that cancer progression is likely to be extensive by the time a patient develops symptoms. Because earlier detection of lung cancer is associated with improved patient outcomes [53], lung cancer screening has garnered considerable interest. Currently, multi-detector CT (MDCT) is the clinically established standard for screening of lung cancer. MDCT of the chest provides detailed three-dimensional radiographic imaging of the lung anatomy and pathology with sub-millimeter resolution. In patients considered high-risk for lung cancer, MDCT reveals a high incidence of potentially cancerous solitary pulmonary nodules (SPNs) which are ≤ 3 cm in diameter (Figure 2.1). Ultimate determination of SPN malignancy requires histological analysis of representative tissue. Biopsy procedures are considered to be invasive and require careful consideration of the diagnostic accuracy, risk of morbidity, and clinical cost.

When possible, bronchoscopic biopsy is the preferred method for acquiring tissue because it is more minimally invasive. However, a number of these SPNs are small (< 10 mm) and located within the peripheral lung, making them difficult or impossible to access bronchoscopically. These lesions pose a diagnostic predicament: whether to forego intervention or pursue a more invasive staging strategy. Our laboratory at the University of Washington has developed an ultrathin scanning fiber endoscope (SFE) that is small enough to extend into peripheral airways where these SPNs occur. While this is encourag-



Figure 2.1: CT slice containing a peripheral solitary pulmonary nodule.

ing for early diagnosis of lung cancer, it poses as difficult challenge to the bronchoscopist who must correctly navigate a tortuous route through several airway generations to reach an SPN that may or may not be endoluminally visible. As part of this new technology, a bronchoscopic guidance system is being developed to assist in navigating the complex airway anatomy by fusing preoperative CT images with bronchoscopic video.

In this chapter, limitations in the clinical management of SPNs are described and the novel SFE technology is presented with an analysis of its potential impact on earlier diagnosis of SPNs. Following, we present our arguments for the need of assisted navigation of the SFE as part of a complete clinical system, and discuss previous work in this field. Finally, we list the essential components for bronchoscopic guidance of the SFE and outline the specific stages of research and development contained in this dissertation.

2.1 Clinical Management of SPNs

Effective management of SPNs requires an assessment of the likelihood of malignance. Factors considered in the evaluation include both clinical pretest findings and radiological features: most notably, history of smoking, age, SPN diameter, and edge characteristics [40, 45]. Probability of malignance increases significantly with increasing cigarette use and increasing age. It is also well known that a malignant diagnosis is associated with a larger SPN diameter. Lesions > 3 cm in diameter, formally defined as pulmonary masses, carry a more than 90% probability of malignance and necessitate immediate resection [174]. However, for small nodules, < 1 cm in diameter, the estimated prevalence of lung cancer varies dramatically between studies [38, 72, 173, 53, 4].

For SPNs of a more intermediate size, a number radiographic features are used to persuade future staging, including edge characteristics [174, 33, 121], calcification, and overall density [52]. For malignant SPNs relevant features include spiculated edges, non-calcified pattern, and an increase in tissue density. Alternatively, non-cancerous etiologies are differentiated by a smooth lesion boundary and lower attenuation values. The presence of calcification in the lesion is often evident of inflammation. Contrast enhancement can also help establish malignance as evidenced by higher attenuation values which result from increased tumor vascularization.

Overall, following initial detection by MDCT, SPNs are most likely considered to be indeterminate and require further workup by continued CT surveillance, positron emission tomography (PET), biopsy, or surgical resection. These specific staging strategies and the overall aggressiveness in obtaining a definitive diagnosis should weigh suspicion of malignance and a potential life-saving resection against the compromise to patient health and expense. In an effort to streamline management of SPNs, clinical algorithms for staging have been proposed [91].

2.1.1 CT Surveillance

For patients in whom an SPN is largely indeterminate, periodic follow-up by MDCT provides a noninvasive means of tracking tumor growth, a well-established metric for differentiating benign and malignant etiologies [159, 171]. Surveillance is primarily advisable in cases where clinical and radiological features are indicative of non-cancer or if the nodule is considered too small to biopsy (< 10 mm). Frequency of follow-up MDCT is typically spaced at annual, semi-annual, or quarterly intervals. SPNs demonstrating little or no distinguishable growth over a 2 year period are considered benign and require no further workup. For lesions exhibiting discernible growth, volumetric doubling times are useful in distinguishing lung cancer from other causes of SPNs including granulomatous and inflammation [159]. Surveillance continues until the lesion is at least 1 cm in diameter at which point more aggressive staging techniques are considered.

2.1.2 PET Imaging

PET scanning is an ancillary imaging modality that further characterizes functional aspects of SPNs, complimentary to the structural attributes resolved by MDCT. Specifically, the metabolic uptake of the glucose analogue 18F-Fluorodeoxyglucose (FDG) can be used to differentiate between malignant and benign tumors with a high sensitivity and specificity [44, 15]. A positive PET scan is commensurate with a 90% likelihood of malignance. This is particularly useful in cases where the clinical pretest factors and radiological features infer contradictory diagnoses [41]. However, for very small SPNs (< 10mm) FDG-PET suffers from a high incidence of false positives, often the result of sarcoidosis or alternative cause of inflammation. For these nodules, intervention is relegated to continued CT surveillance.

2.1.3 Tissue Biopsy

In cases where malignance is highly suspect, biopsy of the lesion can provide a more definitive diagnosis, particularly in the event lung cancer is discovered. Biopsies are primarily acquired by one of three methods: flexible bronchoscopy (FB), transthoracic needle aspiration (TTNA), or surgical resection. Choice of biopsy procedure is contingent on lesion size, location in the lung (peripheral or central), availability of hospital resources, and experience of the attending physician. Given the large number of factors involved, summarizing the efficacy of a given biopsy method is complicated and highly variable. Below, a general overview of these methods are given from a broad clinical perspective along with current limitations of each procedure.

2.1.3.1 Flexible Bronchoscopy

FB involves the insertion of a flexible, steerable shaft into the airways through an oral or nasal route. The endoluminal surface of the airways is viewed by the bronchoscopist using an encapsulated fiber-optic bundle or CCD array. In Figure 2.2, a bronchoscopist navigates using video displayed on a nearby monitor as captured by the internal CCD camera. Once the bronchoscope reaches the lesion as evident from endoluminal video or radiological verification, a biopsy tool such as forceps, cytological brush, or needle is fed through the working channel to obtain a tissue specimen by transbronchial biopsy (TBB). In the case of FB, diagnostic yield depends heavily on the nodule size, location in the lung, endoluminal apparency, and number of samples acquired. For SPNs situated in the peripheral lung, the diameter of the bronchoscope (~5 mm) is often too large to access the peripheral airways adjacent to the lesion. As a result, biopsies must be taken blindly or under the aid of fluoroscopy. While the overall sensitivity of FB is 88%, the sensitivity for peripheral lesions is only 69%, and only 33% for SPNs < 2 cm in diameter [115]. Given these limitations, bronchoscopy is rarely performed in patients presenting with a small, peripheral SPN.

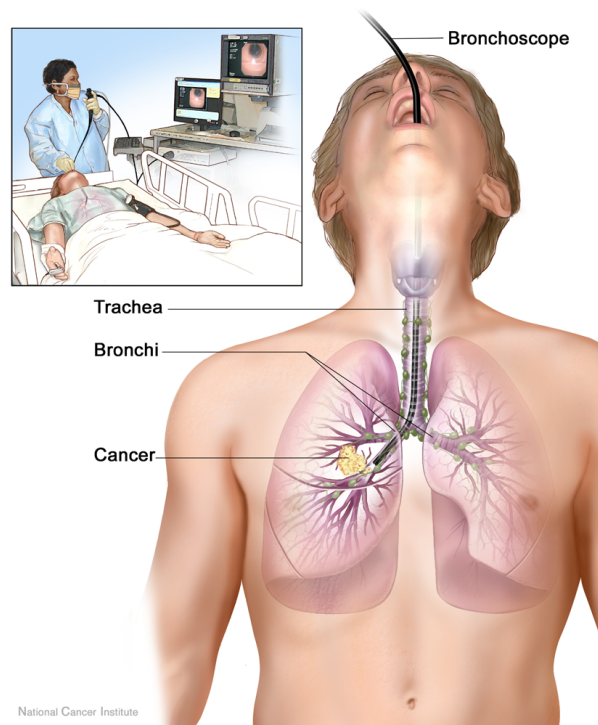


Figure 2.2: Flexible bronchoscopy in the diagnosis of a solitary pulmonary nodule. A video bronchoscope is fed into the trachea and higher order bronchi through the oral cavity. The bronchoscopist navigates to an identified lesion using a video monitor. Image acquired from the National Cancer Institute (www.cancer.gov).

2.1.3.2 Transthoracic Needle Aspiration

TTNA enables percutaneous access and core biopsy of peripheral SPNs by needle aspiration. In contrast to TBB, TTNA is primarily employed for peripherally located SPNs, thereby limiting the needle insertion depth. Overall, TTNA has a very high sensitivity of 95% and specificity of 88% for peripheral SPNs when navigated using CT-guidance [71], but degrades for lesions at < 15 mm in diameter. However, high diagnostic yield is heavily affected by the skill of the radiologist. A number of technical aspects of TTNA have been identified, which include a discussion of the benefits of immediate cytopathologic analysis following TTNA [13]. Due to the invasive nature of TTNA, the prior condition of the patient must be considered. In ~25% of cases, the patient will suffer a pneumothorax, of which a further 5-10% will require chest tube insertion [142, 17, 105, 55].

2.1.3.3 Surgical Resection

A minority of indeterminate SPNs will undergo surgical resection by video-assisted thoracoscopy (VATS), considered relatively safe procedures outside the central third of the lung [67]. While CT surveillance of small SPNs is the more standard protocol, potential malignance may merit intervention [72]. One study suggests that this discrepancy in SPN management may be owing to a bias toward resection within surgical subspecialties [110]. The resection of indeterminate SPNs is considered to be curative, demonstrating dramatically improved 5- and 10- year survival rates following early detection [53, 79]. Primary scenarios in which VATS is performed include: previous diagnosis of cancer, MDCT uncovers at least one coexisting nodule, or if the SPN > 1 cm in diameter [38]. Alternatively, surgery is often ruled out in cases where the patient presents poor lung reserve or in which lobectomy has been performed previously. For lesions > 3 cm in diameter, VATS is not appropriate, and resection by thoracotomy is undergone.

2.1.4 Bronchoscopy in the Diagnosis of Small, Peripheral SPNs

At present, management of small SPNs (< 10 mm) is lacking and there is little agreement over their prognostic implications. While detection has vastly improved with the advent of MDCT, intervention is foregone in favor of surveillance. While subsequent growth likely clarifies etiology, delayed intervention places the patient at increased risk of advanced lung cancer. FDG-PET, though highly sensitive to cancer in larger lesions, suffers a high incidence of false positives in small SPNs. Likewise, diagnostic yield from tissue biopsy is effected by lesion size. The respective sensitivities and specificities for TTNA and TBB drop significantly for SPNs with < 2 cm diameter, due to accuracy in targeting the lesion. Consequently, tissue diagnosis is often reserved for cases in which malignance is highly suspected. Reducing mortality and morbidity rates for lung cancer would benefit from a more accurate, less invasive, and less expensive means of diagnosing disease at its earliest stages, namely these very small SPNs.

Despite the diagnostic limitations, FB has a number of advantages: 1) tissue removal is minimally invasive and thus results in fewer procedural complications; 2) discolorations and other subtle abnormalities that are radiographically transparent are easily identifiable; 3) several biopsies can be taken quickly and easily from multiple locations within the lung; 4) patient sedation is not required; and 5) accompanying instrumentation is compact and relatively inexpensive. The poor diagnostic yield of TBB of peripheral SPNs is the result of inaccessibility. While the diagnostic yield for FB overall is quite good, the large diameter prevents navigation of the bronchoscope beyond the central airways where many nodules occur. In such instances TBB is performed by blindly extending the biopsy tool into the effected lung, or under the aid of fluoroscopy. In either case, the diagnostic accuracy is degraded by inability to visualize the endoluminal surface and placement of the biopsy tool. At present, TBB would benefit from smaller scopes and instruments capable of imaging these peripheral airway regions.

2.2 The Scanning Fiber Endoscope

Our laboratory has constructed an ultrathin (1.6 mm) scanning-fiber endoscope (SFE) that is revolutionary in its design [123] and imaging capabilities. The SFE possesses a much smaller outer diameter than most ultrathin endoscopes while achieving a much higher image resolution and field of view. This miniaturization is afforded by replacing the relatively large fiberoptic bundle or CCD array found in conventional endoscopes with a single scanning optical fiber. Consequently, the SFE does not image by diffuse illumination, but rather, by directed delivery of laser light through the single scanning fiber. Image resolution is therefore determined by the Gaussian limited spot size of the laser beam rather than by the size of individual imaging elements. With this laser scanning approach, high resolution images can be generated from the SFE, whereas element-per-pixel imaging devices are forced to confront the fundamental trade-off between endoscope diameter and image resolution. Advanced design features of the SFE include:

- small overall diameter (1.6 mm)
- high resolution (500×500) images
- video frame rates (30 Hz)
- small bend radius
- low-cost components

This novel SFE design offers improved diagnostic capabilities within regions of the body that are inaccessible to larger endoscopes. Preliminary *in vivo* imaging has been demonstrated within the airways [135], bile duct [10], and the lower esophageal sphincter [122].

2.2.1 SFE Distal Tip Components

The components within the distal tip of the SFE are depicted in Figure 2.3. Red ($\lambda = 635$ nm), green ($\lambda = 532$ nm), and blue ($\lambda = 443$ nm) laser light is coupled into the single optical fiber and then focused through the lens assembly onto the image plane. Images are acquired

by laser scanning of the surface in a spiral path starting from the image center and extending radially to the edges of the image. With this design, full-color 500-line resolution images can be acquired with a large field of view ($>60^\circ$).

The majority of the engineering effort has been dedicated to the development of the scan engine, which includes the scanned illumination fiber, piezo tube actuator, collar, and the scanner housing. Deflection of the scanning fiber is achieved by applying a voltage to the piezo actuator. The piezo tube is broken into four quadrants, both negative and positive quadrant pairs, which independently actuate the fiber at its single mode resonant frequency in both x and y axes. A circular scan pattern can be acquired by applying sinusoidal voltages to both the x and y electrode pairs with a 90° phase offset as shown in Figure 2.4. Modulation of the sinusoidal amplitude using a linearly ramped envelope results in an outwardly radiating spiral scan pattern. At the end of each spiral scan, a breaking sequence drives the scanning fiber back to its resting state before acquiring a new frame.

Because laser scanning illuminates only a single point of the surface at any instant, high resolution images can be obtained using only a small number of sensing elements rather than the large CCDs and fiber bundles used for wide field illumination. During scanning, reflected laser light is collected through an annular ring of twelve return fibers which surround the scanner housing. Collected light is transmitted and detected at the proximal base station where the intensity values of each scan sample are mapped to a 2D pixel location to construct the final video image.

2.2.2 The Complete SFE System

The SFE system, including the base station, workstation, transport cart, display monitors and imaging probe are pictured in Figure 2.5a. A schematic of the base station is also provided in Figure 2.5b. The SFE is operated through a workstation containing custom software to control the SFE scan parameters and compute the scanner drive signal. Housed within the base station are the red, green, and blue laser diodes which couple into the SFE probe through a front end connector. To construct each video image, reflected light is fil-

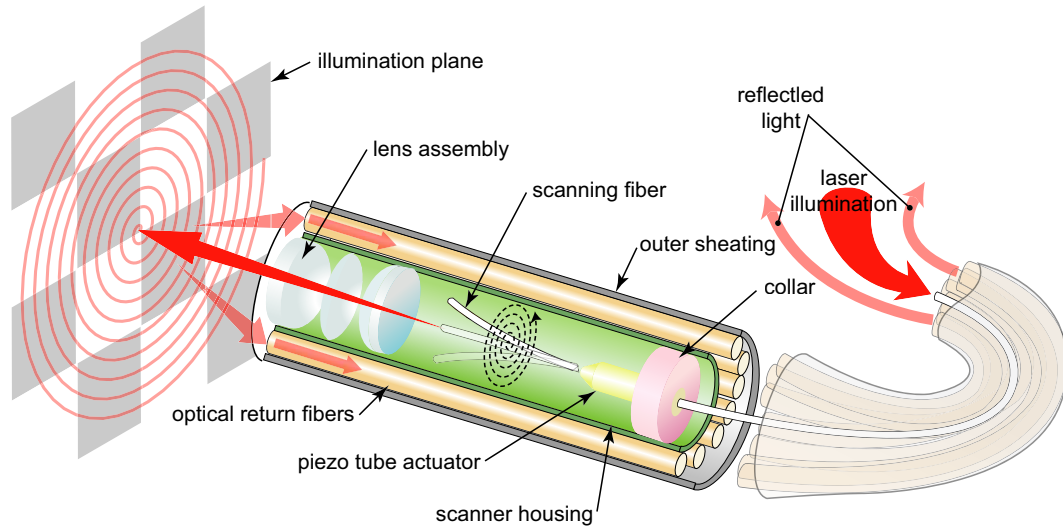


Figure 2.3: Functional schematic of the scanning fiber endoscope distal tip.

tered through a color separation system and amplified by parallel photomultiplier tubes for each color channel. The acquired signal is then processed by an image generator FPGA board within the workstation and displayed in real time on a VGA monitor. Prior to imaging, the SFE is placed in a calibration chamber to set the scan parameters. As part of the calibration, a position-sensing diode plots the true scanned path of the SFE fiber during imaging. The imaging parameters are adjusted to achieve the optimal scanning characteristics as determined by the circularity of the scan path and absence of distortion.

2.2.3 Advantages of SFE for Evaluation of SPNs

Miniaturization of endoscopic devices introduces new avenues for evaluating pulmonary diseases within small peripheral airways. Previous work has already substantiated the utility of ultrathin bronchoscopes for diagnosis of lung cancer [116, 167]. However, current ultrathin bronchoscopes suffer from poor image resolution, fragility, high cost, and are still relatively large (2.5 – 3.0 mm OD) . The SFE, by contrast, is half the size of other ultrathin endoscopes while providing superior image resolution for potentially much cheaper costs.

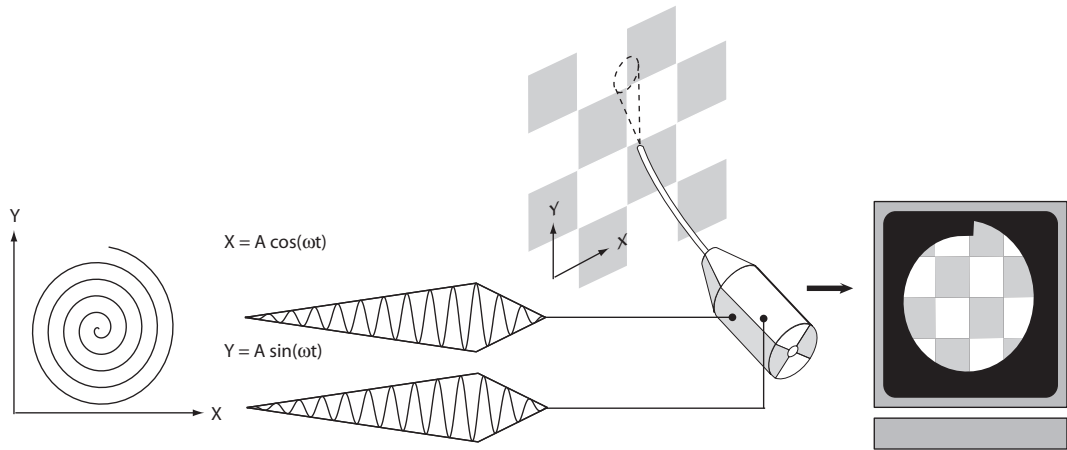
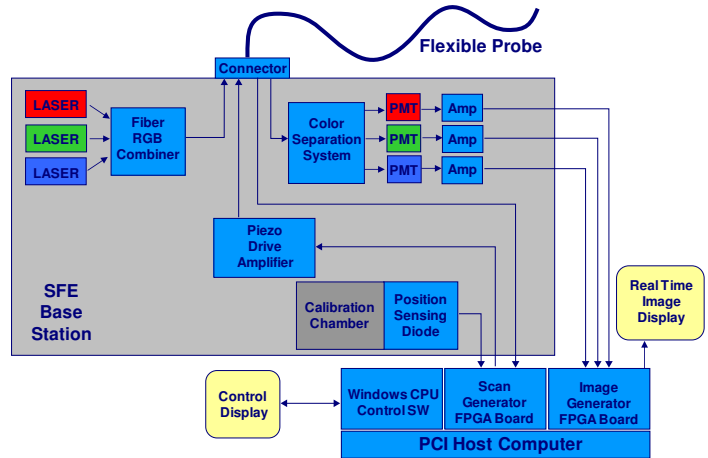


Figure 2.4: Input voltage signal used to generate the spiral scan pattern.



(a)



(b)

Figure 2.5: The complete SFE system (a) includes the base station, workstation, display monitors attached to a transport cart. A diagram of the base station (b) shows the interaction between the base station, SFE imaging probe, and workstation.

Table 2.1: Number of airways and average airway diameter for each branching generation [59].

Generation	No. Airways	Diameter (mm)
0	1	18.0
1	2	12.2
2	4	8.3
3	8	5.6
4	16	4.5
5	32	3.5
6	64	2.8
7	128	2.3
8	256	1.86
9	512	1.54
10	1,024	1.30
11	2,048	1.09
12	4,096	0.95

Though still in a prototype stage, SFE probes are physically durable, provide superior image quality, and can be easily transported between our engineering lab and the hospital. The work in this dissertation constitutes the first steps in evaluating the SFE *in vivo*.

2.3 Bronchoscopic Navigation

Due to the small size and unique imaging capabilities of the SFE, extension into peripheral airways for bronchoscopic evaluation of SPNs is feasible. This provides a means of diagnosing lung cancer at earlier stages with reduced cost and risk of complication. While conventional bronchoscopes, roughly 5 mm in diameter, can only reach fourth generation airways, the SFE is small enough to access ten branching generations. The increase in the number of airway generations reached by the SFE is commensurate with an exponential increase in the number of accessible airways, as listed in Table 2.1. While conventional bronchoscopes can reach a total of 2^4 or 16 airways, the SFE can reach 2^{10} or a total of 1,024 airways.

While the increase in accessible lung volume is motivating translation of the SFE technology to clinical application, this presents a significant challenge to the bronchoscopist who must navigate the airway anatomy to reach the identified lesion. While navigation of a conventional bronchoscope within the central airways the bronchoscopist can mentally reconstruct a path to a lesion from the CT scan directly. However, peripheral airways lie outside the bronchoscopist's working anatomical knowledge. To enable accurate biopsy of small SPNs identified on CT scans, a means of assisted navigation is imperative. To assist with TBB of peripheral SPNs a number of guidance strategies have been proposed. These include radiological imaging, subsurface interrogation, electromagnetic tracking, and virtual guidance.

2.3.1 Radiological Imaging

Intraoperative CT and fluoroscopic imaging provide a valuable means of locating the bronchoscope or biopsy tool relative to a lesion. Shinagawa *et al.* demonstrated effective biopsy of small SPNs using real time CT-guidance coupled with virtual bronchoscopic images [126]. Tsushima *et al.* experimented with real time guidance using CT fluoroscopy and found improved sensitivity in diagnosing small SPNs over the standard 2D X-ray fluoroscopy [152]. Carlson *et al.* also used CT fluoroscopy with Breath-hold monitoring for improved targeting of SPNs by TTNA [12]. Miyoshi *et al.* relied on CT-guided coil marking of small SPNs using an ultrathin bronchoscope for later resection by VATS [95]. Asano *et al.* also employed CT fluoroscopy to guide forceps for biopsy of peripheral lesions using an ultrathin bronchoscope [1]. Using this technique, the ultrathin bronchoscope was successfully advanced to 94.7% of all nodules.

Though studies using CT fluoroscopy have indeed shown improved diagnostic accuracy for peripheral SPNs, there are a number of limitations. Navigation through a 3D anatomy using 2D fluoroscopic X-ray images is perceptually awkward, and high-density regions, such as bone, can occlude the lesion and the biopsy tool. For imaging of smaller SPNs, fluoroscopy has often proved to be unreliable. By contrast, CT fluoroscopy provides real

time multislice CT imaging at an operator-controlled position. However, this requires use of expensive imaging equipment and dedicated CT rooms, incurring added expense. During the procedure, the patient and physician are exposed to X-ray radiation that is potentially health compromising and places limits on the amount of time allowed for the procedure.

2.3.2 Subsurface Interrogation

Unlike radiological imaging that provides a large-scale external visualization of the scope, tool, and target lesion, accessory imaging modalities can be equipped to the bronchoscope itself to interrogate local subsurface anatomy. More recently, miniature endobronchial ultrasound (EBUS) transducers are fed through the bronchoscope working channel to intra-operatively image a subsurface lesion and biopsy needle several centimeters deep. Herth *et al.* found performance of EBUS-guided biopsy of peripheral SPNs with forceps to be on par with fluoroscopic imaging [54]. Kanoh *et al.* also showed that real time visualization of needle aspiration using EBUS significantly improved accurate diagnosis of lymphadenopathy in patients [70]. A limitation of EBUS is that penetration of ultrasound waves into tissue requires close coupling of the EBUS transducer to the endoluminal wall and is only propagated along one side of the airway lumen. By contrast, optical coherence tomography (OCT) can be used to image radially in all directions [80] and is not limited by the air-tissue impedance mismatch. However, OCT imaging depth is only 1-2 mm. While this is advantageous for optical staging of dysplastic regions at the lumen surface, it is not ideal for biopsy of SPNs that are likely more than several millimeters in size. Ultimately, subsurface interrogation by introduction of these accessory imaging modalities is technically limited. While evaluation of peripheral lesions promotes use of smaller bronchoscopes, use of EBUS and OCT introduces additional hardware and limits extension into small airways. Imaging is also limited to subsurface anatomy and depends first on accurate navigation of the bronchoscope to a site near the lesion. In another study by Eberhardt *et al.* EBUS could not be performed in 33 of 100 patients due to inability to locate lesions [27].

2.3.3 Electromagnetic Tracking

Electromagnetic tracking or EMT systems have miniature sensors (~ 1 mm OD), which measure the electromagnetic field induced by a transmitter to determine the sensor's relative position and orientation with 5 or 6 degrees of freedom (DoF) ($x, y, z, yaw, pitch,$ and $roll$ -optional). By attaching this sensor to the tip of a bronchoscope or biopsy tool, it is possible to maneuver the device to the known location of a nodule. A preoperative CT scan serves as a roadmap of the anatomy, and once the EMT system is properly registered to the image, it operates similarly to GPS, tracking the scope or biopsy tool on the CT image coordinates in real-time. The bronchoscopist is then guided by a user interface which displays the scope position and an identified target on the preoperative CT image or virtual surface model of the airways.

Early work using EMT sensors for bronchoscopic guidance began in 1998 when Solomon *et al.* used a miniature EMT sensor to locate a bronchoscope for TBNA of artificial lesions placed within the trachea of a live pig [130]. A number of navigation systems using EMT present results from tracking within an artificial model [23, 20, 97] and excised lungs [156, 2]. Hautman *et al.* observed that EMT was effective for targeting small SPNs that are unrecognized on fluoroscopic images [49]. The commercially available Bronchus navigation system (superDimension, Herzliya, Israel) has further demonstrated improved biopsy precision in guided TBB of peripheral nodules using a miniature EMT sensor attached to a steerable guidewire [120, 6, 26].

Although EMT permits accurate and robust tracking of a bronchoscope in an operative environment, a number of limitations must be considered. First, navigation is dependent on an accurate initial registration between the real anatomy in the EMT system coordinates, and the virtual anatomy in CT coordinates. Such registrations are typically computed by point-to-point alignment of fiducial markers placed on the patient's thorax or anatomical landmarks identified during the procedure. However, such registrations naturally result in point registration errors on the order of several millimeters. This is due to a two main

factors. First, registration error naturally occurs from the fact that localized fiducials or landmarks on the patient will not be perfectly congruent with those identified in a CT image. Second, the patient anatomy is deformable, and motion due to shifting of the body, respiration, and coughing can result in misalignment with the static CT image. The result is considerable registration error and strained navigation, which degrades biopsy accuracy at best, or is unusable at worst. Though use of EMT systems has demonstrated improved diagnostic sensitivity for small SPNs, overall diagnostic yield remains low and would benefit greatly from any form of visual feedback to assess accuracy of the registration at the site of the lesion.

2.3.4 Virtual Guidance

Unlike the previous guidance approaches, virtual guidance does not require additional external hardware, but rather uses a computer generated virtual surface model of the airways as a roadmap with visualization of subsurface lesions. For TBNA of hilar and mediastinal lymph nodes virtual bronchoscopy was performed to produce simulated views of the optimal needle insertion point for reference during flexible bronchoscopy [89, 158]. A similar system by Geiger *et al.* has validated virtual guidance for needle biopsy of artificial targets in an airway phantom [35]. Virtual guidance may also be supplied in discrete intervals, such as a system that allows the bronchoscopist to advance or regress the virtual view at each bifurcation and rotate the view to match the real bronchoscopic video [1, 144]. A drawback of these studies is that they lack live automated guidance, requiring interaction during the procedure that is distracting to the bronchoscopist. Furthermore, passive virtual guidance requires some level of mental registration for eventual biopsy, carrying with it, some level of operator error.

Alternative methods of virtual guidance have been approached by automated image-based tracking (IBT) of bronchoscopes. IBT is achieved by 2D/3D image registration, where each 2D bronchoscopic video frame is registered to the 3D CT scan. At each frame, 2D/3D registration, or CT-video registration, involves iteratively optimizing the 6D position

and pose of the virtual camera, in CT coordinates, to maximize similarity between the video frame and the subsequent virtual rendering. Using the video images directly, accurate local registration between real and virtual anatomies is possible [9, 98, 22, 51]. Unlike EMT-based localization, which relies on a globally precomputed rigid registration between EMT and CT coordinate systems, CT-video registration is applied to each frame, resulting in highly accurate bronchoscope localization that is not highly susceptible to deformation. Despite this, two major limitations persist. First, image-based tracking requires continuous and unobstructed video input, and can therefore only be used in regions that are accessible to the bronchoscope. Second, due to the large parameter space searched during image-based registration, it is necessary to provide an accurate initial estimate of the position and pose at each frame. As a result, IBT assumes that the motion between subsequent video frames is sufficiently small to be captured by the registration. Once IBT diverges from the true bronchoscopic path, it cannot recover without user intervention. As a result, abrupt motion, coughing, or obscuring of the scope by mucus or blood can cause tracking failure.

2.4 A Navigation System for SFE in Peripheral Airways

Although the bronchoscopic guidance methods previously described have met with some degree of success, a number of limitations prevent clinical standardization of these techniques for TBB of small SPNs. Radiological imaging is expensive, potentially deleterious, and does not provide directional guidance *en route* to the lesion. EMT can be used in conjunction with a preoperative CT to localize the bronchoscope within the airways in relation to a path to a lesion. However, registration error presents a significant degree of uncertainty in biopsying small lesions. IBT can provide accurate tracking, but requires continuous video and can suffer from aberrant tracking.

A majority of the literature has focused on tracking in the central lung, where airways are much larger and within the bronchoscopist's mental framework of the anatomy. Within peripheral airways, tracking becomes more challenging in that small errors in localization

more greatly impact effectiveness of guidance (for instance, mapping the SFE position to a point in an incorrect airway or outside the airways altogether). This is further complicated by large respiratory-induced displacements that occur in the peripheral airways, resulting in greater misalignment between the deformable airways and the virtual model.

As part of our effort to improve clinical management of small, indeterminate SPNs, a navigation system was conceived with the following essential features:

- 1. Stand-alone system without dependence on external imaging systems.**
- 2. Robust and accurate tracking of the SFE in both large and small airways.**
- 3. User interface software to effectively direct the bronchoscopist and guide biopsy of a 1 cm nodule.**

In this dissertation, we discuss the development of a navigation system and experimental results. In earlier chapters, computational methods for generating a virtual airway model are described and we elaborate on the preoperative planning software that is used to define a 3D path to guide the bronchoscopist to a peripheral lesion. As part of the development we evaluated the accuracy of both EMT and IBT strategies independently during navigation within a benchtop and live animal model. In parallel, we evaluated the potential impact of respiratory motion on tracking accuracy by quantifying deformation through nonrigid registration of CT images taken at various phases of respiration. We ultimately propose a hybrid tracking system that incorporates both EMT and IBT in a novel tracking algorithm. In the final embodiment, respiratory motion compensation is integrated into the tracking framework, providing optimal tracking stability in peripheral lung regions.

Chapter 3

CONSTRUCTION OF A VIRTUAL AIRWAY MODEL

Preoperative MDCT is now predominantly used for both detection and observation of small SPNs. This image also provides roadmap of the patient anatomy that is helpful for locating a lesion relative to other anatomical landmarks and can be used to generate interactive virtual bronchoscopic views for preoperative planning or virtual guidance during an examination. In this chapter, we discuss the construction of a virtual airway model by analysis of the preoperative CT image. The virtual model includes a surface mesh of the airways and a centerline tree model that defines the central axis of each airway and its relation to both parent and child airways.

The preprocessing pipeline is illustrated in Figure 3.1. The initial preprocessing stage performs automated segmentation of the airways, from which a binary mask is computed that corresponds to airway regions. From this extraction, the virtual surface model is generated and the centerline analysis stage produces airway centerline paths and branchpoints throughout the segmented tree. This chapter describes in detail the three processes of airway segmentation, virtual surface model generation, and centerline analysis as well as providing a survey of current techniques in this field.

3.1 Airway Segmentation

3.1.1 Background

Image segmentation is the process of labeling regions that correspond to particular objects within the image. On CT images, each voxel possesses a graylevel that is equivalent to

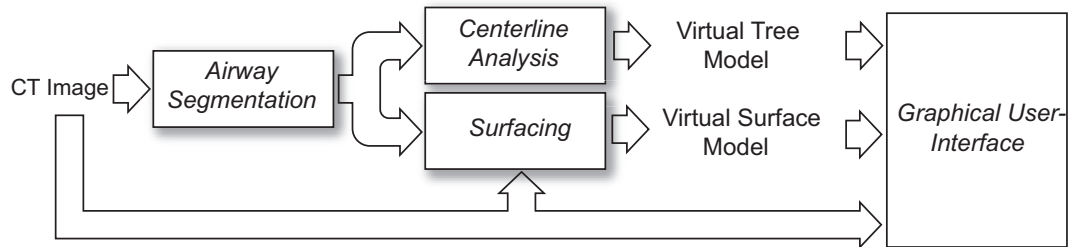


Figure 3.1: The processing pipeline for preoperative MDCT.

the density averaged over the voxel volume and expressed in Hounsfield units (HU). The airways appear as a series of low-density bifurcating vessels that progressively decrease in diameter with path-length from the trachea. In general, the airways are characterized by dark, low-density regions (-1000 HU) circumscribed by bright airway wall voxels (0 HU). In the larger conducting airways, the dark air regions and bright wall regions are easily identified. Several generations down, in the transitional airways, the branch diameter eventually decreases beyond the resolution of the CT image. At some point, segmentation is halted by partial volume effects, where the individual voxels that comprise the airways overlap both the airway and the lumen wall, producing a segmentation that is incomplete at some level. In large part, the performance of airway segmentation algorithms must be evaluated within the context of the application. For example, one application may require accurate measurement of small airway diameters for computing air flow, while another may be primarily concerned with the topological realism of the resulting virtual surface model. Yet another may wish to perform some sort of automatic detection of airway stenosis in the central airways. Overall, as multi-slice CT resolution has improved, segmentation schemes have become more accurate and more sophisticated.

In general, approaches to airway segmentation can be categorized as one or a combination of the following strategies: region growing, rule-based segmentation, and mathematical morphology. A number of segmentation algorithms using probabilistic models such as neural networks [83], fuzzy logic [114, 108, 151], or trained classifiers [82] have also been

used to an extent though they do not comprise the major thrust of development in this area of late. An overview of these methods is described below with particular focus on groups whose work constitutes the majority of research on this subject since its inception.

3.1.1.1 Region Growing

Region growing is commonly used as an initial segmentation stage for the reason that it takes little time to execute and provides a good first approximation of the object. To start, a seedpoint is selected from within the region, forming a single one-voxel component. Neighboring pixels (2D) or voxels (3D) are then checked and added to the region if their intensity is above or below a given threshold. This proceeds at each border voxel until no more neighbors can be added to the component.

In segmenting the airway tree, 3D region growing proceeds by selecting a seedpoint in the trachea and growing a region of low-density air voxels, below a given threshold, to form an individual component that represents the airways. As this threshold is increased, a larger percentage of airway voxels are included in the segmentation. At some point, the threshold is sufficiently high that the growing region breaks through the airway wall and “leaks” into the surrounding parenchyma, causing the segmentation to flood the entire lung. Summers *et al.* [139] empirically chose a threshold of -675 HU for optimal distinction of airway and non-airway regions. Mori *et al.* [100] employed an adaptive “3D painting” algorithm to find an optimal threshold in each CT image. In this technique, 3D region growing is performed at an initially low threshold estimate and expanded by incrementing the threshold until the volume of the airway component “explodes”, indicating a segmentation leakage from the airways to the lung parenchyma. The threshold value is then decremented by one to the value just preceding the explosion. This adaptive strategy has been very successful and is now widely used as a the first stage in airway segmentation.

Adjustments to this technique have tried to work around using a globally optimal threshold for region growing by operating on subvolumes of the image. In the approach by Tschirren *et al.* [151], a locally optimal threshold is found within overlapping regions

of interest using a fuzzy logic strategy to discern airway voxels from non-airway voxels. Szymczak and Vanderhyde [143], applied a topology-driven region growing method that selects a locally optimal threshold in a “thick slice” subvolume based on limiting the number of connected components in each slice.

3.1.1.2 Rule-Based Segmentation

Rule-based segmentation is applied as a filter that accepts or rejects candidate regions based on a set of criteria leveraged by knowledge of the anatomical structure and morphology. Sonka *et al.* [132], used the close structural relationship of bronchial airways to pulmonary blood vessels to limit candidate airway regions. This approach improved airway detection, as the bright high-density vessels that run adjacent to airways are much more easily identified on each 2D slice. The research group of Mayer *et al.* [88] and Bartz *et al.* [5] implemented a wave propagation algorithm to extend airways in 2D slices using a series of shape-based rules. With this method, candidate airway regions were advanced or terminated on the basis of diameter, change in diameter, and number of branches. A more generalized tree-extraction method was further proposed in three-dimensions by Bulow *et al.* [7]. Zheng and Leader [176] used both the area and circularity of the airway region on 2D slices as metrics to accurately identify candidate airway regions.

3.1.1.3 Mathematical Morphology

Mathematical morphology is generally typified by the use of operators to enhance image regions by size, shape, and intensity level, and provide unique advantages over region growing and rule-based segmentation. Unlike region growing, which operates on the grayscale intensity values, morphological filtering of an image produces grayscale values that reflect local shape characteristics such as the relative height of local peaks and valleys. This has been especially advantageous for segmentation of small airways where partial-volume effects preclude classification of airway and non-airway regions by grayscale value alone. Further, with the advent of MDCT imaging systems (several hundred slices), mathematical

morphology provides a more robust approach to processing volumetric topologies rather than developing a set of empirical rules to connect features in contiguous 2D slices that are potentially spaced several millimeters apart.

In the work by Kiraly *et al.* [75], grayscale reconstruction was used to identify candidate airway regions in a CT image. On each 2D slice, airway cross-sections appear as dark circular holes, or valleys, circumscribed by a steep white ridge comprising the airway wall. By applying a series of morphological operators of increasing radii in the reconstruction, candidate airway regions of the same approximate shape are labeled. In the method developed by Fetita *et al.* [29], a morphological operator is used to identify airway regions based on their connection cost as defined by the smallest grayscale peak which separates potentially connected regions.

3.1.2 Methods

Before elaborating on the methods employed in our system, it is worth prefacing the specific challenges of airway segmentation as it relates to navigation of the SFE in the peripheral airways. From a clinical viability standpoint, the ideal navigation system would produce a near-perfect virtual model of the airway anatomy, require little or no human interaction, and run within a time frame of a few minutes. As a practicality, however, software components, such as segmentation, can be programatically complex, potentially require many minutes to hours to execute, and require multiple data sets for testing. Because the development of more accurate airway segmentation methods is largely orthogonal to the goals set forth by this dissertation, currently published approaches were evaluated on the basis of sensitivity to smaller airways (specifically those large enough to accommodate the SFE), robustness, and overall complexity.

Given the small size of the SFE, the ideal segmentation would extract all airway regions of equivalent or larger diameter. At present, the 1.6 mm outer diameter of the scope translates to an equivalent cross-sectional area of approximately 9 pixels given an isotropic pixel spacing of 0.5 mm. The algorithm performance must also be appropriately robust so as to

provide decent segmentation results given a range of different patient body types, scanner types, and image reconstruction kernels. Lastly, algorithm complexity is a significant factor in development time. Use of highly sophisticated algorithms, excessive parameterization or tuning, or requisite training sets all limit feasibility. Ultimately, a modified version of the method proposed by Kiraly *et al.* [75] was used for segmentation of airways in our CT image sets, and is described in further detail below. In this strategy, the segmentation is broken into two separate stages including adaptive region growing and morphological analysis.

3.1.2.1 CT Imaging

Automated airway segmentation was tested on both porcine and human CT images. CT imaging of live pigs was performed at the University of Washington Medical Center using a VCT Light-Speed scanner (General Electric, Milwaukee, WI), using a protocol approved by the University of Washington Animal Care Committee. Helical CT scanning produced a volumetric image lattice, I , for which each voxel position, (x, y, z) , is given a grayscale value in HU. The image slice resolution was 512×512 with several hundred slices and an isotropic voxel spacing, $(\Delta x, \Delta y, \Delta z)$, of 0.5 mm. During each scan, the subject was placed on a continuous positive airway pressure of 22 cmH₂O to prevent respiratory artifacts. This static respiratory airway pressure roughly corresponded to full inspiration. Imaging at full inspiration was preferred due to the fact that increased air volume expands the airways, making them easier to differentiate for segmentation. Images were recorded to DVDs and transferred to a Dell 470 Precision Workstation (3.40 GHz CPU, 2GBytes RAM) for analysis. Two anonymous human data sets were also supplied by Dr. Jed Gorden at Swedish Medical, Center, Seattle, WA. Both data sets had a slightly larger voxel spacing of 0.78 and 0.88 mm.

3.1.2.2 Image Clipping

The high-resolution images acquired from CT scanning require significant memory usage during segmentation. From the image spacing specified, and a 16-bit grayscale value, each image requires 200 MB of memory. This image size can be significant both with regard to the amount of memory usage and the amount of processing time. Because the actual lung volume is typically a fraction of the image volume, clipping the original CT image allows for more efficient memory management and faster processing. To clip the image, an initial segmentation of the lung region is performed using the method of Hu *et al.* [62]. The original image is then cropped such that the boundary completely contains the lung region.

3.1.2.3 Adaptive Region Growing

Region growing is almost universally used as a first stage to airway segmentation. To start, a seed point is selected, either manually or automatically to initialize the segmentation. In this case, an automated selection algorithm was used. To find the seed point, the trachea is first localized within the top slice of the CT image, $I_0 = I(x, y, 0)$. Candidate trachea regions are selected by overall area, solidity, and extent. When more than one candidate region occurs, the most central candidate region is selected. The closest center pixel of the region is then selected as the seed point for region growing, expressed as the 3D voxel coordinate: (x_s, y_s, z_s) .

The result from region growing I_R is stored as a binary mask in which airway regions are assigned a value of 1 and non-airway regions are assigned a value of 0. Prior to region growing, the input image I is median filtered to reduce image noise. Median filtering is advantageous in that it removes noise which can attribute to inaccurate segmentation while avoiding smoothing effects. The segmentation I_R is then initialized such that $I_R(x, y, z) = 0, \forall (x, y, z) \in I_R$, with the exception of the seed point, where $I_R(x_s, y_s, z_s) = 1$. During the first iteration of region growing, each voxel $(x, y, z) \in N_{27}(x_s, y_s, z_s)$ is processed such that for a threshold T , $I_R(x, y, z)$ is set to 1, for all $I_R(x, y, z) \neq 1$ and $I(x, y, z) < T$. The function

$N_{27}(x,y,z)$ is used to denote the $3 \times 3 \times 3$ neighborhood of the center voxel (x,y,z) . Each voxel added to I_R is similarly processed until no further voxels can be added. In the adaptive implementation, 3D region growing is progressively re-run at increasing threshold values until an explosion in the volume of segmented voxels is detected, indicating a bleed-out into a discontinuous region (in this case the lung parenchyma) [100].

Figure 3.2 illustrates the 3D region growing algorithm. A key difference in this implementation is that the threshold value is incremented at various resolution levels. This allows much faster convergence of the adaptive region growing strategy. For each value of T , region growing is performed. If $\Delta V > \Delta V_{max}$ and $V_{new} > V_{min}$, an explosion is registered, and T is decremented by ΔT . For future iterations, ΔT is cut in half for finer step changes, unless $\Delta T = 1$, in which case region growing is halted and a final 3D region growing is performed. From empirical testing, the values of V_{min} and ΔV_{max} were set to 30,000 and 100,000 voxels respectively. A result of the adaptive 3D region growing is given in Figure 3.3.

3.1.2.4 Morphological Analysis

The second stage of the segmentation scheme relies on analysis of 2D airway morphology. Within each slice, grayscale reconstruction enhances regions of the image characterized by dark, circular regions that are equivalent in size to a morphological operator of our choosing. From this, a set of candidate airway regions are identified for potential inclusion in the final segmentation.

During grayscale reconstruction, a *marker* image is successively dilated or eroded until its topology is completely contained within a second *mask* image. For reconstruction of airway regions, iterative erosion of a marker image J_1 , over the mask S , produces a final reconstruction J_∞ by the equation:

$$J_{k+1} = \max(J_k \ominus B_4, S) \quad (3.1)$$

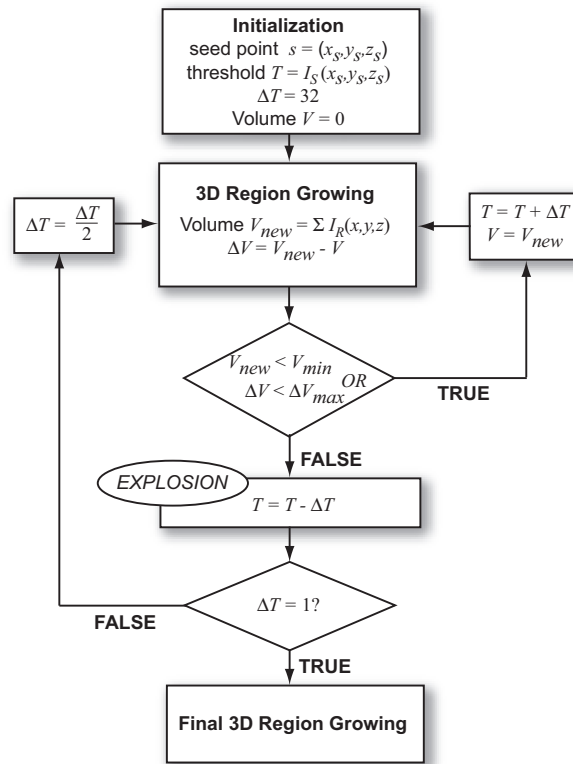


Figure 3.2: Block diagram of the adaptive 3D region growing segmentation stage.

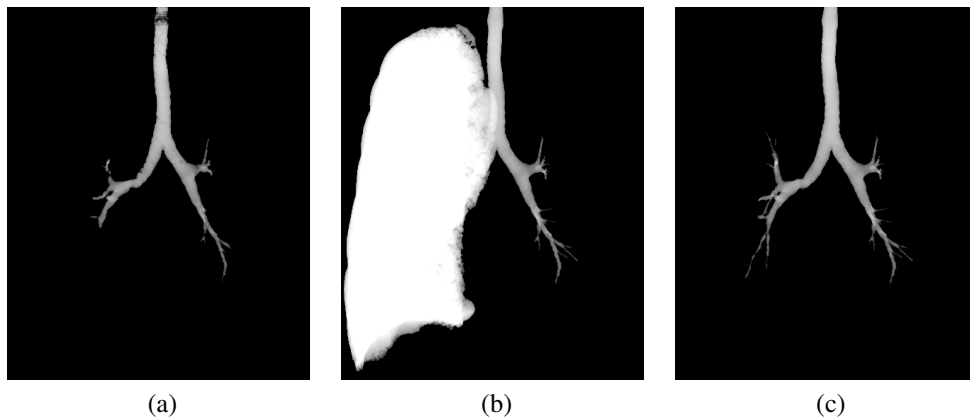


Figure 3.3: Results of 3D region growing. The initial region growing segmentation (a) starts from the seed point to acquire a minimum volume. The threshold, T , is increased until the segmentation explodes out into the parenchyma (b). The optimal segmentation is acquired by decrementing T to its value just before the explosion.

where B_4 is the 2D 4-connected neighborhood (Figure 3.5). This is repeated until there is no change in the reconstructed image from iteration k to $k + 1$, stated formally as:

$$J_\infty(x, y) = J_{k+1}(x, y) = J_k(x, y) \quad \forall (x, y) \in J_\infty$$

A 1D example is shown in Figure 3.4. A cross-section of an airway is depicted through a transverse CT slice in which the trough corresponds to the dark airway surrounded by a bright ridge representing the airway wall. For reconstruction, the image data itself is set as the mask, S , and the marker J_1 , is computed by dilation of S , as shown by two different dilation kernel sizes in Figure 3.4(b) and Figure 3.4(c). Reconstruction of J_1 by equation 3.1 produces a topology in which valleys having a radius smaller than the dilation kernel B are filled in. The airway regions are then enhanced by the difference image given by $J_\infty - S$. In the first example, the dilation by B does not fill in the airway trough, resulting in non-detection. With the larger kernel in the second example, reconstruction produces strong evidence of an airway region.

Grayscale reconstruction is applied to each 2D slice of the CT image, such that $S(x, y) = I_z(x, y)$, windowed between -1000 and 0 HU for all slices of z in the image. This is done to nullify contributions from bone or other high-density features on the reconstructed image. The marker image J_1 , is computed by grayscale closing of S with an arbitrary operator B :

$$J_1 = S \bullet B = (S \oplus B) \ominus B$$

Following reconstruction of J_1 to J_∞ by equation 3.1, a binary image of candidate airway regions are identified by thresholding the difference image, $J_\infty - S$:

$$C(x, y) = \begin{cases} 1 & \text{if } J_\infty(x, y) - S \geq T_{morph} \\ 0 & \text{otherwise} \end{cases}$$

With this method, Kiraly *et al.* [75] implemented morphological analysis of airway regions

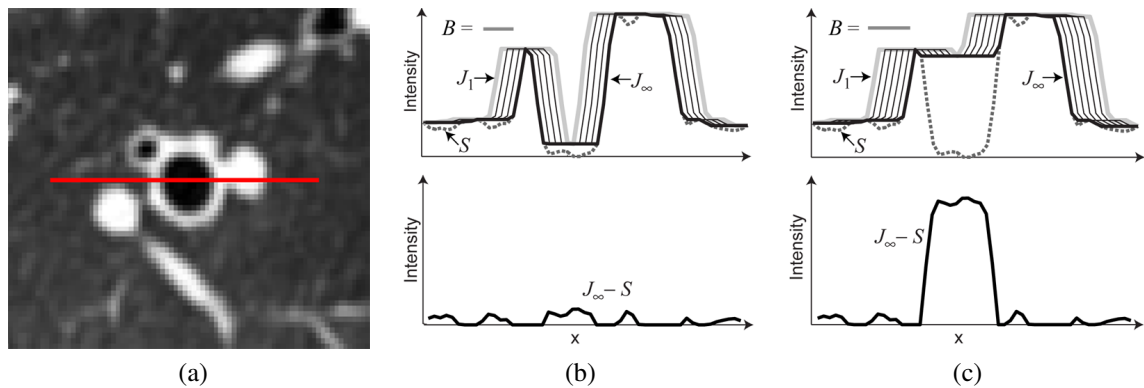


Figure 3.4: A 1D example of grayscale reconstruction of an airway. An airway is depicted on a transverse CT slice (a) with an identified 1D cross-section. The topology of the 1D cross section is represented by a dashed line (b) and (c) and is selected as the mask, S . The marker J_1 (gray), is computed from dilation of S with a smaller (b) and larger (c) dilation kernel, B . The reconstructed result, J_∞ (black), has removed valleys which are smaller than the reconstruction kernel. With the larger kernel (c), the difference between the reconstructed and original topologies, $J_\infty - S$, indicates the presence of an airway smaller than B .

in each 2D slice of the original image. Candidate regions are accumulated into a separate segmentation I_M computed from morphological processing. The segmentation results I_R and I_M are then combined and reconstructed to acquire a single segmented component I_S .

In order to reconstruct airways of different sizes during morphological analysis, a bank of operators of increasing radii were used up to the size of the largest airway as previously proposed [75]. Unfortunately, computation times prove to be quite slow with this method given the number of slices and number of kernels employed in the reconstruction. In the scheme adopted here, a modification is proposed to permit more rapid segmentation. This is achieved through two steps: a simple refinement of previously segmented central and larger airways I_R followed by more extensive processing to detect smaller airways in the peripheral lung.

The larger more central airways are predominantly evident in the region growing segmentation result I_R . However, this segmentation is heavily dictated by the computed global threshold value T rather than by more precise differentiation of local tissue-air interfaces.

A more accurate delineation of the larger airway geometry need not consider regions of the image outside of the initial segmentation I_R . Instead, each 2D cross-section of I_R can be reprocessed to better capture the surrounding airway morphology. Within each 2D image slice that intersects I_R , grayscale reconstruction is performed on each individual airway region using a reconstruction kernel just slightly larger in size than that of the airway. The refined 2D airway segmentation is then inserted into the final segmentation result I_S .

Following, small candidate airway regions are detected within the peripheral lung. Grayscale reconstruction is performed twice using a smaller reconstruction kernel B_4^1 (radius = 1), and a larger reconstruction kernel B_4^3 (radius = 3). Here, B_4^b is the kernel acquired by $b - 1$ successive dilations of B_4 , where

$$B_4^b = \underbrace{B_4 \oplus B_4 \oplus \dots \oplus B_4}_{b-1 \text{ dilations}}$$

Figure 3.5 shows the first three reconstruction kernels. From this, candidate airway regions, C^1 and C^3 are computed for each slice. The segmentation result from morphological analysis of small airways is then given as the union of candidate regions C^1 and C^3 in slice z :

$$I_M(x, y, z) = C_z^1(x, y) \cup C_z^3(x, y) \quad (3.2)$$

Figure 3.6 depicts results of morphological analysis in a window of a transverse image slice. Because the resolution of the images is isotropic or near isotropic, morphological analysis of small airways was further performed in coronal and sagittal image planes as well, though the original study by Kiraly *et al.* [75] only attempted to implement the algorithm in the transverse image slices. Therefore, equation 3.2 is rewritten to also include the results from each image dimension:

$$I_M(x, y, z) = C_z^1(x, y) \cup C_z^3(x, y) \cup C_y^1(x, z) \cup C_y^3(x, z) \cup C_x^1(y, z) \cup C_x^3(y, z)$$

The final segmentation result I_S is acquired by combining I_R and I_M . Incorporation or

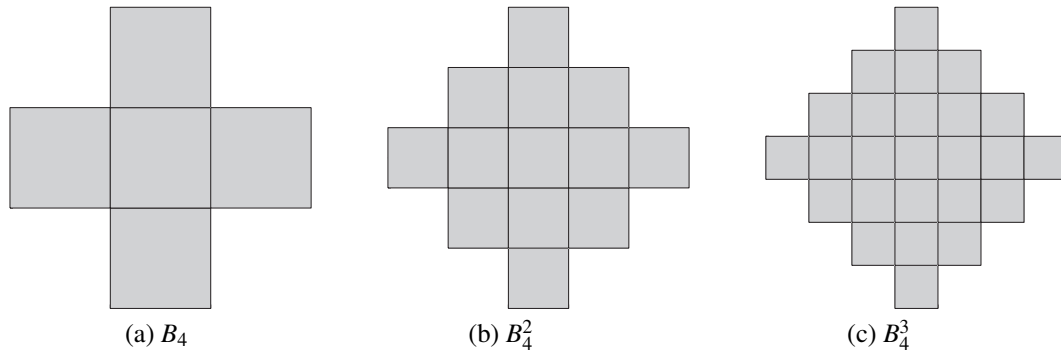


Figure 3.5: Bank of morphological reconstruction kernels of various radii.

removal of candidate regions in I_M is established by reconstructing the airway tree from the seed point. Only regions that are part of the single segmentation component are preserved.

3.1.3 Results

Segmentation results varied from each data set analyzed. Figure 3.7 shows the segmentations from four CT scans, two from pigs, and two from human patient data. The output of region growing is shown in blue. The green voxels depict airways extracted from morphological reconstruction in transverse image slices as previously proposed [75]. In red are airway regions uniquely extracted from morphological analysis in all three image planes. From the output it can be seen that additional morphological analysis on both coronal and sagittal slices improves detection of small airways that run more horizontally. For both of the pig studies, segmentation had the tendency to leak into small airspaces outside the airways, near the diaphragm.

3.2 Virtual Surface Generation

The virtual surface model provides a 3D topological map of the airways that closely mimics that of the endoluminal surfaces seen during bronchoscopy and serves as a virtual scene through which the bronchoscopist is navigated. Surface extraction is commonly performed

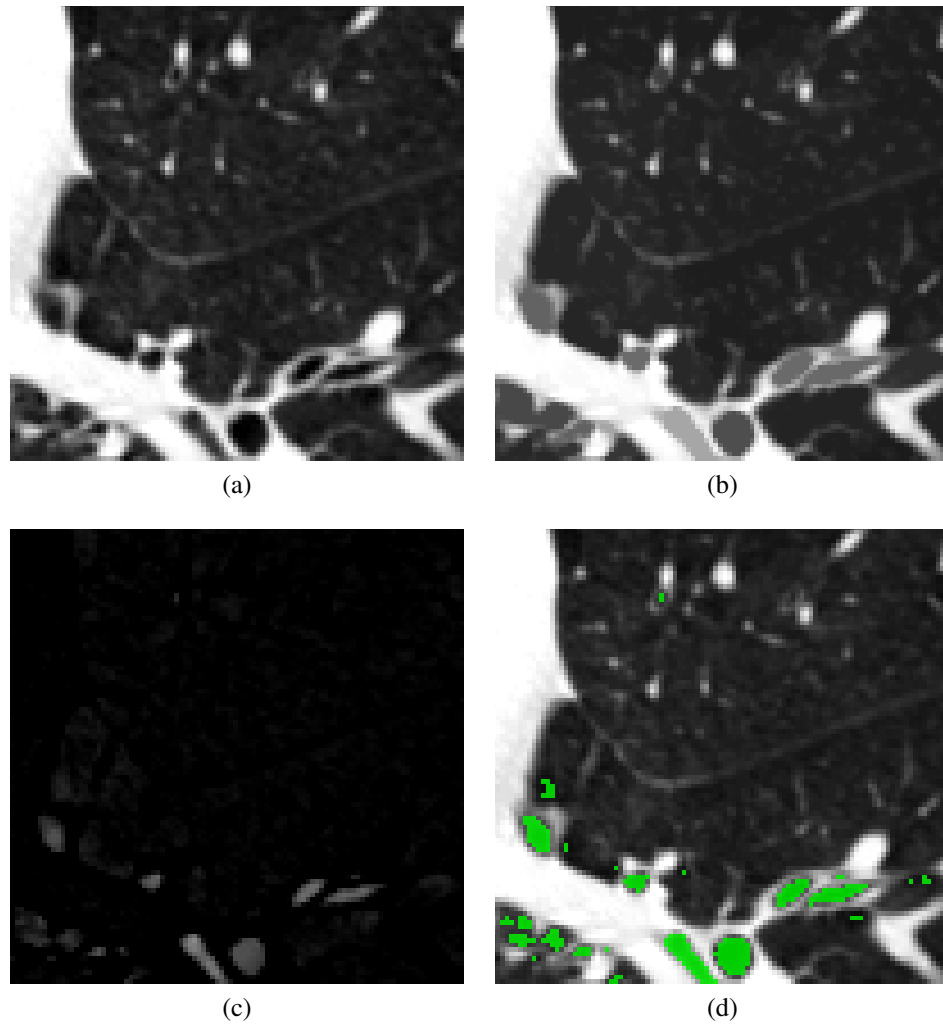


Figure 3.6: Morphological analysis of airway regions in a CT slice (a) are enhanced by grayscale reconstruction (b). The difference between the original and reconstructed images (c) is threshold to find candidate airway regions shown as a green overlay in (d).

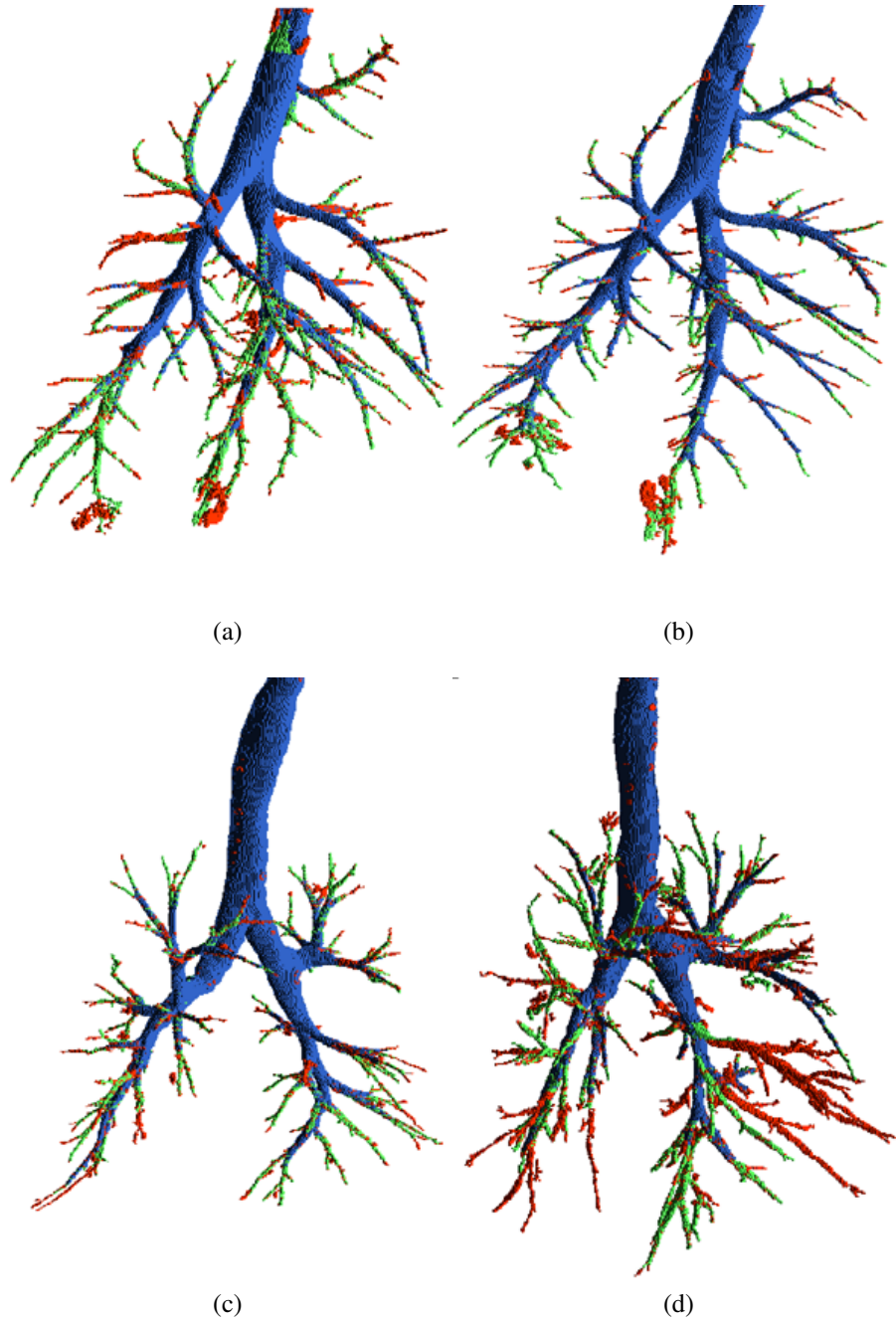


Figure 3.7: Final segmentation results for four different chest CT scans. The results from region growing are shown in *blue*, plus morphological analysis in transverse slices only in *green*, and in all three dimensions shown in *red*. Examples (a) & (b) are from two pig studies while (c) & (d) are segmented from patient scans.

by hexahedral decomposition of a rectangular image lattice at a given isovalue. The resulting manifold represents a constant value interface throughout the image. The most commonly used approach for extracting a surface mesh from lattice volumes is the *Marching Cubes* algorithm of Lorensen and Cline [84]. With regard to medical image analysis, variations of this technique are more thoroughly described elsewhere [46].

To generate a surface mesh of the airways, a contouring filter was used within the Visualization Toolkit (VTK, Kitware). As a first step in the surface extraction, a windowing function was performed on the input image I to fully encapsulate the segmented airways in I_S within the final surface as well as to prevent isosurfacing of regions outside the airways. For a given isovalue s and the voxel position x , the input image I was processed such that $I(x) = \min(I(x), s) \forall x \in I_S$ and $I(x) = \max(I(x), s + 1) \forall x \notin I_S$. For the CT images in this dissertation, an isovalue of -500 HU was used. Following the extraction of the isosurface, laplacian smoothing of the triangulated mesh was performed as proposed by Taubin *et al.* [145]. This helped to remove the blocky surface artifacts that result from surface decomposition of discrete voxels. The degree of smoothing must consider the trade-offs between under- or over-smoothing. If too few iterations of smoothing are performed, the surface maintains a rough or voxelated appearance. If the surface is over-smoothed, relevant airway features are lost, or more critically, small airways are narrowed or pinched off from the main mesh. Figure 3.8 shows four bronchoscopic images of the airways in a pig and the corresponding virtual viewpoints using various degrees of smoothing. Without any smoothing, the resulting surface is heavily voxelated. Less voxelation artifact is manifest after 100 iterations. After 200 iterations, a much smoother representation of the surface is computed, though at 400 iterations, the topology appears over-smoothed.

3.3 Centerline Analysis

The intent of the triangulated surface mesh discussed in the previous section is to reproduce topological features of the airways for visual realism. While the anatomical synchrony

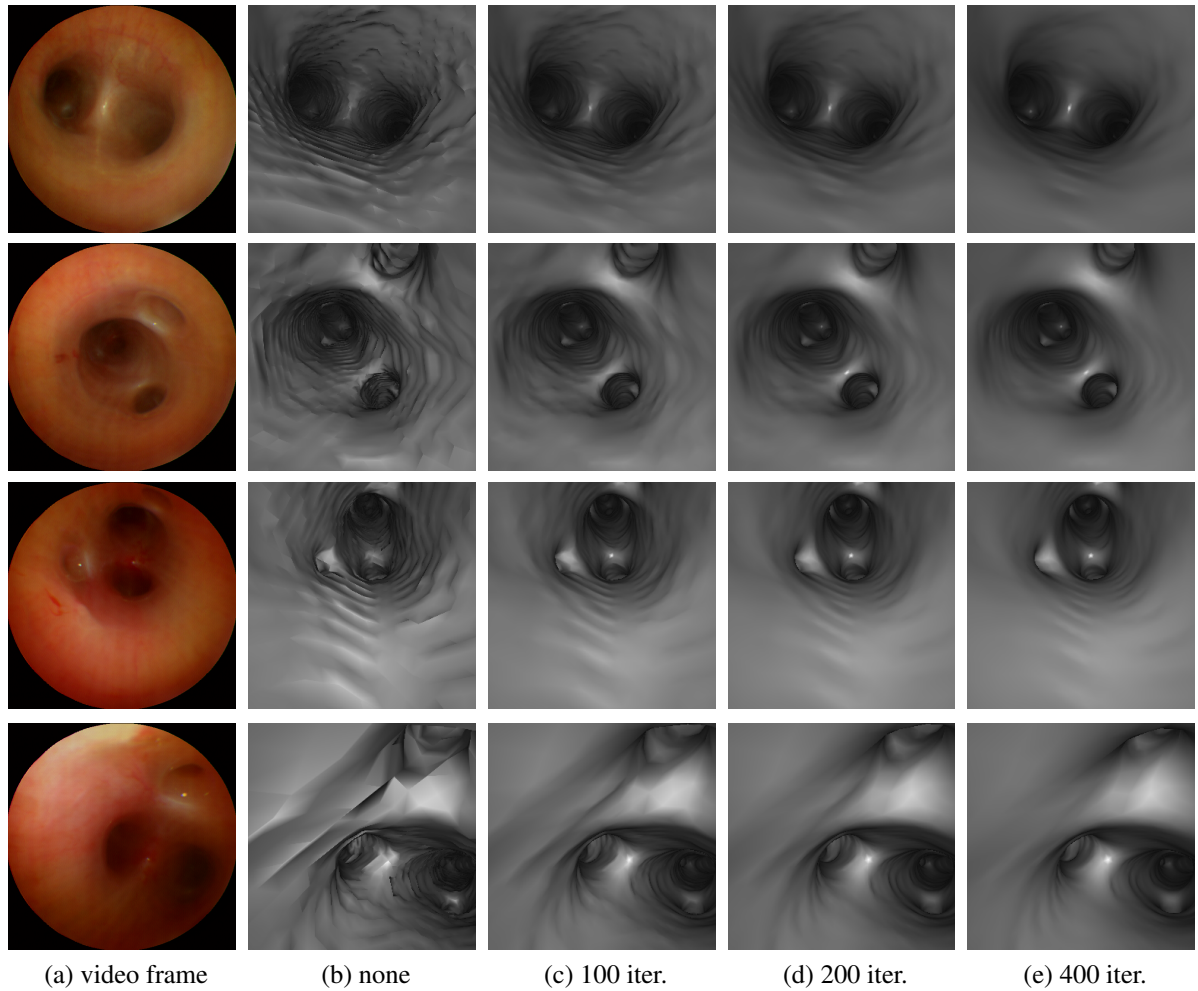


Figure 3.8: Four bronchoscopic video frames (a) and the corresponding virtual reconstructions using 0 (b), 100 (c), 200 (d), and 400 (e) smoothing iterations. From the results, 200 smoothing iterations were used for smoothing of the extracted polygonal surface mesh.

between real and virtual perspectives establishes confidence in correct localization of the bronchoscope during a procedure, guidance requires explicit navigational cues at each bifurcation. A simplified centerline model of the airway anatomy is computed, defining the medial axis of each airway, and a definitive branchpoint location at which two child airways intersect a parent airway. In much the same way that a map provides an element of navigational perspicuity through a simplified schematic of the roads, clear delineation of a 3D path through the airways, including bifurcating points, are vital for intraoperative guidance that is intuitive to the user.

Through centerline analysis, the segmented airway volume is processed and represented as a hierarchical tree structure which defines, for each airway, the curvilinear medial axis and branch point position. These centerlines enable ease in navigation within virtual or real bronchoscopic applications. Virtual exploration of the airways allows the bronchoscopist to review for a procedure or non-invasively investigate a surface abnormality [154, 89, 90]. By simple mouse motion, real bronchoscopic motion can be simulated along the airway centerlines as it is maneuvered through the airways. During a live bronchoscopic procedure, the centerline tree can be used to display a high-lighted path that coincides with the intended course of travel at each bifurcation, preventing incorrect steering of the scope [56, 156]. In some tracking applications, bronchoscope localization is often confined to centerline points only, thereby preventing mismapping of the bronchoscope position to extraluminal spaces [2, 156]. Alternatively, the centerline points themselves can be used in conjunction with tracking data to intraoperatively refine registration between the EMT system coordinates and the preoperative CT image coordinates [20].

3.3.1 Methods

Centerline analysis has been researched for characterization of a variety vessels in medical images. In the work of Aykac *et al.*, airway branchpoints were detected as the splitting of a 3D region on successive CT slices, providing discernible anatomical reference points [3]. Wink *et al.* proposed a more direct approach for blood vessel centerline delineation using

image data itself rather than the segmentation result [162]. Yu *et al.* computed centerlines of the branching vascular tree from the precomputed surface model, demonstrating smoother centerlines that form less disjointed splits at each branchpoint [172]. The more popular approaches, such as those proposed by Mori *et al.* [102], Kiraly *et al.* [74], and Palagyi *et al.* [106] have implemented thinning algorithms that reduce a segmented airway volume into a single voxel-wide centerline component. Below, a similar approach is described for comprehensive centerline analysis of images as part of the image processing pipeline.

Definition of the airway centerlines proceeds through topological analysis of the segmented airway mask, I_S . A thinning algorithm is implemented to skeletonize the airway regions, yielding a single voxel-wide component along the central axis of the airways. From the thinned image, centerline voxels of individual airways are identified and represented by a smooth centerline. The final tree T is an array of branches, (b_1, b_2, \dots, b_n) , each of which is a structure comprised of a set of 3D points which define the central axis, an index to the parent branch, and indexes to subsequent child branches. From this, the centerline geometries are fully specified as well as the respective connectivities of each airway to parent or child airways. Extraction of the centerlines analysis from the initial airway segmentation is broken into stages: end point detection, homotopic thinning, loop elimination, recentering, and finally conversion to a spline-based model. Each of these stages are described in fuller detail below.

3.3.1.1 Endpoint Detection

The process of homotopic thinning involves erosion of successive voxel layers in a 3D object. To prevent over-erosion of meaningful topology or disintegration of small airway voxels, endpoints are detected and preserved within the final thinned result using the method of Kiraly *et al.* [74]. To start, a root site is selected at the very top of the trachea. This is done by locating the uppermost 2D slice in I_S and setting the center-most voxel of the trachea region as the root site. Two distance transforms are applied to the airway mask I_S , producing an outer edge distance image I_{out} and a root distance image I_{root} , which label for

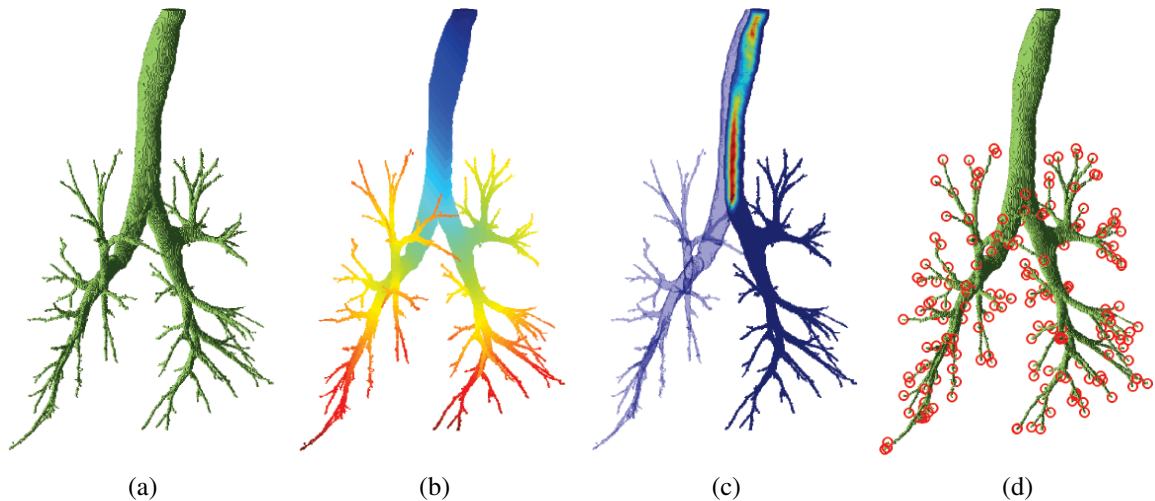


Figure 3.9: Detection of endpoints in I_S (a) proceeds by first applying quasi-Euclidean distance transforms to specify the root distance (b) and border distance (c). Endpoints are defined by regions at which the root distance reaches a local maxima (d). If neighboring points are both equally maximal, the point with the larger border distance is selected.

each pixel, the pseudo-distance to the nearest border voxel and path length to the identified root voxel, respectively. From this, endpoints are defined as voxels in I_{root} with a locally maximal path distance from the root site within the N_{27} neighborhood. For pixel clusters in I_{root} that share a locally maximal path distance, the pixel with the largest edge-distance found in I_{out} is selected as a candidate endpoint.

3.3.1.2 Homotopic Thinning

Homotopic thinning is applied to I_S to represent each airway by its medial axis. Thinning, of I_S progresses in a distance-ordered fashion, in which outer layers of the segmentation are recursively eroded away while preserving the underlying airway tree homotopy. The output image I_{tree} is initially set equal to I_{out} . Endpoints identified in the previous section are set to a value ∞ , ensuring that they will be preserved in the final skeletonized result. In the first pass of the algorithm, all voxels which lie on the inner border ($d=1$) are processed first. For each voxel in the current layer, a determination is made as to whether the voxel is

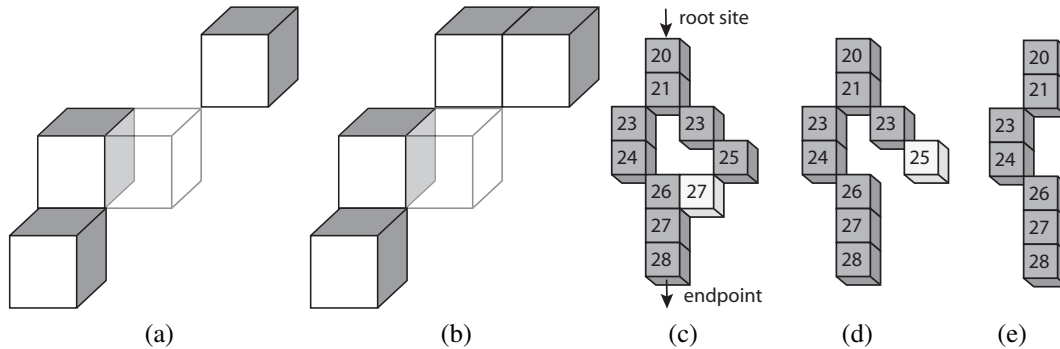


Figure 3.10: Simple-connected voxels result in a broken or multiple components as a result of its deletion in N_{26} (a). Deletion of a non-simple (b) connected voxel does not alter the homotopy. The skeletonized tree contains a loop that requires deletion (c). After deleting the loop voxel (d), false endpoints are removed until remaining points are simple.

simple-connected to I_{tree} using the criterion of Saha *et al.*[117]. This is determined for each voxel x in the N_{26} neighborhood, where $N_{26}(x)$ represents the neighborhood connected to a center voxel x , but excludes x itself. Simple-connectedness is established if $N_{26}(x)$ contains more than a single component. Figures 3.10a and 3.10b illustrate the difference. Each voxel at the distance d is recursively checked until no more voxels can be removed. Underlying layers are then processed from $d = 1, 2, \dots, d_{max}$ where d_{max} is the maximum finite border distance in I_{tree} .

3.3.1.3 Loop and False Endpoint Elimination

Homotopic thinning reduces volumetric features of I_S into medial axis components in (I_{tree}) . Although the airways are shaped as tubular structures that can, in theory, be represented by a single central axis, small undulating surface features commonly produce several false centerlines or loops that carry no real anatomical relevance. A loop and false endpoint elimination stage is therefore added to the pipeline to rectify these artifacts in I_{tree} . First, a distance transform is applied to I_{tree} , labeling each voxel with its path distance from the root site. Loops are identified as simple connected voxels which connect to two non-

neighboring voxels with a lesser path distance. Figure 3.10c illustrates such a scenario in which a loop is identified. The highlighted voxels connects to two separated voxels with lower path distances and is subsequently deleted (Figure 3.10d). The remaining false branch is removed by deleting false endpoints (i.e. voxels that are not simple-connected and which are not labeled with a distance of ∞).

3.3.1.4 Recentering and Branch Labeling

Prior to the conversion of the discrete image I_{tree} into an analytic expressions of centerlines, simple recentering and branch labeling routines are undergone. Recentering recursively checks each voxel \mathbf{x} in I_{tree} to see if it can be better centered by moving the voxel to $\mathbf{x}_{new} \in N_{27}(\mathbf{x})$, increasing the border distance from $I_{out}(\mathbf{x})$ to $I_{out}(\mathbf{x}_{new})$ without breaking homotopy. A branch labeling routine assigns each voxel $\mathbf{x} \in I_{tree}$ to a branch b_i , where b is an array of n branches, from b_0 to b_{n-1} , and each branch b_i is an array of m_i voxel positions $[\mathbf{x}_{i,0}, \mathbf{x}_{i,1}, \dots, \mathbf{x}_{i,m_i-1}]$. To start, the number of branches n is initialized to 1, and \mathbf{x}_{root} is set as the first element of b_0 . Neighboring voxels are iteratively added to b_0 in increasing order of path-length $I_{root}(\mathbf{x})$ up to the first branchpoint located along the centerline. Child branches b_1 and b_2 are subsequently initialized to the respective downstream voxels, $\mathbf{x}_{1,0}$ and $\mathbf{x}_{2,0}$, that neighbor \mathbf{x}_{0,m_0-1} (the last point in the parent branch). For each new branch b_i created, connectivity is established by an array of parent and child labels L_p and L_c , respectively. Each branch is processed in this manner until all voxels are assigned a label.

3.3.1.5 Spline Conversion

Once the branches are defined by b , each is translated into a smooth differentiable 3D contour that approximates the true centerline of the anatomy and is not overly sensitive to the integer step changes that are present in the voxel-based centerlines of I_{tree} . To approximate the general airway contours, a B-spline is used to parametrically model the central axis as a continuous and differentiable curve $\mathbf{x}_c(t)$. The B-spline is a generalization of the Bézier curve which consists of a set of N control points \mathbf{p} , and knots $\mathbf{t} = [t_0, t_1, \dots, t_M]$,

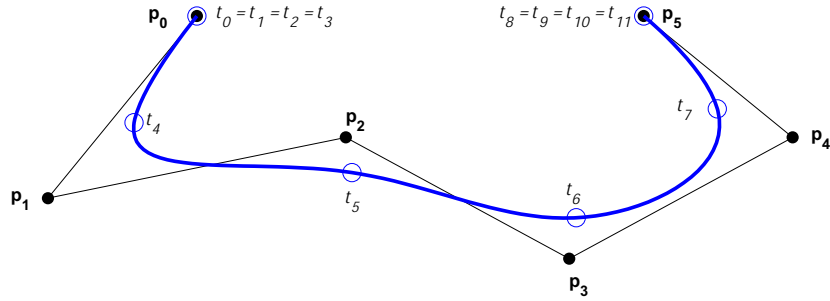


Figure 3.11: Example of a B-spline containing control points \mathbf{p} and knots \mathbf{t} .

where $0 \leq t \leq 1$. Figure 3.3 depicts a 2D example in which a set of points are modeled by a B-spline. The spline curve $\mathbf{x}_c(t)$ is evaluated by:

$$\mathbf{x}_c(t) = \sum_i^n B_{i,j} \mathbf{p}_i \quad (3.3)$$

where the basis function $B_{i,j}$ is computed from:

$$B_{i,0}(t) = \begin{cases} 1 & \text{if } t_i \leq t < t_{i+1} \text{ and } t_i < t_{i+1} \\ 0 & \text{otherwise} \end{cases}$$

$$B_{i,j}(t) = \frac{t - t_i}{t_{i+j} - t_i} B_{i,j-1}(t) + \frac{t_{i+j+1} - t}{t_{i+j+1} - t_{i+1}} B_{i+1,j-1}(t)$$

where $j = 0, 1, \dots, k$, and k is the order of the spline, given by $k = M - N$. From Figure 3.3, the start and end knots are multiplied to produce the desired order $k = 4$. The control points, \mathbf{p}_0 and \mathbf{p}_{N-1} are also duplicated to permit point discontinuity at start and endpoints, respectively.

The B-spline works well for computation of the airway centerline, for the reason that $\mathbf{x}_c(t)$ is not constrained to pass through each voxel position, thus sparing the appearance of stepping in the curve between voxel positions. This also precludes more exhaustive centering algorithms that are required for explicit curve definition using cubic spline-based

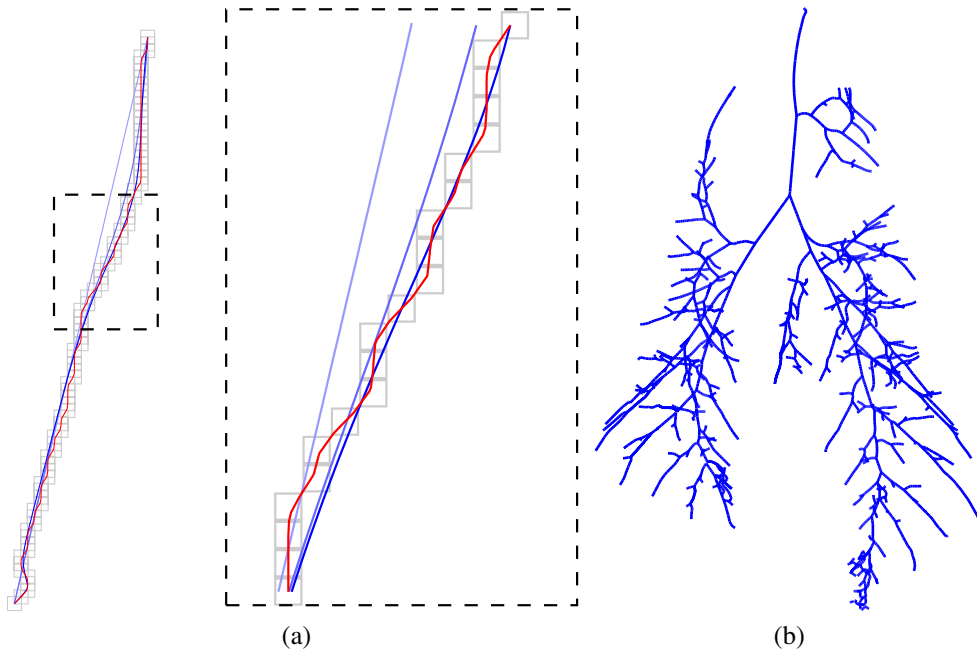


Figure 3.12: B-Spline approximation of the airway centerlines. The voxels comprising the trachea centerline are converted to a B-spline (a). Control points are added until spline contour adequately models the true centerline (*blue*), though if too many control points are added the contour will model the discrete step changes in voxel positions. The final centerline model of the airways of a pig is displayed (b).

axis generation [74].

For each branch b_i , a spline is used to evaluate the curve using, at first, only the start and end points $\mathbf{x}_{i,0}$ and \mathbf{x}_{i,m_i-1} , which produces a straight line. For each point $\mathbf{x}_{i,j}$ in b_i , the minimum distance d_c is computed as the distance between $\mathbf{x}_{i,j}$ and the curve \mathbf{x}_c . If d_c is larger than a threshold ε , $\mathbf{x}_{i,j}$ is added to the list of control points. For each point $\mathbf{x}_{i,j}$, ε is set to $0.4 \cdot I_{out}(\mathbf{x}_{i,j})$, which allows larger values of d_c in larger airways.

3.4 Discussion

This chapter has given a description of the preprocessing software stages used in the conversion of CT image data to a virtual airway model. As part of the development, all software

was written in-house in MATLAB using a number of techniques presented in literature. Exception is made for the surface generation software that was borrowed from VTK. The resulting software pipeline represents a best attempt at analysis of a limited number of chest scans. The output produced viable virtual models of the airway anatomy.

Currently, airway segmentation presents the most significant challenge to clinical implementation. First, the segmentation algorithm fails to identify many of the small peripheral airways that are visible on CT scan slices. At the present scan resolution, it is difficult to assess the diameters at which airways tend to elude segmentation given these small airways are only one or two voxels in diameter. In many cases, such airways may prove to be inaccessible to the SFE. However, this limitation can be easily resolved with minimal user intervention. Although segmentation of a multitude of small airways isn't feasible, bronchoscopy is targeted for a single biopsy site. Thus manually editing segmentation along only one or two airways to reach a region is within reason. Interactive tools have been developed to permit user-specified corrections to the initial segmentation.

Following segmentation, surface generation is also limited for very small airways. At the voxel scale, airways appear blocky or are disconnected by smoothing of the airway surface. This produces a topology that is not representative of the actual airway anatomy. Further research into this issue is lacking as bronchoscopes are large and used for navigation within the more central airway anatomy that is suitably characterized by the computed surface model. The quality is ultimately dependent on the image resolution. However, some alternative approaches have been proposed and should be considered for future use. [37] *et al.* proposed a dilation of small airways that results in a virtual surface that is not contrived from isovalue extraction. Due to poor visualization of small airways, Geiger *et al.* used a virtual surface of adjacent pulmonary arteries as a surrogate model of the airway anatomy [34]. In the future, experimental testing of the SFE will need to be performed to deduce whether bronchoscopy beyond the virtual airway model should be anticipated as an unavoidable occurrence, and to what extent these allowances would remedy surface generation for peripheral airways.

Table 3.1: Processing times for the individual processing stages given a CT image with 0.5 mm resolution and a volume of $228 \times 206 \times 486$.

	Lung Segmentation	Airway Segmentation	Surface Generation	Centerline Analysis	Total
Time (s)	215.35	379.35	115.70	89.20	799.60

The processing time of the pipeline based on a sample CT scan is given in Table 3.1. Overall, more than 13 minutes are required to process the image in computing the virtual airway model. Processing was performed on a Dell Precision Workstation (3.43 GHz, 4 GB RAM) running on the Windows XP platform. Though somewhat lengthy, the preprocessing is not deemed to be critical to the clinical workflow. First, a preoperative CT scan is commonly acquired well before a procedure is scheduled. Following referral for bronchoscopy, the clinician would be permitted sufficient time to process, review, and plan for a future bronchoscopy. Although, more expedient algorithmic approaches are likely possible, the framework developed here is not considered a final implementation and was not optimized for speed. More rapid virtual modeling may be considered, should an intraoperative CT be necessary.

Chapter 4

USER INTERFACE DESIGN

In Chapter 3, software tools were developed for analysis of the CT image data, including segmentation of the airways, virtual surface generation, and centerline analysis. In this chapter, software is devised for visualization of these elements and their interaction by the user. The interface software is broken into two components to reflect clinical workflow, including preoperative planning and intraoperative guidance. The preoperative planning utility allows the clinician to identify the target location of a nodule and plot a course to the biopsy site. During intraoperative guidance, the bronchoscopist references both the bronchoscopic video and the virtually displayed path to navigate to the lesion.

Both the preoperative and intraoperative utilities were built around the Visualization Toolkit or VTK¹ (Kitware). This open-source software provides a set of C++ class libraries for 3D graphics, visualization, and user interaction. Applications are constructed around Qt (Open Source Edition)² graphical user interface (GUI) framework. Although all code is cross-platform, applications were developed on Precision 470 (Dell) workstation running Windows XP.

4.1 Preoperative Planning

Before bronchoscopy can be performed, the clinician must specify a path along which the scope is to be navigated to access the identified lesion. The preoperative planning utility

¹www.vtk.org

²www.qtsoftware.com

provides visualization of the CT image to both establish a target lesion location, as well as to select an automatically generated path, via airway centerlines, to the region of interest. An overview of the application functionality is demonstrated in the example below as well as previous work [2].

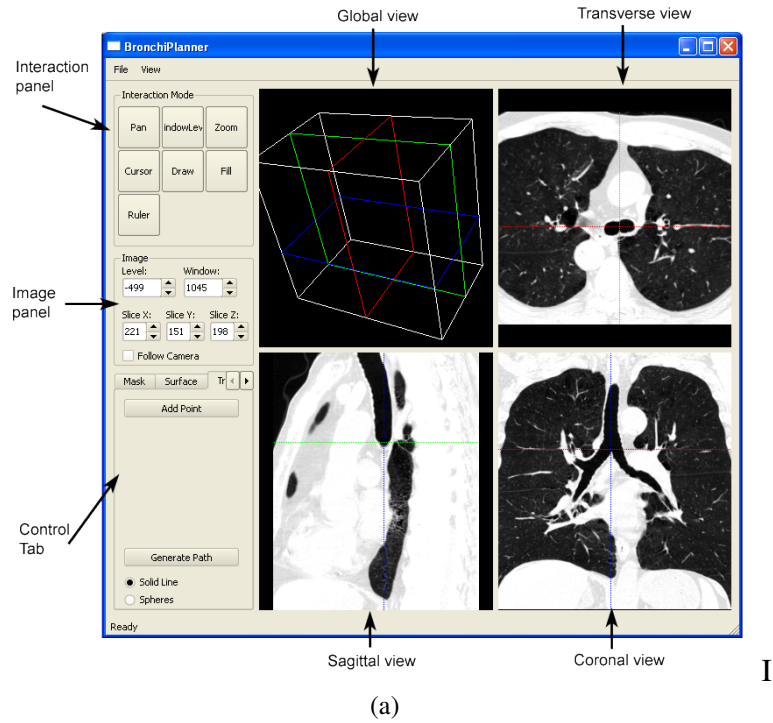
The interface of the preoperative planning utility includes four windows for visualization and interaction of the image data elements. Patient specific data is loaded through the file menu, including the CT image, surface, and centerline models. The top-left window displays the global perspective view of the image volume, which can be easily rotated, translated and zoomed to focus on a particular point of interest. Within the image volume are three slice outlines that identify the locations of the transverse, sagittal and coronal slices. These are depicted in 2D orthographic windows at the top-right, bottom-left, and bottom-right. The cursor position corresponds to the intersection point of all three planes. The user can efficiently scroll through the CT image stack in any plane by holding down the right mouse button and moving the mouse. Figure 4.1a illustrates the utility after loading patient image data. The sidebar allows easy switching between different interaction modes as well as specifying visualization parameters. The following is a list of the interaction modes and a short description their functions:

Scan: Marches through CT image slices in all three dimensions. This is always controlled by the right mouse button.

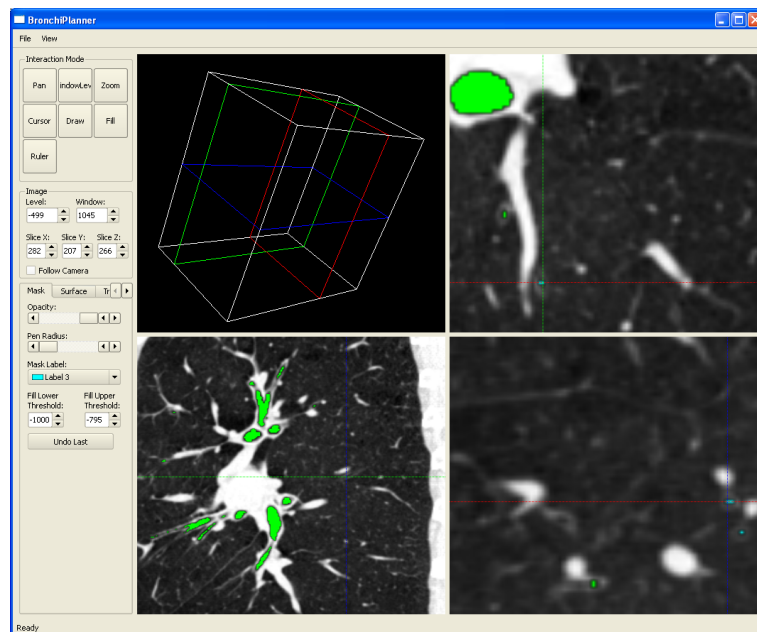
Pan: Translates the camera orthogonal to the view direction to better position the center focus.

Window\Level: Motion of the mouse in x - and y - axis control the window and level of the grayscale CT image in each of the ortho planes.

Zoom: Controls the magnification within a view window



(a)



(b)

Figure 4.1: The preoperative planning utility after loading the CT image of a patient.

Cursor: A cross-hair target is used to select a point of interest in the image. Every ortho view image is adjusted after the cursor click so that transverse, coronal, and sagittal view planes intersect at the site of the cursor.

Draw: A pen-style tool allows for the manual image segmentation.

Fill: Performs a 2D flood-filling operation within lower and upper grayscale bounds.

Ruler: Measures distance (in mm) between two points in an image plane.

4.1.1 Image Interaction

The CT image is the foundational data source around which the virtual airway model is constructed. After loading the image, the window and level values are set to optimize contrast at the desired HU value. The image panel contains numeric controls that both display and set the window and level values as well as the slice index for all three image planes. For the CT image in Figure 4.1a, the window and level are is for contrast between air and tissue HU values.

In addition to the image, a mask can simultaneously be loaded, which displays the results of automatic or manual segmentation. For the image mask, each integer value defines a different label, each assigned its own unique color. Zero-valued pixels are assigned a transparent color. Figure 4.1b depicts the results of the automatic segmentation in green from the previous section. To turn the mask off, the mask control tab contains an opacity slider that can be moved to visualize underlying image data.

4.1.2 Manual Segmentation

The results from automated segmentation frequently miss very small airways that are only a voxel or two in thickness. The preoperative planning utility is equipped with segmentation editing tools to refine segmentation, especially for small unsegmented airways near a region of interest. A pen tool can be used to directly write over the mask with any preferred label.

This allows for distinct management of automatic and manual segmentation outputs. Figure 4.1b shows two small airways in the coronal plane that were unidentified during automatic segmentation. The pen tool was used to label the regions. A larger pen radius can be specified by sliding the pen radius slider on the mask control tab.

Flood fill operations can also be performed for larger portions of unsegmented airways. This first requires setting upper and lower HU threshold values for the fill. Once the fill mode is selected, a 2D region is flood-filled following clicking of the mouse on a particular region. Practically, segmentation by flood-filling requires iteratively optimizing the threshold values until the desired result is achieved. Subsequently, over-filling commonly occurs. The application maintains a comprehensive list of each pixel added to the mask region as part of each fill or draw operation. By clicking on “**Undo Last**”, the segmentation reverts back to its state prior to the last action.

4.1.3 Path Definition

4.1.3.1 Target Identification

The preoperative path planning utility provides easy identification of a target lesion and definition of a 3D path that leads to the region. First, the lesion is located in the CT image slices. Figure 4.2 shows an SPN located at the cursor point in all three orthogonal planes. A target is then selected by scrolling to the “**Target**” tab and selecting “**Add Target**”. A yellow spherical target widget then appears at the cursor location. The term widget is used to describe a graphical object in VTK that has built-in interactive features. After selecting the widget, the mouse can be used to move and grow or shrink the target.

4.1.3.2 Path Selection

Once the target lesion is located, the user must specify a path to the biopsy site. This is provided through the centerline model that was extracted from the previous chapter. After loading the centerline tree, a custom tree widget was developed to allow automated path

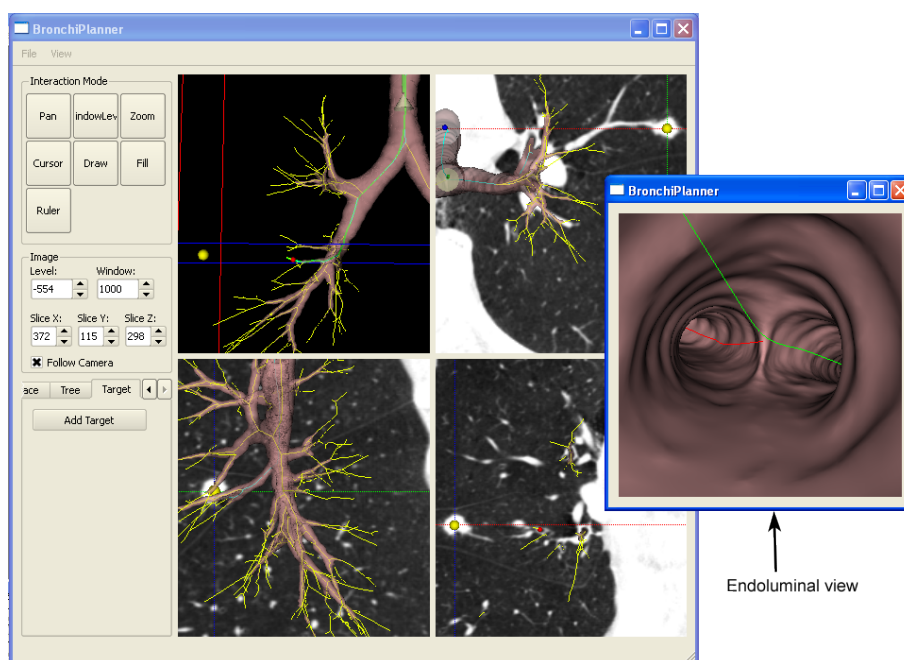


Figure 4.2: Selection of a 3D path to an identified nodule. After locating a target lesion, a 3D path is generated from selecting the nearest centerline point. A virtual endoluminal view displays a highlighted path leading to the region of interest.

generation by selecting any point on the tree. By default, the path start is represented as the first point along the trachea (*blue sphere*). After selecting a point on a branch (*red sphere*), a path is highlighted by recursively connecting upstream branches up to the trachea. An optional endoluminal view provides a realistic bronchoscopic perspective of the anatomy. The highlighted path instructs virtual navigation along the predefined path. The global views depict the scope location as it is moved along the path. A red path indicates an incorrect route.

4.1.3.3 Path Extension

For lesions that fall outside the segmented airway tree, manual extension of the path is necessary. In Figure 4.3, the lesion is located, but lies well beyond the range of the identified branch centerlines. By scrolling through the slices, it is possible to better visualize a

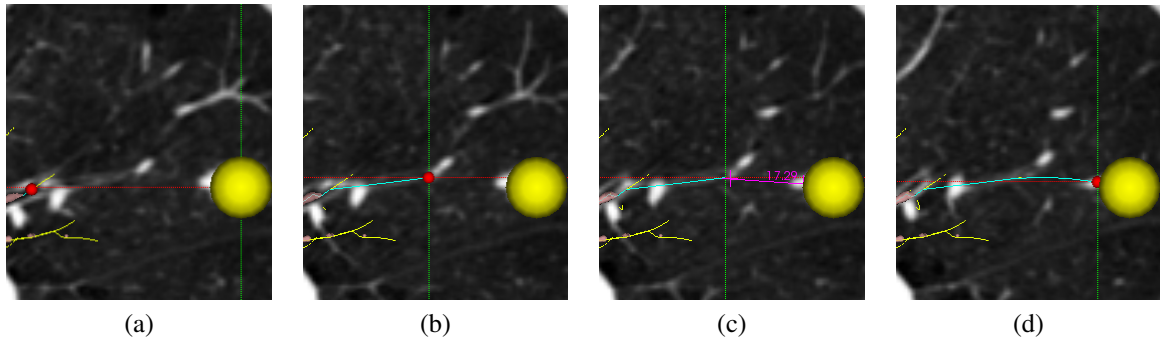


Figure 4.3: Manual path extension to reach an peripheral lesion. After locating a peripheral SPN, the target widget is used to define the position and size of the lesion. Because no airway directly accesses the lesion, the nearest proximal airway is selected (a). To account for limitations in the segmentation, the path is extended along an adjacent visible airway (b). Following, the airway cannot be tracked at a position of about 17 mm from the front of the SPN (c). The path is extended to the lesion using a pulmonary blood vessel as a surrogate (d).

small airway that extends beyond the segmented portion of the airways. This is somewhat difficult for peripheral airways due to the fact that partial volume effects blur these small airways, and are often cloaked by bright blood vessels that parallel the bronchial passages. In the example depicted in Figure 4.3, the CT scan acquired had a 1-mm voxel resolution, where those obtained from pig experiments were on the order of 0.5 mm, implying that improved resolution may markedly benefit segmentation and automated modeling of these small airways. Ultimately, the small airway could not be tracked, where the distance to the front of the lesion was measured at over 17 mm. The path was finally extended to meet the lesion.

4.2 Discussion

The preoperative path-planning utility presented in this chapter has been effective for visualization and interaction with virtual image data as well as preparation for future procedure. To this point, demonstrating effective guidance based on preoperative planning has been limited. CT imaging and bronchoscopy of the live pigs was performed all within the

same night, which did not allow for sufficient time for the image acquisition, transfer, analysis and planning. Furthermore, inability to steer the SFE tip at this stage has precluded navigation to a user-defined position, as extension of the scope is more or less limited to the mainstem bronchi. At present, a number of functionalities could be added to the interface including virtual bronchoscopy, marking a biopsy site, or generating multiple paths for surgery. However, the purpose of this utility was to demonstrate minimum functionality as part of the clinical workflow involving the detection, planning, and operative stages.

A poignant concern of guided SFE and biopsy of SPNs is that such lesions may lie beyond the accessible airway volume. It is perceived that SPNs are situated randomly throughout the airways with a slightly higher prevalence in the upper lobes. However, due to lack of experience in the bronchoscopic examination of small peripherally positioned SPNs, planning may be hindered by two main factors. First, small airways not only evade detection by automated segmentation, but visual tracking of such small airways may be difficult for the operator. In many cases, it may not be apparent whether an airway accesses the SPN or whether it may be a significant subsurface distance from the nearest point. Within regions where an airway can be identified, accessibility of the airway to the SFE may not be assessed to the inability to precisely estimate small airway diameters at the current CT image resolution.

Given current limitations in exploratory use of the scope within either live animal or human studies, an initial evaluation of accessibility of SPNs to the SFE was conducted using only those airways detected on the CT image. An airway distance map of the segmented lung volume was performed using ITK. This computed the shortest Euclidean distance of each lung voxel to the nearest airway, thereby providing an upper bound of the penetration distance that would be required to access a subsurface SPN. Figure 4.4c portrays the histogram of distances associated with each voxel contained within the lung volume. From the front and side projections, a maximum distance of 40 mm is observed. The mean distance of a randomly position SPN, however, is only about 10 mm, or 1 cm.

Though future in vivo validation of the SFE and associated biopsy techniques will need

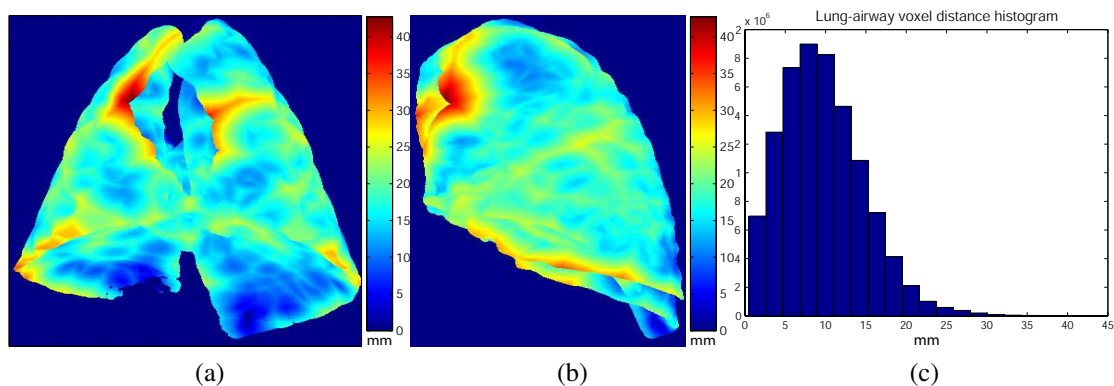


Figure 4.4: A computed lung-airway distance map is depicted in the form of maximum intensity projections from both front (a) and side (b) views. A histogram (c) shows the relative distribution of lung voxel distances to the nearest airway.

to be evaluated for a host of patients with a variety of SPNs of different sizes and locations, the results of this analysis seem feasible as aspiration of nodules 1-2 cm from the nearest airway are commonplace in bronchoscopy. The virtual model extracted from the previous model provides an interactive roadmap that can be used to immediately generate a path through the airways to reach a lesion. For SPNs that lie outside this roadmap, manual segmentation and path extension to reach an SPN was achieved through incorporation of interactive functions in the planning GUI.

At present, there is some uncertainty as to how planning will translate to physical biopsy of an SPN. In conventional bronchoscopy, a needle insertion depth of 1 cm is commonly achieved. However, the functionality of biopsy or aspiration of such SPNs within the peripheral airways are unknown. Factors such as depth, relative orientation of adjacent airways to the nodule, and needle or forcep sizes should be considered. Likewise, it is possible that cytological brushings within airways adjacent to subsurface lesions may produce specimens that reflect underlying pathology. Ultimately, future approaches to preoperative planning for SFE-guided biopsy of SPNs will be dictated by trial and error as clinicians examine airway regions that may appear anatomically and pathologically foreign.

Chapter 5

ELECTROMAGNETIC NAVIGATION WITHIN A RIGID LUNG MODEL

The virtual components developed in the preceding chapters provide a roadmap of the anatomy to be used for guided navigation of the SFE. To localize the SFE, an electromagnetic tracking (EMT) system is used by attaching a miniature (1.3 mm) sensor to the scope's distal tip. During a procedure, EMT records the position and orientation of the SFE with six degrees of freedom (DoF) in real time. Once the registration between the operative environment and CT image is performed, the SFE position can be mapped onto the virtual airway model to display the position along a path to the lesion. Below is a brief introduction to tracking technologies and their role in medicine as well as a number of factors that effect EMT performance. A rationale is given for the EMT system purchased for SFE guidance and results are presented for preliminary tracking studies within a rigid lung model.

5.1 Background

There is often great difficulty in guiding catheters, endoscopes, or operative instruments to desired locations within the body. Incorrect positioning of such tools can result in misdiagnosis or potentially deleterious complications. As a result, these procedures are heavily dependent on intraoperative imaging modalities, such as CT or fluoroscopy, to ensure proper guidance. Unfortunately, imaging systems are expensive, health compromising, and cumbersome. Non-radiologic tracking of endoscopes, catheters, and other instruments have become extremely valuable in the medical field to improve navigation through anatomy that

is not directly visible.

EMT has garnered a high level of interest from the medical field as a means of determining the position and orientation of a device in the body in real time. While EMT has been used for nearly 30 years for a variety of applications, it is the advancement toward one millimeter sensor sizes that has launched this technology to the forefront of several guided-therapy innovations. Applications of EMT already include electroanatomic mapping of the heart [36, 25], laparoscopic surgery [129, 58], prostate biopsy [166, 73], neuronavigation [39, 137, 78], and bronchoscopy [6, 26, 120]. The benefits offered by EMT include: 1) the ability to define position in 6 DoF; 2) no requirement for line of sight or rigid stereotaxis as is associated with optical tracking technologies; 3) localization accuracies of ~ 1 mm; 4) low relative cost and 5) highly adaptable to a clinical environment.

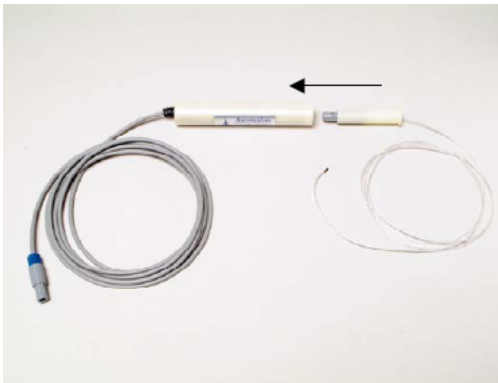
The components of EMT systems include a transmitter or field generator, sensor, and central processing unit. Within the transmitter are a set of coils used to generate a magnetic field. The sensor houses a set of coils placed at orthogonal orientations which produce a voltage proportional to the change in electromagnetic flux within the. The induced voltage is then measured by the central processing unit to compute the position and orientation, typically with an error of 1-2 mm and 1-2°. For EM tracking of the SFE, the 3D Guidance medSAFE system (Ascension Technology Corporation, Burlington, VT) was used for the unique advantages it offers over other commercially available systems. These include: very small sensor sizes (down to 1.3 mm), simultaneous tracking of 4 sensors, a sufficiently large tracking volume, high tracking accuracy, and superior insusceptibility to metallic distortion. Figure 5.1 depicts the central unit, sensor, and flat transmitter that comprise the 3D Guidance system.

5.2 Evaluation of EMT Accuracy

The large number of electromagnetic tracking systems and applications for which this technology has been proposed has substantiated the need for independent performance metrics.



(a) central processing unit



(b) sensor and pre-amplifier



(c) flat transmitter

Figure 5.1: The 3D Guidance medSAFE system (Ascension Technology Corporation, Burlington, VT), including the central processing unit, sensor and attachable pre-amplifier, and the flat transmitter. Images were acquired from the *3D Guidance medSAFE Installation and Operation Guide*.

Over the last decade, multiple researches have focused on characterizing EMT system accuracy under different scenarios. Static sensor accuracy has been quantified by placing the sensor into slots of a plastic calibration grid machined at high tolerance [19, 63]. Some investigations have undergone comprehensive mapping of 6DoF accuracy and precision throughout the tracking volume using a robotic arm [32]. Dynamic accuracy assessment has been an area of EMT research interest. In the work of Nafis *et al.* dynamic accuracy was quantified by manually scribbling the sensor over a flat surface [103]. Schneider and Stevens proposed a simple characterization of dynamic accuracy by affixing two sensors together and measuring the recorded differential distance while freely weaving them through the tracking space [119]. A more systematic approach by Hummel *et al.* employed a specialized pendulum to gauge motion tracking of an EMT system [65].

Although EMT systems are useful for tracking objects through a known space, a majority of medical applications require tracking for precise registration between the procedural coordinate system and an image-based coordinate system. In this scenario, performance of the tracking system is related both to fiducial localization error (FLE) and the subsequent registration error between procedural and image coordinate systems. With this in mind, Fitzpatrick *et al.* proposed specific registration error metrics, termed: *fiducial registration error* (FRE) and *target registration error* (TRE) [31], where FRE is the error between the located fiducials following registration between two coordinate systems and TRE is the registration error of all other points. Measurements of FLE, FRE, and TRE have been used frequently in the tracking of ultrasound scanheads [81, 64], and assessing tracking accuracy within fluoroscopic[170] and CT imaging [124] environments.

5.2.1 Results

The accuracy of the 3D Guidance medSAFE system has been reported on previously by several researchers [119, 169]. To measure the FLE of the EMT system, the stylus calibration of Leotta *et al.* was used [81]. In this system, a sensor was attached to a stylus and rotated around a common pivot point. Figure 5.2a illustrates the setup and the stylus used

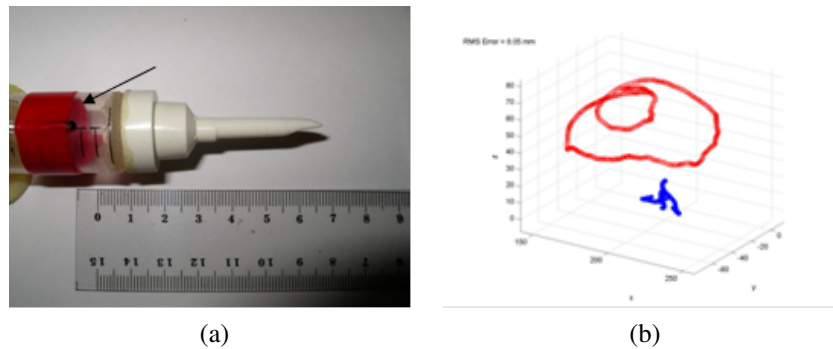


Figure 5.2: The EMT accuracy is measured by FLE using a tracked stylus. The sensor is attached to a rigid stylus (a) and a plot of the sensor trajectory and computed stylus centroid are pictured (b).

for navigation. Figure 5.2b depicts the localization accuracy of the stylus tip following after computing the stylus vector in sensor coordinates from the method proposed by Hartov *et al.* [48]. The performance of the EMT system resulted in a FLE of 2-3 mm for most tests. The FLE in this experiment is owed to both the sensor system, but as well some slippage that occurs at the contact point of the stylus tip. However, the overall FLE is most relevant to performance likely to be observed during a procedure.

5.3 Navigation of a Dried Sheep Lung

For initial testing of the EMT system, a dried sheep lung was fixed within a plexiglass container. A tracheal opening was placed in the side of the box to permit easy insertion of the EMT. Small holes were drilled into the frame of the box that accommodated the sensor. The centroid of the sensor holes were manually located on the CT image. The FRE of the registration between world and image coordinates was 1.01 mm for the sessions.

5.3.1 Results

Tracking within the rigid sheep model is plotted in Figure 5.4. The sensor was simply passively extended into the model. In some regions, the sensor may have gotten caught on

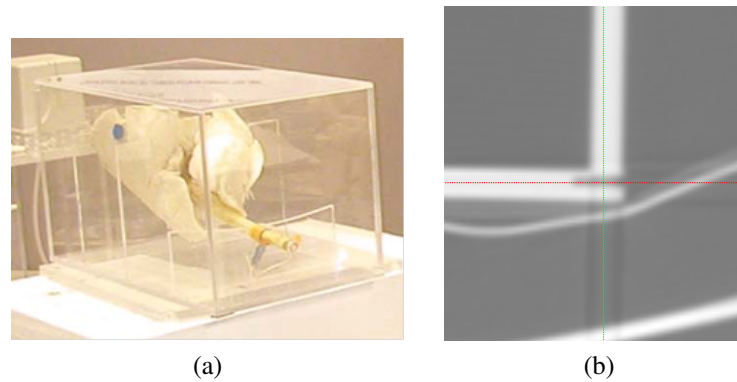


Figure 5.3: The dried (rigid) sheep lung model encased in a plexiglass box (a) and localization of the sensor slot on a slice of the acquire CT image (b)

an edge of the lung or was flipped to quickly. This is evident from small points where the sensor jerks away from the plotted path. To assess registration error, the minimum distance between the recorded sensor position and the nearest centerline point was computed. The average error was approximately 6.1 mm.

This metric value combines a number of sources of error. First, FLE is inherent in the registration process as there is certainly misalignment between position located within the CT image and that recorded by the sensor. For instance, it is assumed that the sensor position is roughly recorded from the sensor centroid. This assumption may be incorrect, or possibly, such error may depend on the sensor position relative to the transmitter. The point to point registration error is also limited by using only three points. In practice, determination of a rigid registration is improved in an overdetermined system using multiple sensor readings. Lastly, the FRE presumes that the sensor travels along the centerline of the airway model. In actuality, the sensor most likely slides along the airway wall rather than through the centerline, contributing an error equivalent to the radius of airway being navigated. Thus the 6.1 mm discrepancy provides only an estimate of the error.

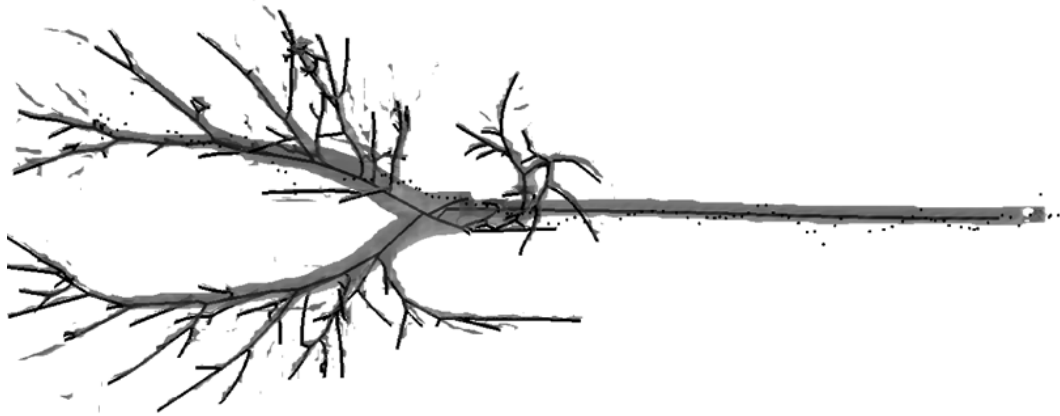


Figure 5.4: Tracking session within the rigid lung model. The central airway axes are plotted as line and the EMT sensor readings are presented as dots.

5.4 Discussion

The registration error of the navigation experiment has a number of contributing factors. First, although the FRE is very small, it is known that the TRE distribution can be much larger than that observed from FRE [30]. This may be attributed to a low number of fiducial markers, as only three were used in this case, or to high FLE either through inaccurate sensor based localization or corresponding manual localization of fiducials in an image. An unfortunate predicament of EMT is that registration is only performed initially, and runs in open-loop fashion without means of assessing TRE without the use of external measurements. However, some workarounds have been proposed. Both Wegner *et al.* and Atmosukarto *et al.* proposed reprojection of the tracked sensor position to the nearest airway centerline [2, 156]. Atmosukarto *et al.* also implemented a *particle filter* to probabilistically maximize localization along a given medial axis with accurate results [2]. Alternatively, Deguchi *et al.* and Klein *et al.* have proposed use of the iterative closest point algorithm to adaptively optimize the registration the sensor path to the centerline model [20, 76].

Though EMT performance is generally robust, it carries some limitations for navigated

bronchoscopy within a live subject. First, although EMT sensor accuracy is within the 1 millimeter range, the resulting TRE is the combination of FLE, contributed to both by the EMT system and the user. Compensation methods which use the central axis notwithstanding, the TRE may still be several millimeters, which may ultimately result in missed biopsy of an SPN. Due to the inherency of TRE, even within rigid systems, a fundamental disconnect exists between the tracked sensor position and what is seen on the SFE. This leaves the bronchoscopist to mentally bridge the gap between the EMT position of the scope seen from a global perspective and the perceived position derived from bronchoscopic video. Furthermore, these experiments were conducted completely within a rigid system, and make no attempt to account for misalignment introduced by deformable anatomy. To evaluate the efficacy of EMT within a real procedure, attempts must be made to evaluate TRE resulting from reorientation of the patient and effects of breathing. Though compensation for such anatomical motion has been attempted [157], evaluation for bronchoscopic biopsy has been limited to more central airways using a conventional bronchoscope. For localization of the SFE, consideration must be made for small peripheral airways, where airways are more densely configured and subject to larger respiratory induced motions.

Chapter 6

MODELING RESPIRATORY MOTION

In Chapter 5, the bronchoscopic guidance system was tested within a rigid benchtop model. By combining EMT within a virtual airway model, relatively accurate bronchoscopic tracking was achieved. However, within a live subject, motion resulting from shifting of body position, coughing, and breathing present significant barriers to navigation. While rigid motion of the subject can be largely monitored by externally mounted sensors, deformation caused by respiration introduces periodic misalignment between the virtual airway model and the actual anatomy. Because the goal of bronchoscopic tracking is to localize the SFE relative to the airway anatomy, such as the airways or target lesion, direct mapping between the EMT coordinate system and the static CT image coordinate system is insufficient. The resulting localization error presents uncertainty in the predicted position of the SFE relative to the airway geometry and will likely frustrate the bronchoscopist's ability to navigate correctly or accurately target the an SPN.

To evaluate the effect of respiratory motion in bronchoscopic tracking, various CT images were acquired of each pig at various phases of respiration. From these images, quantitative approximations of regional respiratory-induced motion are acquired through non-rigid registration of CT images. From this, it was possible to establish the degree of respiratory motion and the likely effect on localization of the bronchoscope. Intraoperative motion compensation is proposed as a solution by modeling the lung dynamics using the array of CT images and the resulting motion fields which co-register them. This motion is then compared to a simple linear motion model computed from only two CT images (one at full inspiration and one at full expiration). During bronchoscopic tracking, local misalign-

ment due to respiratory motion can be estimated by linear interpolation between these two phases. In subsequent sections, the accuracy and validity of this model is further discussed with regard to accurate bronchoscopic tracking.

6.1 Mechanics of Respiration

The act of breathing is balanced between inspiratory and expiratory cycles during which the lung undergoes expansion and compression. The increase in lung volume seen during inspiration is primarily accomplished through active contraction of ventilatory muscles (Figure 6.1). The muscle primarily responsible for inspiration is the diaphragm, a large dome-shaped muscle sheet that separates the thoracic and abdominal cavities. As the diaphragm descends, the thoracic cavity expands, creating a negative intrathoracic pressure, thereby inducing inhalation. Contraction of the external and parasternal intercostals further increase lung volume by pulling the ribs upward and outward. The ribs themselves hinge between sternum and spine much like a bucket handle. As they are pulled into a more horizontal orientation by the intercostal muscles, the cross-sectional area of the thorax increases. Following inspiration, energy is stored within the lung, chest wall and ventilatory muscles. Expiration then commonly proceeds through passive relaxation of the ventilatory muscles. Once this occurs, elastic energy stored in the lung and chest wall is converted to expiratory flow. As the diaphragm relaxes, the thoracic cavity compresses as lung pressure equilibrates with the external environment. Alternatively, active expiration can be achieved through abdominal and intercostal muscles. The external oblique, internal oblique, rectus abdominis and transverse abdominis actively compress the diaphragm. The internal intercostals and triangularis sterni decrease the cross-sectional area of the thorax by pulling the ribs downward and inward. The overall result is a positive lung pressure which actively drives expiration of air from the lung.

The deformation resulting from the expansion and compression of the lung between maximal inspiration and the functional residual capacity (FRC) at the end of passive expi-

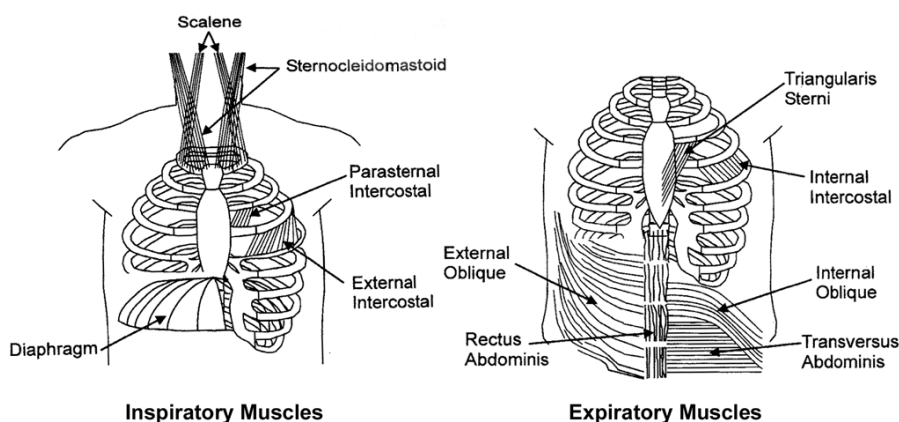


Figure 6.1: Respiratory physiology and the muscles involved in inspiration and expiration. Figure adapted from Hlastala and Berger[59].

ration is considerable. Such motion can present complications in imaging or intervention of lung diseases. Modeling of respiratory-induced tumor motion has been of great interest in the field of radiotherapy, where a lesion can be ablated through targeted delivery of radiation [127, 60, 87]. In many instances, therapy could be optimized by accurate tracking of the tumor or by gating the radiation at given breath-hold level, thereby immobilizing the lesion [118].

Figure 6.2 displays the radiographic outlines of the lungs from x-ray images of a patient at various phases of respiration. At the maximal inspiration, the lung appears significantly larger than at FRC or residual volume (RV). With the advent of high-resolution CT, more precise volumetric deformation fields have been computed over the respiratory cycle. In a study by Margeras *et al.* displacement of tumors was > 1 cm in three of nine patients [87]. Deformable registration schemes have further been implemented to characterize local lung mechanics throughout the entire lung. Results from Coselman *et al.* computed a mean displacement of 0.4 mm in x , 8.1 mm in y , and 3.2 in z directions of all points in the lung [18]. Fan *et al.* computed values of 6.73 mm in x , 17.69 mm in y , and 0.59 mm in z directions [28]. Boldea *et al.* computed a displacement of approximately 3 to 4 mm for two patients [8]. Tawhai *et al.* computed regional volume changes over the entire lung,

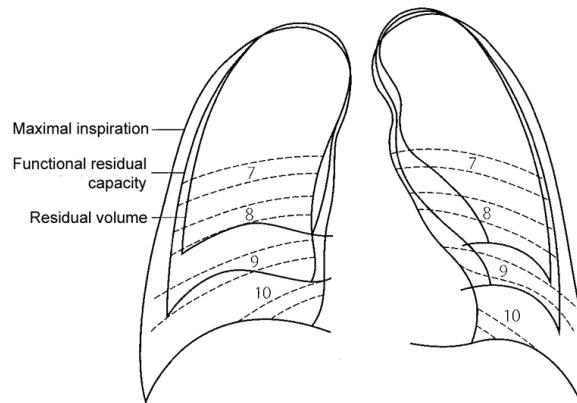


Figure 6.2: Radiographic outlines of a lung at various volumes from [86]. The outer outline represents the lung shape at maximal inspiration, the middle outline represents the FRC volume, and the inner outline is at RV. The lower ribs are numbered corresponding to their position at maximal inspiration.

showing that volume change was significant in the lower lung adjacent to the diaphragm and appeared highly non-uniform [146].

The result from previous work substantiate concerns over the effect of respiration misalignment between a static preoperative CT and that of a live, dynamically breathing, subject. However, results seem inconclusive over the magnitude of the motion as well as its ability to be modeled. To clarify the effect of respiration in pig studies, a non-rigid registration framework was developed to directly quantify deformation caused by breathing. A determination of the registration consistency is also made and a simple motion model is proposed for motion compensation during tracked bronchoscopy.

6.2 Non-rigid Registration

Non-rigid registration of 3D images establishes point correspondences between every voxel in a pair of images. Warping of a test image (also termed a moving image) proceeds until its similarity to a reference (or fixed) image is maximized. Similarity metrics are most frequently derived from voxel-to-voxel grayscale comparison of the registered image to the

fixed image. The warping of the moving image is described by a deformation field, defining at every point, a three-dimensional displacement vector that points to the corresponding location in the fixed image. Within an organ such as the lung, non-rigid registration of serial CT images has helped elucidate structure-function relationships. Literature has shown non-rigid registration of CT lung images to be a useful tool in quantifying regional ventilation [28, 107, 43], modeling lung biomechanics [140], measuring deformation of the thorax [161, 18, 153], and real-time CT-fluoroscopic guidance of a biopsy needle [126, 168, 152]. For this experiment, non-rigid registration provides a quantitative measure of the deformation at each point in the lung between two phases of respiration. This can then be used to correct for deformation of the lung at the recorded SFE tip position within a breathing animal.

Non-rigid registration of lung images has been explored using a number of methods, including: optical flow [24], surface matching [153], and hybrid landmark and intensity based techniques [68]. The algorithm choice is often highly dependent on the application. When registering inter-subject data sets, image discrepancies owing to anatomical variation between patients, scanner types, and image resolutions require more robust registration methods. In these cases, direct comparison of grayscale values is insufficient, and thus manual, automatic, or semi-automatic identification of corresponding landmarks is required. Because registration is only performed on images acquired from the same subject in this experiment, consistency in anatomical topology and image reconstruction has motivated the use of an intensity-based registration method. In this scheme gray-level similarity of intra-subject images is optimized without constraining correspondence of predefined landmarks or surface points.

6.2.1 *Optical Flow and the Demons Algorithm*

An optical flow-based registration method known as the ‘demons’ algorithm, proposed by Thirion [148], was implemented for characterizing deformation between chest images of a pig taken at various lung capacities. The demons algorithm has demonstrated performance

comparable with other methods [165, 109] and has been used by previous studies to register lung images [8, 155, 168, 6].

For a fixed image F , and moving image G , the 3D images $F(x,y,z)$ and $G(x,y,z)$ are considered as discrete samples of a 4D (time-varying) image $I(x,y,z,t)$. Each point in I is considered to have a constant intensity κ and underlying time-dependent position $\langle x(t), y(t), z(t) \rangle$, such that $I(x(t), y(t), z(t), t) = \kappa$. If F and G are ‘‘snapshots’’ of I at times t_0 and t_1 respectively, then the correspondence between F and G at any point (x, y, z) is measured by the velocity vector \mathbf{v} , where:

$$\mathbf{v} = \frac{\langle x(t_1) - x(t_0), y(t_1) - y(t_0), z(t_1) - z(t_0) \rangle}{t_1 - t_0}$$

Considering the change in time, $t_1 - t_0$, to be unity, \mathbf{v} represents the displacement of any point, $\mathbf{x} = (x, y, z)$ in image G to a point $\mathbf{x} + \mathbf{v}$ in image F . From optical flow equations, the displacement is estimated using the local gradient $\vec{\nabla}F$ such that $\mathbf{v} \cdot \vec{\nabla}F = G - F$ (Figure 6.3). The displacement estimate is rewritten as:

$$\mathbf{v} = \frac{(G - F)\vec{\nabla}F}{\vec{\nabla}F^2} \quad (6.1)$$

However, the estimates of \mathbf{v} become extremely largely in regions where $\vec{\nabla}F$ approaches zero. Therefore, an additional $(G - F)^2$ term is added to the denominator of equation 6.1 to prevent infinite displacement values:

$$\mathbf{v} = \frac{(G - F)\vec{\nabla}F}{\|\vec{\nabla}F\|^2 + (G - F)^2}. \quad (6.2)$$

Given the optical flow equation of 6.2, we seek a general transformation U that warps the moving image G into fixed image F , given by $F = U \cdot G$. More specifically, this transformation is given by a 3D vector field \vec{U} , defining at each point \mathbf{x} , the correspondence between F and G , such that $F(\mathbf{x}) = G(\mathbf{x} + \vec{U}(\mathbf{x}))$. Using the demons algorithm, the deformation field

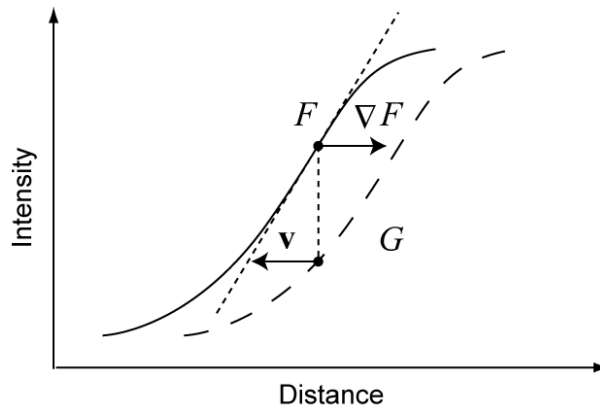


Figure 6.3: A 1D example illustrating the optical flow between a fixed image F and moving image G . The displacement vector \mathbf{v} computes the displacement of a point in G that is proportional to the grayscale difference $G - F$.

\vec{U} is resolved through an iterative two-step approach. In the first step, the deformation field, given by \vec{U} , is updated from equation 6.2 for each voxel where $\mathbf{v} = \vec{U}(\mathbf{x}) \forall \mathbf{x} \in G$. Following, regularization of the deformation field is performed to maintain a locally smooth deformation. With each iteration of the algorithm, the moving image G diffuses into F until the grayscale intensity differences are small, producing negligible displacement forces. In the iterative approach, equation 6.2 is rewritten with respect to the deformation field \vec{U} , giving:

$$\vec{U}_{i+1}(\mathbf{x}) = \vec{U}_i(\mathbf{x}) + \frac{F(\mathbf{x}) - G(\mathbf{x} + \vec{U}_i(\mathbf{x}))}{\|\vec{\nabla}F(\mathbf{x})\|^2 + \alpha^2[F(\mathbf{x}) - G(\mathbf{x} + \vec{U}_i(\mathbf{x}))]^2} \vec{\nabla}F(\mathbf{x}). \quad (6.3)$$

In equation 6.3 the updated deformation \vec{U}_{i+1} is computed from the previous deformation, \vec{U}_i , and the warped moving image, $U_i \cdot G$, whose grayscale intensity is given at each point \mathbf{x} by $G(\mathbf{x} + \vec{U}_i(\mathbf{x}))$. The α^2 term is provided as a step parameter which dictates the convergence speed of the algorithm. Following the update from equation 6.3, \vec{U} is regularized by Gaussian smoothing in each dimension.

6.3 Experimental Methods

6.3.1 Image Acquisition

CT imaging was performed as described in section 3.1.2.1. Images were reconstructed at slightly different resolutions and slice thicknesses, though they were all between 0.50 and 0.80 mm. For each subject at least 10 chest CT scans were acquired at various static lung pressures. During each scan, the subject was placed on a continuous positive airway pressure system to hold the lung at a fixed pressure. The scans were performed in sets of 5 scans. Within the set, scans were performed at the equally spaced lung pressures of 6, 10, 14, 18, and 22 cmH₂O, denoted hereafter as *A*, *B*, *C*, *D*, and *E* scans respectively. For the first series, scans were performed in descending order ($E_1 - A_1$), while the second series was performed in increasing ($A_2 - E_2$) order. Radio-opaque fiducial markers were also placed on the chest and abdomen to correct for small shifts in the subjects position.

6.3.2 Deformable Registration Framework

The deformable demons registration framework is diagrammed in Figure 6.4. Registration software was adapted from code found within the Insight Toolkit (ITK), and implemented within MATLAB. The two stages of the registration are initial preprocessing and non-rigid registration using multi-resolution demons.

6.3.2.1 Preprocessing

Before registering a fixed image *F* and moving image *G*, preprocessing of the original fixed and moving CT images is necessary (Figure 6.4). This stage involves: 1) rigid registration; 2) lung segmentation; 3) histogram matching; and 4) image smoothing. Rigid registration of the moving image to the fixed image corrects for shifting in the subject's position or orientation so as to eliminate non-respiratory-induced motion. Fiducial markers placed on the pig's breast plate and shoulders were used to measure rigid motion as they did not deform with breathing.

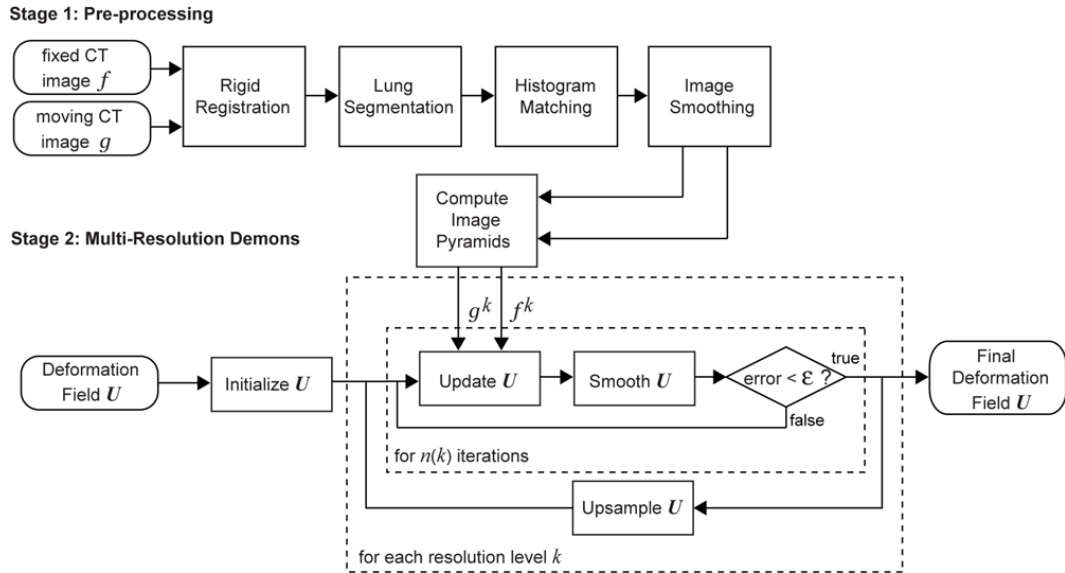


Figure 6.4: The deformable demons registration framework

In the second step, segmentation of the lung permits removal of unnecessary image data from the registration process. A stipulation of the deformation field \vec{U} requires that motion be locally smooth without discontinuities. The pleural surface, however, is a sliding boundary that can move independently from the ribcage and chest wall. Therefore the lung is initially segmented using previously developed methods [62] to nullify the effects of motion of chest wall and cardiac image regions.

The third phase of preprocessing applies a histogram matching filter that aligns the intensity histograms of both the fixed and moving images following lung segmentation. Although registered images are all obtained from the same subject, intensity-based registration does not account for the gray-level shifts that occur during expansion or contraction of the lung. At full inspiration the lung parenchyma appears very dark due to a high fractional air volume. At full expiration, however, lung compression results in an overall increase in density and brightening of the lung parenchyma while other pulmonary structures are left unchanged. The histogram matching filter is used to compensate for this effect. As part of

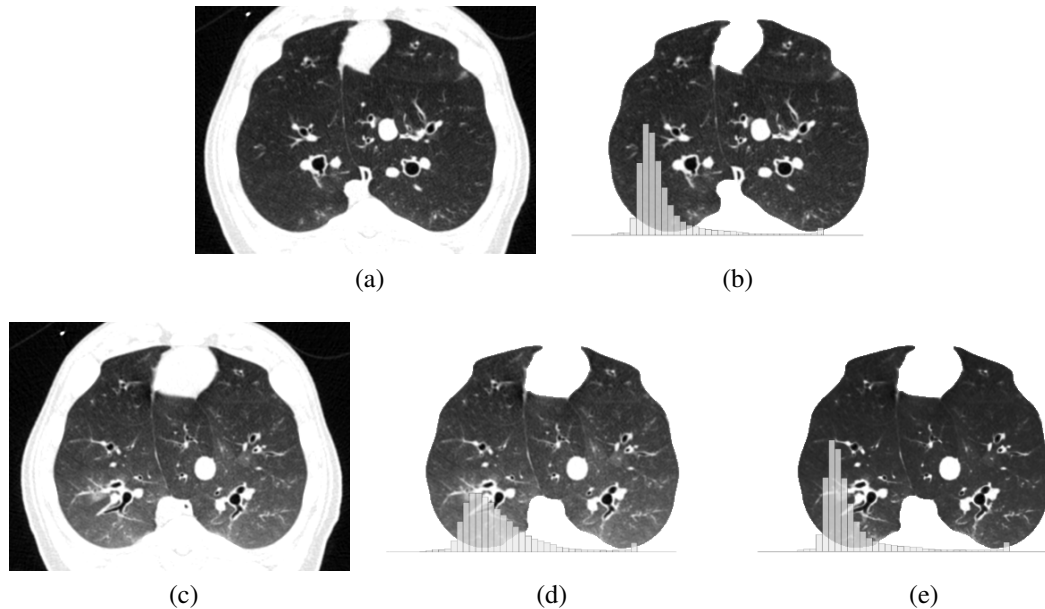


Figure 6.5: Preprocessing of the fixed and moving images prior to deformable registration. During the preprocessing stage, a moving image (c) is first rigidly registered to the fixed image (a). In the second step, the lung region is segmented from the rest of the anatomy (b&d). In the third step, the histogram matching filter adjusts the moving image grayscale histogram to match the fixed image histogram (e). In this example, the interstitial space of the moving image is brighter due to compression of lung tissue at FRC. Following histogram matching, the graylevel histogram shifts leftward to match the darker fixed image histogram taken at TLC.

the study, registration results were compared both with and without use of this filter.

Finally, both the fixed and moving images are smoothed using a Gaussian smoothing kernel to reduce image noise. By smoothing the images, the gradient ∇F can be easily computed using the central difference estimate. Were image noise not removed, the image gradients would be highly spurious, causing inaccurate registration.

6.3.2.2 Multi-Resolution Demons

Following the preprocessing stage, image resolution pyramids are generated for both input images F and G . At each pyramid level k , the image resolution of the previous level is downsampled by 2 in all dimensions to construct lower-resolution images F^k and G^k , such

that F^0 and G^0 are the original images and F^m and G^m have been downsampled m times. The registration starts at the lowest resolution ($k = m$) and decrements through m levels to the full resolution image ($k = 0$). Registration of images in this hierarchical fashion is advantageous in that large deformations are more accurately and expediently recovered when progressively refined in a coarse to fine manner. For this study, resolution pyramids of 6 levels ($m = 5$) were constructed and the number of iterations for each resolution, $n(k)$, was set to 4^{k+1} empirically.

6.3.3 Experimental Variants

Four variants of the algorithm were tested and optimized based on the quality of the registration. These included:

1. Histogram matching
2. Symmetric demons forces
3. Field smoothing standard deviation
4. Adaptive smoothing method

First, the use of a histogram matching filter in the pre-processing phase was validated by comparing registrations that resulted both with and without histogram matching. Second, the demons force from equation 6.3 was modified to be symmetrical. In this adaptation the symmetric force was computed by averaging the fixed image gradient $\vec{\nabla}F(x)$ and the gradient of the registered image $\vec{\nabla}G(x + \vec{U}_i(x))$ at the current iteration [147]. This symmetric image gradient that combines both the forward and backward registration forces is defined as:

$$\vec{\nabla}S(x) = \frac{\vec{\nabla}F(x) + \vec{\nabla}G(x + \vec{U}_i(x))}{2}$$

The symmetric force gradient $\vec{\nabla}S(x)$ is exchanged for $\vec{\nabla}F(x)$ in equation 6.3 to yield a symmetric update in equation 6.4.

$$\vec{U}_{i+1}(x) = \vec{U}_i(x) + \frac{F(x) - G(x + \vec{U}_i(x))}{\|\vec{\nabla}S(x)\|^2 + \alpha^2[F(x) - G(x + \vec{U}_i(x))]^2} \vec{\nabla}S(x) \quad (6.4)$$

The velocity or displacement computed at each voxel tends to be more accurate and better preserves invertibility of the deformation. Third, the standard deviation σ of the Gaussian smoothing kernel g is tuned in order to find an optimum degree of smoothing. Under-smoothing of \vec{U} can lead to noisy motion predictions that are spurious and inaccurate. Over-smoothing, worsens registration resolution and causes insensitivity to local variations in the deformation. Lastly, an adaptive smoothing technique was used as a modification to regularization by Gaussian smoothing. During adaptive smoothing, each element of the Gaussian smoothing kernel g is additionally weighted by the local magnitude of the fixed image gradient. Using this approach, smoothing of the deformation field preferentially weights voxels that lie on surface contours or sharp boundaries where motion estimations are likely to be more accurate. The adaptive smoothing method at each point \mathbf{x} is given by:

$$\vec{U}(\mathbf{x})_{smooth} = \frac{\sum_{t=-a}^a g(t) \cdot \|\vec{\nabla}F(\mathbf{x}+t)\| \cdot \vec{U}(\mathbf{x}+t)}{\sum_{t=-a}^a g(t) \cdot \|\vec{\nabla}F(\mathbf{x}+t)\|}$$

where a is the size of the Gaussian smoothing kernel g .

6.4 Results

6.4.1 Registration Parameter Optimization

No gold standard exists by which to measure registration accuracy. Here, registration results are compared using inverse and transitive consistency metrics [14]. First, U_{FG} is defined as the transformation that maps a point \mathbf{x} in image G to a point $U_{FG}(\mathbf{x})$ in image F . The inverse consistency stipulates that U_{FG} should be equal to the inverse of U_{GF} such that $U_{FG}(\mathbf{x}) = U_{GF}^{-1}(\mathbf{x})$ and $U_{GF} \cdot U_{FG}(\mathbf{x}) = \mathbf{I}$, where \mathbf{I} is the identity matrix. This relationship is not a mathematical certainty as registration of G to F is independent from that computed for F to G . Thus the inverse error at a point \mathbf{x} , is measured as the Euclidean distance be-

tween x and $U_{GF} \cdot U_{FG}(x)$ (equation 6.5). The inverse consistency error, E^{IC} , in registering image G to F is calculated as the mean of errors from every point $x \in G$.

$$E_{FG}^{IC} = \frac{1}{N} \sum_i^N \|x_i - U_{GF} \cdot U_{FG}(x_i)\| \quad (6.5)$$

$$E_{FGH}^{TC} = \frac{1}{N} \sum_i^N \|U_{FH}(x_i) - U_{FG} \cdot U_{GH}(x_i)\| \quad (6.6)$$

The transitive consistency restraint further asserts that each deformation should be equivalent to a series of transformations that begin and end with the same images. Thus a transformation $U_{FH}(x)$ should be equivalent to a transformation series $U_{FG} \cdot U_{GH}(x)$ that maps a point x in image H first to an intermediate image G , and then from G to F . Transitive consistency error for the image triplet F , G , and H is measured as the Euclidean distance between $U_{FH}(x)$ and $U_{FG} \cdot U_{GH}(x)$ (equation 6.6).

To avoid excessive computation, algorithm performance assessment was limited to registrations of only the five images in the first series of scans ($A_1 - E_1$). This yielded a total of 20 individual image pair registrations from which to analyze. Thus for each change made to the registration parameter settings, E^{IC} was computed for 20 image pairs, and E^{TC} was computed for 20 image triplets.

Histogram Matching: The histogram matching filter takes as its inputs, a test image and reference image to which the test image's histogram is matched. The matching algorithm generally seeks a function f that converts a graylevel x in the moving image to a value $f(x)$ in the fixed image such that:

$$\int_0^x p_g(x) dx = \int_0^{f(x)} p_f(f(x)) dx$$

where $p_g(x)$ and $p_f(x)$ represents the probability of the graylevel x occurring in the moving and fixed images, respectively. For a discrete grayscale image, f can be expressed

as a monotonically increasing vector that maps each input graylevel x to an output $f(x)$. Initially, E^{IC} and E^{TC} are computed without histogram matching. Averaging over all 20 registrations, the errors were 1.292 mm and 1.349 mm respectively. After implementing the histogram matching filter, registration error dropped to 0.502 mm and 0.712 mm respectively (Figure 6.6).

Symmetric Demons Forces: The symmetric demons algorithm also improved registration performance. Mean inverse and transitive registration errors dropped from 0.502 mm to 0.409 mm and from 0.712 mm to 0.678 mm respectively when the symmetric correction is applied (Figure 6.6). The symmetric forces variant of the demons algorithm was used for all subsequent experiments as it constituted a modes improvement in registration accuracy as well as a more expedient registration convergence.

Gaussian Smoothing: The impact of Gaussian smoothing was experimentally tested over a range of standard deviations, σ , at integral values from 1.0 to 7.0 voxels. Registration error was largest at a value of 1, and sharply declined at higher values of σ . Interestingly enough, as σ increases, E^{IC} levels off, while E^{TC} increases at values larger than 4 (Figure 6.7). Because of the use of symmetric demons forces, over-smoothing may not affect inverse registration error to the same degree. It is concluded that selection of $\sigma > 4$ causes over-smoothing of the deformation field, and σ was therefore set to 4 for the remainder of the parameter-tuning process. Following this adjustment, E^{IC} and E^{TC} fell to 0.252 mm and 0.555 mm respectively.

Adaptive Gradient-Weighted Smoothing: Lastly, the adaptive smoothing technique demonstrated a modest improvement in registration accuracy. While E^{IC} increased slightly to 0.291 mm, E^{TC} decreased from 0.555 mm to 0.398 mm.

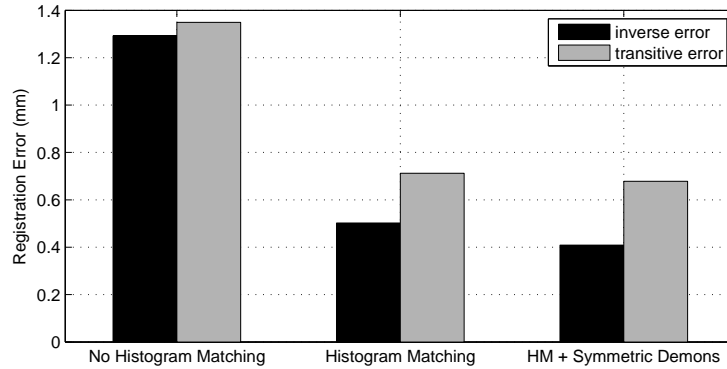


Figure 6.6: Inverse and transitive registration errors with and without histogram matching and symmetric demons forces. Implementation of the histogram filter into the pre-processing stage dramatically reduces registration errors. Additionally, the symmetric demons forces further improve registration accuracy.

6.4.2 Measuring Deformation

After establishing an optimum set of algorithm parameters, image E_1 was selected as a baseline image, and was registered to every other image. This produced a total of 14 deformation fields, denoted by the variable \vec{U}_X , which describe the deformation from image E_1 to image X . The maximum deformation was observed between the baseline image at full inspiration and A_1 at full expiration, giving \vec{U}_{A_1} or \vec{U}_{max} . The deformation field \vec{U}_{max} possesses a mean displacement magnitude of 11.11 ± 4.89 mm. The mean directional motion is 0.53 ± 2.73 mm in the x -axis, 4.71 ± 3.21 mm in the y -axis, and -8.53 ± 5.86 mm in the z -axis. This motion is as expected. As seen by Figure 6.9, deformation is much larger in the lower lung sections where contraction of the diaphragm deforms the lungs primarily along the z -axis. By contrast, regions of the upper lung undergo very little deformation. Expansion of the rib cage also results in a mean motion vector out from the chest along the y -axis when the subject is in the supine position. The mean deformation along the x -axis or side to side motion is least significant as it is highly symmetric.

The average lung displacement is shown relative to respiratory pressure in Table 6.1.

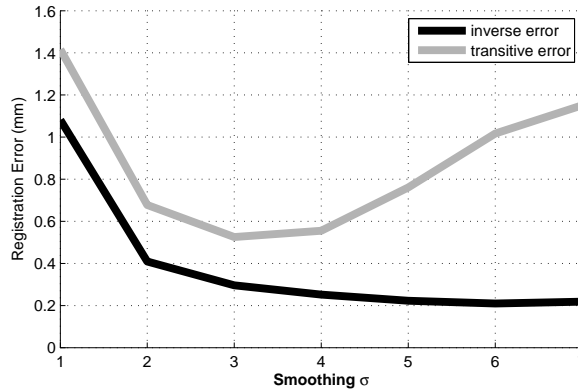


Figure 6.7: Inverse and transitive registration error as a function of the degree of smoothing. Regularization of the deformation field \vec{U} is achieved by Gaussian smoothing. As σ increases, E^{IC} decreases and eventually levels off. E^{TC} is optimized at a σ value between 3 and 4.

The mean motion from E_1 to A_1 is approximately 6-7 times the diameter of the SFE and the smallest accessible airways. In the lower lung, the displacement increases to 20 mm which is 12-13 times the SFE diameter. This presents a significant source of localization error in accurately tracking the SFE during a bronchoscopic procedure, especially within peripheral airways.

Table 6.1: Mean lung displacements (in mm) computed between the baseline CT scan at full inspiration and scans taken over the entire respiratory cycle.

	<i>A</i>	<i>B</i>	<i>C</i>	<i>D</i>	<i>E</i>
series 1	10.28	7.10	4.64	1.39	NA
series 2	11.00	7.38	4.65	2.97	1.08
series 3	10.18	7.47	4.99	2.72	1.80
average	10.47	7.32	4.76	2.36	1.44

6.4.3 Modeling Lung Deformation

To compensate for the localization error caused by breathing, a model of the deformation, $\vec{\Phi}(x, p)$, was constructed to predict displacement of any point x in the baseline image E_1 as a

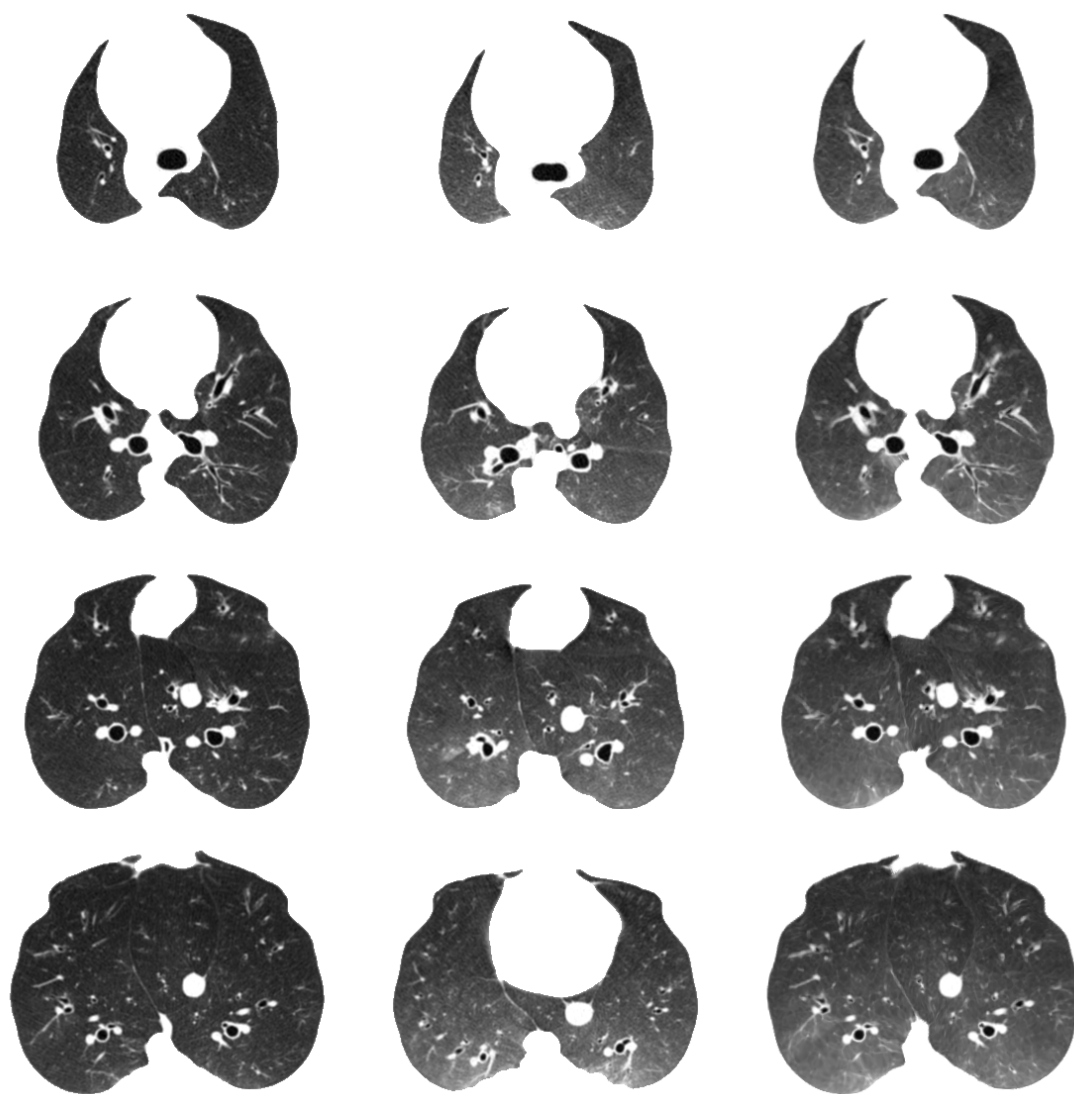


Figure 6.8: Registration result of the fixed and moving images

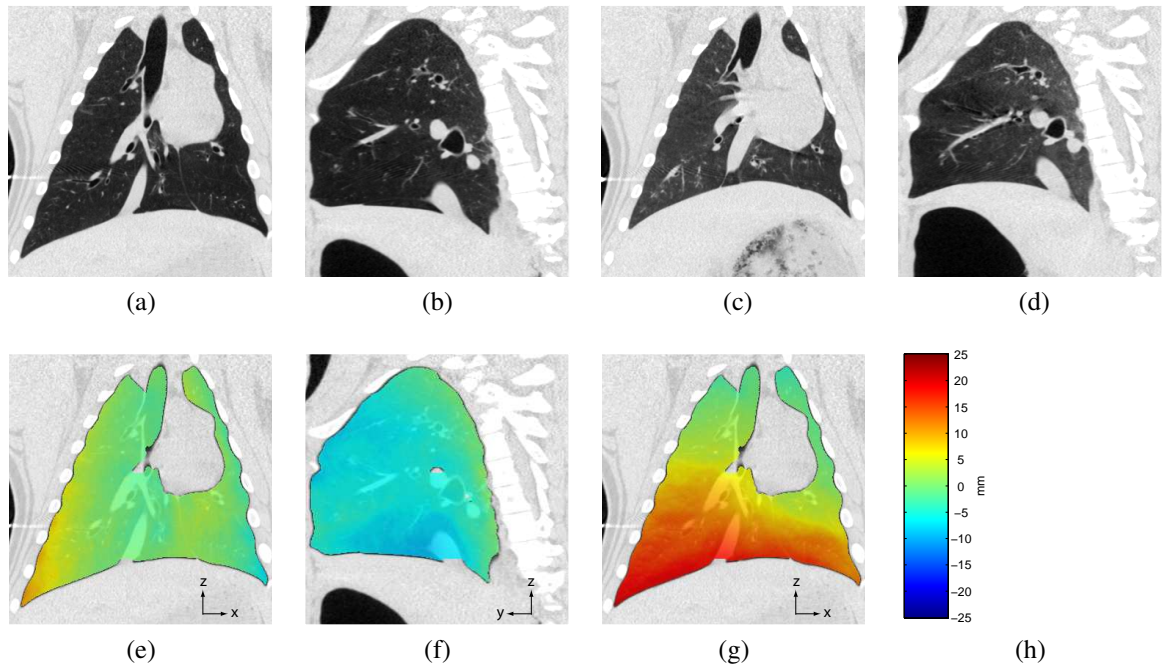


Figure 6.9: The deformation field \vec{U}_{max} is computed from registering image E_1 , represented by coronal and sagittal slices (a) and (b), to image A_1 , represented by slices (c) and (d) at the same position. Color overlays depict the magnitude of the deformation \vec{U}_{max} along the x-(e), y-(f), and z-(g) axes.

function of the distending lung pressure $p(t)$ which is assumed to be an oscillatory function of time. Given that each point in the lung follows some underlying motion $x(p(t))$, each deformation field \vec{U}_X provides an estimation of the displacement $x(p_X) - x(p_0)$, where p_X is the distending pressure corresponding to image X , and p_0 is the baseline pressure, p_{E_1} . The model, $\vec{\Phi}$, can therefore be fit to the deformations in \vec{U}_X . However, while the number of deformation fields computed in this study are sufficient for characterizing complex motion, the model $\vec{\Phi}$ must also consider that repetitive CT scanning of a patient for this purpose is not clinically feasible. Therefore, a linear model of lung deformation was developed as an approximation to the actual motion by assuming that any lung deformation during breathing could be modeled as a submultiple of the maximal deformation given by \vec{U}_{max} , that submultiple applying to all parts of the lung simultaneously. This linear model estimates

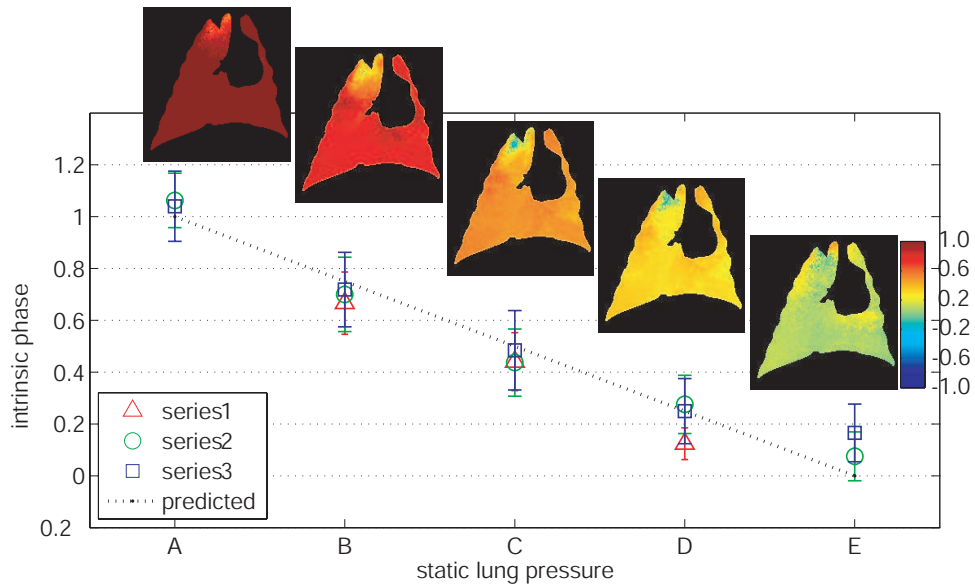


Figure 6.10: The mean value of the intrinsic phase ϕ is computed for each deformation field \vec{U}_X and plotted versus static lung pressure. Sample slices depict the distribution of ϕ at the corresponding pressures.

the deformation of the lung at an arbitrary distending pressure p as a fraction of \vec{U}_{max} :

$$\vec{\Phi}(p) = \phi(p) \cdot \vec{U}_{max}, \quad (6.7)$$

where ϕ is defined as the intrinsic phase. Unlike respiratory phase, which associates a point in the respiratory cycle by time, intrinsic phase ϕ is defined by the fractional deformation of the lung at any moment. For each deformation \vec{U}_X , the intrinsic phase ϕ is estimated at each point as:

$$\phi(x, p_X) = \frac{\vec{U}_X(x) \cdot \vec{U}_{max}(x)}{\|\vec{U}_{max}(x)\|^2} \quad (6.8)$$

Equation 6.8 calculates ϕ as the magnitude of the fractional displacement at $\vec{U}_X(x)$ that is collinear with $\vec{U}_{max}(x)$. For the linear model to be valid, $\phi(x, p)$ should be relatively constant for all points in a given deformation \vec{U}_X .

The mean and standard deviation of ϕ was computed over the entire lung for each

deformation field \vec{U}_X and plotted versus static lung pressure (Figure 6.11). The standard deviation of ϕ is 0.117 on average. Coronal image slices illustrate the spatial distribution of ϕ , for each image in series 2. For each slice, ϕ appears fairly constant, with the exception of a couple of small regions. These areas, however, correspond to regions of the lung in which motion is nearly non-existent. As a result, the computed deformations in these regions are highly susceptible to noise from the registration process. Because the motion of these regions is small, the resulting localization error is minimal and of little consequence. When considering only those points in the lung which deform a distance of 5 mm or more over the respiratory cycle, the mean standard deviation of ϕ drops to 0.079. Overall, results indicate that data are consistent with the model. For each image, $\phi(p_X)$ from equation 6.7 is computed as the mean value of $\phi(x, p_X)$ averaged over the entire lung.

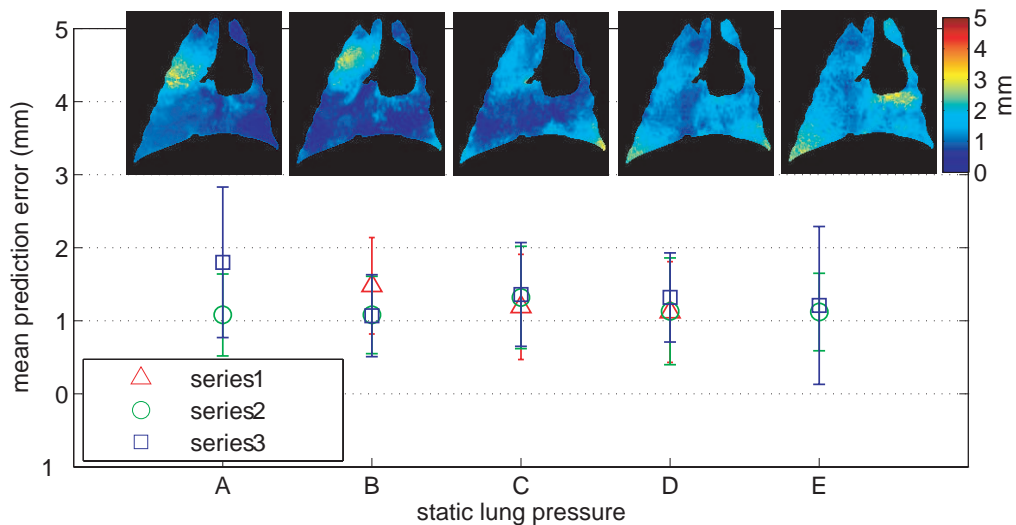


Figure 6.11: The mean MPE is plotted for each deformation \vec{U}_ϕ . Sample slices of the MPE are depicted for deformation fields for images in series 2. Overall, prediction errors are low (<2 mm predominantly)

Although the data validates modeling each deformation as a submultiple of \vec{U}_{max} , no assumptions have yet been made as to how ϕ varies with lung pressure. From Figure 6.11,

it appears that the relationship between ϕ and static lung pressure is linear. The intrinsic phase can therefore be computed as:

$$\phi(p) = \frac{p - p_0}{p_{max} - p_0}. \quad (6.9)$$

For each A , B , C , D , or E image, the corresponding value of ϕ is 1.0, 0.75, 0.50, 0.25, and 0.0 respectively.

At this stage, Φ is completely described. The accuracy of this model was then tested by comparing each deformation field \vec{U}_X to the predicted model, $\Phi(p_X)$. A formal definition of the model prediction error (MPE) is given below.

$$\text{MPE} = \frac{1}{N} \sum_x^N \|\vec{U}_X(x) - \vec{\Phi}(x, \phi(p_X))\| \quad (6.10)$$

Table 6.2 gives the lung-averaged MPE values for each deformation field. The MPE values range from 1.08 mm to 1.80 mm. The model prediction is also illustrated in Figure 6.12. The segmented airway surface from image E_1 (*red*) is warped to match the airway surface from image C_1 (*green*) using the computed deformation \vec{U}_{C_1} . This is compared to deformation predicted by $\Phi(\phi = 0.5)$ (*blue*).

Table 6.2: Prediction error (in mm) of the linear lung motion model for each CT scan acquired.

MPE (mm) (σ)	A	B	C	D	E
series 1	NA	1.48 (0.66)	1.19 (0.72)	1.12 (0.69)	NA
series 2	1.08 (0.56)	1.08 (0.53)	1.32 (0.70)	1.13 (0.73)	1.12 (0.53)
series 3	1.80 (1.03)	1.07 (0.56)	1.36 (0.71)	1.32 (0.61)	1.21 (1.08)
Average	1.44 (0.80)	1.21 (0.59)	1.29 (0.71)	1.19 (0.68)	1.17 (0.81)

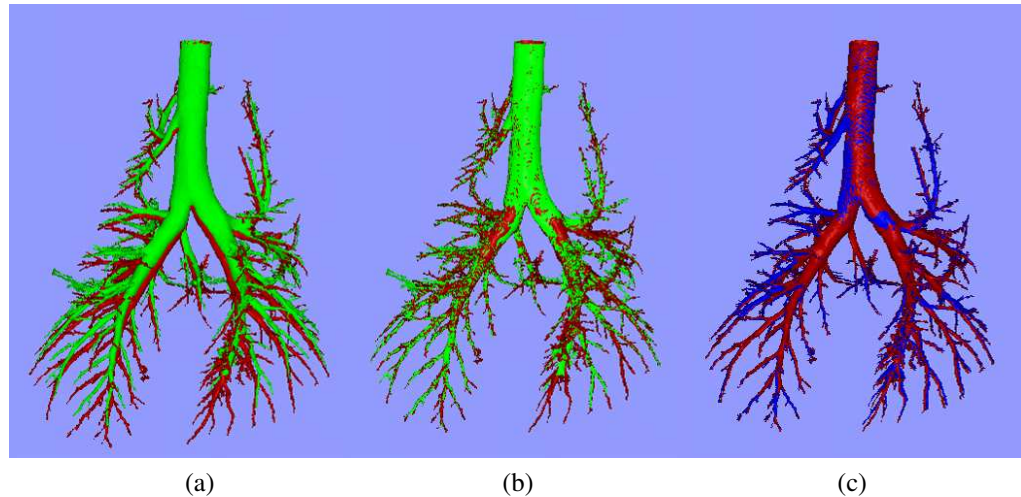


Figure 6.12: Surface renderings of the airways compare the predicted and computed deformations at an intermediate respiratory phase. Surface renderings of the segmented airways from image E_1 (red) and image C_1 (green) are depicted (a). The airway surface from E_1 is warped to match the surface from C_1 using the deformation field \vec{U}_{C_1} (b). The warped surface is then compared to the predicted surface (blue) using the model $\vec{\Phi}$ (c).

6.5 Discussion

The proposed linear model of lung deformation appears to be a good approximation of the actual motion that is undergone by the lung during respiration as computed by the registration algorithm. Specific to our definition of linearity, each deformation can be adequately approximated as a submultiple of the maximum deformation, and the magnitude of this deformation increases linearly with distending lung pressure. Using this model, it is possible to compensate for deformation using only two CT scans at inspiratory and expiratory phases of respiration. Overall, model prediction error is on the order of 1.07-1.80 mm for each image collected. In the case of the maximum deformations between E and A images, the mean displacement was 10.47 mm, which was recovered to within 1.44 mm. This constitutes an 87% reduction respiration-induced localization error. Although the data on average follows the linear prediction on Figure 6.11, some of the images, such as D_1 and E_3 fit less well. It is possible that there were fluctuations in pressure that could not be mon-

itored as it was necessary to clear the CT room during scanning. Discrepancies may also be owing to repeated breath holding. For each image, the computed intrinsic phase appears to be slightly higher for series 2 and 3, than for series 1, suggesting that the lung may have become more compliant over time.

Although the accuracy of the model is promising, a number of potential limitations must be considered when compensating for motion in an animal during continuous respiration. First, it is noted, that a subject that is breathing freely is not likely to breath between the same extremes established by the static lung pressures in this study. A more reasonable estimate of end-inspiratory pressure might be 14-18 cmH₂O (*C* and *D* images, respectively). From the values in Table 6.1, the maximum deformation may be closer to 5-7 mm. Conversely, the lowest pressure setting of 6 cmH₂O is slightly higher than the end-expiratory pressure in a breathing subject. This was done to minimize physiological stress on the pig due to the number and duration of breath holds that were required. The magnitude of deformation is undoubtedly also dependent on a number of other factors, including the tidal volume, and parameters specific to the subject.

The model is also limiting in that it is not possible to continuously monitor lung pressure during bronchoscopy. Instead, a surrogate measure of lung pressure will need to be used. For instance, the displacement of an electromagnetic sensor placed on the subject's abdomen can be used to track the intrinsic phase of respiration ϕ . It is, however, quite possible that this metric is a more accurate determinant of ϕ during continuous respiration. The model constructed here directly relates lung deformation between two phases of respiration at static pressures with deformation within a continuously breathing lung. It is well known, however, that pressure-volume relationships differ in these two scenarios. By measuring intrinsic phase using a mounted sensor, pressure can be decoupled from the model altogether.

Lastly, this model assumes that the lung is quasi-static. It is possible that regions of the lung are viscoelastic, requiring a time-dependent term to adequately model deformation. However, during bronchoscopy we make an assumption that the subject undergoes quiet

breathing to minimize any such effects. Experimental data is still needed to substantiate application of this model to a breathing subject.

Chapter 7

IMAGE-BASED GUIDANCE

Accurate endoscopic navigation relies on precise localization of the endoscope *in-vivo* relative to local anatomy that is continuously deforming. External position sensing methods such as EMT are capable of intraoperative localization, but suffer from inherent registration error and misalignment due to breathing. This produces a disconnect between the tracked position projected onto the virtual airway model and the bronchoscopic video that cannot be resolved.

Image-based guidance, by contrast utilizes similarity between the real and virtually rendered bronchoscopic images to track a scope through anatomy. Image-based tracking (IBT) is a *closed-loop* localization method that is both highly accurate and adaptive to a deformable environment. The tracking mechanism, termed CT-video registration, reconstructs CT data at various candidate scope positions and orientations searching for a “match” between the video frame and corresponding endoluminal rendering. The benefit of this technique is that it requires no additional hardware and does not suffer from deformation such as those caused by respiration or cardiac motion.

Due to the limitations of EMT experienced in Chapter 5 and the lung motion computed in Chapter 6, IBT using CT-video registration is implemented for SFE video images as an alternative tracking technology. First, a camera calibration and video preprocessing pipeline are developed to synchronize characteristics of both the real and virtual cameras. A number of registration metrics were tested to find the optimal performance for SFE video images during bronchoscopy of a live pig. Again, in designing a system for biopsy of 1 cm nodules, an average localization accuracy of approximately 5 mm is required to ensure

biopsy of a targeted lesion.

7.1 Background

CT-video registration, a specific form of 2D/3D registration, optimizes the position and pose $\tilde{\mathbf{x}} = (x, y, z, \theta, \phi, \gamma)$ of the virtual camera, in CT image coordinates, such that similarity between the 2D video frame I^V and reconstructed virtual image $I_{\tilde{\mathbf{x}}}^V$, from the 3D CT image, is maximized. Figure 7.1 contains a registered virtual and video image, acquired using a conventional bronchoscope. The resulting match is dependent on two specific components of the registration: 1) the optimizer used to refine the position/pose estimate, and 2) the metric used to quantify similarity between virtual and endoscopic images.

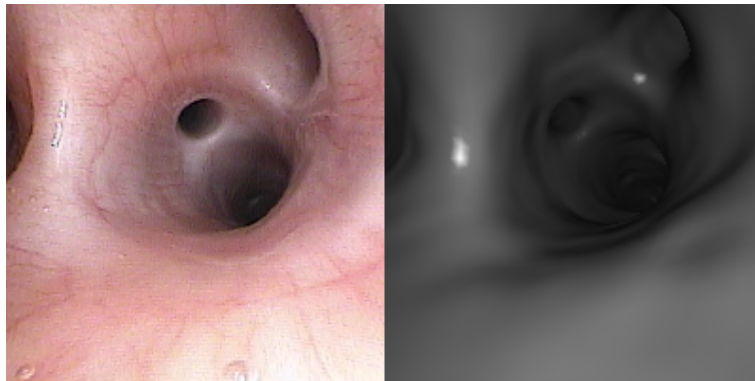


Figure 7.1: Example of CT-video Registration from a conventional PENTAX bronchoscope (EB-1970K).

Similarity metrics for CT-video registration are broken into two classes: 2D-2D and 3D-3D techniques. In the former, similarity is computed from the I^V and the reconstructed image $I_{\tilde{\mathbf{x}}}^{CT}$ as 2D images. Mori *et al.* and Deguchi *et al.* assessed image similarity using a combination of the mean-squared-error and correlation [101, 21]. This metric was then later modified to compute mean-squared-error in selected subregions manifesting characteristic patterns [99]. Similarity has also been computed from mutual information, which measures the joint entropy between real and virtual bronchoscopic images [125, 50, 11].

Helferty *et al.* later adapted this metric to place greater weighting on darker image regions which were less prone to variation in illumination intensity and overexposure [51]. Merritt *et al.* later used cross-correlation between images to evaluate similarity [93]. Alternatively, 3D-3D techniques compute similarity between the 3D scene analysis of the two images. This requires that a 3D surface information be extracted from , and compared to the CT-generated surface mesh. Bricault *et al.* compared 3D structure using shape from shading in video images [9]. Haigron *et al.* computed depth-maps of angioscopic images to reconstruct a 3D scene [47]. Deligianni *et al.* implemented a partial 3D metric by comparing the surface gradients of both the video image and surface mesh model [22].

7.2 Camera Calibration

For CT-video registration to be accurate, a camera calibration procedure must be performed to ensure equivalent homographies between the pixel-spaces of both the virtual and real bronchoscopic images. First, this involves removing radial lens distortion in the video images to reasonably approximate a pinhole camera. Following, the field of view of the video images must be calculated as an input parameter to the virtual rendering. For any camera, a set of intrinsic camera parameters determine the projection of any 2D point on the image plane to a point in the 3D world in camera coordinates, along a given ray. These parameters include the focal length $[f_x, f_y]$, center point $[u, v]$, as well as two non-linear radial distortion coefficients κ_1 and κ_2 . From these, it is possible to relate a 3D world point, $X_w = [x_w, y_w, z_w, 1]^T$, to a pixel position $X_p = [x_p, y_p, 1]^T$ as shown in Figure 7.2a.

First, the position X_w in an arbitrary world coordinate frame must be transformed into a position, $X_c = [x_c, y_c, z_c, 1]^T$, relative to the camera coordinate frame. A transformation T_{wc} defines the extrinsic camera parameters that relate the position and orientation of the camera relative to the world coordinate frame, such that:

$$X_c = T_{wc}X_w \tag{7.1}$$

Here, T_{wc} is given as the 4×4 rigid and homogeneous transformation:

$$T_{wc} = \begin{pmatrix} R & t \\ 0 & 1 \end{pmatrix}$$

where R is a rigid 3×3 rotation matrix, and t is the translation expressed as a 3-element column vector, $[t_x, t_y, t_z]^T$. The point X_c is projected along a ray incident with the camera origin to a point, $X_u = [x_u, y_u, 1]^T$, in normalized coordinates on the image plane of the camera, defined by $z = 1$. By the trigonometric law of similar triangles: $X_u = X_c/z_c$. The acquired frame buffer, however, does not reflect a simple pinhole style camera. In actuality, the lens system introduces radial distortion at each point such that X_u is displaced to X_d by the nonlinear equation:

$$X_u = X_d(1 + \kappa_1 r^2 + \kappa_2 r^4) \quad (7.2)$$

where $r = \sqrt{x_d^2 + y_d^2}$. Finally, the distorted intersection point X_d of ray with the image plane is converted to the pixel-space of the frame buffer:

$$x_p = f_x \cdot x_d + u \quad (7.3)$$

$$y_p = f_y \cdot y_d + v \quad (7.4)$$

as in Figure 7.2b.

A number of methods have been suggested for solving for these intrinsic parameters. The most common approach is to image a test grid of known geometry. The work of Tsai explored general methods of calibration under multiple conditions, specifically depending on the parameters provided by the camera manufacturer[150]. In this work, a method was described for estimating the intrinsic camera parameters using a single calibration image in the event the camera image plane is coplanar with the test target. However, more elaborate calibration procedures have been devised to solve for both intrinsic and extrinsic camera parameters simultaneously[175], by acquiring multiple images of the test target at various

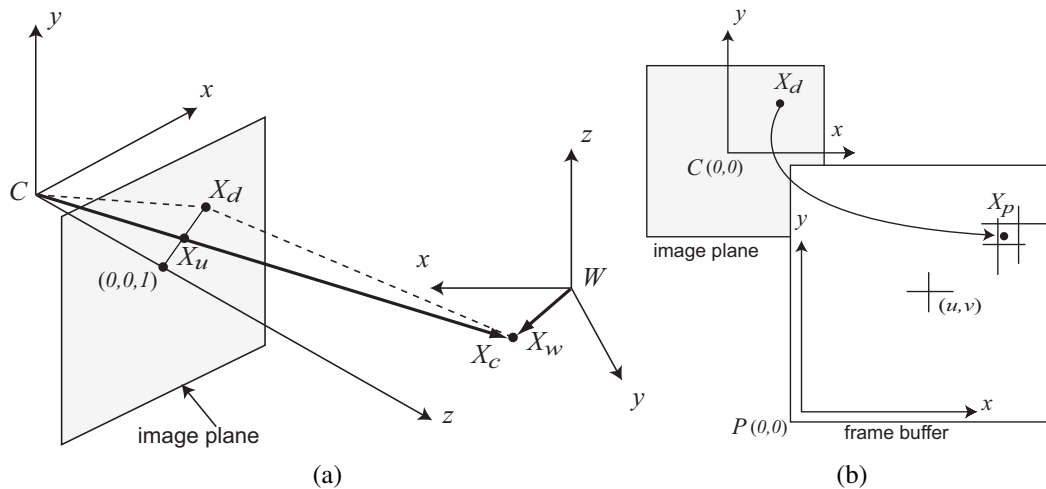


Figure 7.2: A point X_w in world coordinates is projected onto the image plane of a simple pin-hole camera camera at X_u and at the distorted position X_d (a). The point X_d in normalized camera coordinates ($z_c = 1$) is mapped to a pixel position X_p in the frame buffer (b).

viewing locations. Using N images, the 6 intrinsic parameters and $6N$ extrinsic parameters are iteratively refined until converging to an optimal solution.

7.2.1 Methods

For our experiments using the SFE, calibration was performed using OpenCV, a well-known open-source software package for camera calibration (available as a toolbox for MATLAB)¹. As part of this process, a test grid was produced by printing small dots 1 mm in diameter and 5 mm spacing onto a white background (Figure 7.3a). Three central rings define the grid center as well as the x and y axes. To locate the landmarks, bottom-hat filtering of the input image enhances the dark dot regions without sensitivity to variation in illumination (Figure 7.3b). To start, only the central rings are located by adaptively thresholding the filtered image and identifying ring regions based on size and grouping (Figure 7.3c). Once these ring centroids are located, neighbor grid dot locations are iteratively

¹http://www.vision.caltech.edu/bouguetj/calib_doc/

searched in subregions using local estimates of the vectors between rows and columns (Figure 7.3d). The centroid of each dot is located by the maximum point correlation value of each subregion with a Gaussian kernel of similar size. The grid dot detection algorithm ceases once no more dots can be found. From the set of N images, the pixel positions of the grid dots is given by $X_p = [X_p^1, X_p^2, \dots, X_p^N]$, where X_p^i is an array of 3×1 column vectors containing the pixel position, $[x_p, y_p, 1]^T$, of each point. The corresponding grid positions in actual 3D world coordinates are given by X_w for each of the images. The calibration toolbox performs an optimization of all 6 intrinsic camera parameters and $6N$ extrinsic camera parameters, given as homogeneous transformations, $T_{wc}^1, T_{wc}^2, \dots, T_{wc}^N$. From the intrinsic parameters, SFE video images can be undistorted as in Figure 7.3f.

7.2.2 Results

The SFE was maneuvered around the test grid to several perspectives (free-hand) while recording video. For a total of 20 video frames, grid dots were detected and all intrinsic and extrinsic camera parameters were estimated. Table 7.1 presents the estimates of the intrinsic parameters and their approximate error values. The same process was performed for the EB-1970K PENTAX bronchoscope and is also presented. An ideal video frame will have an aspect ratio (f_y/f_x) equal to 1. For a truly centered lens system, the image center should also be roughly near the actual image center. Compared to the conventional bronchoscope, the SFE exhibits considerably larger errors. The aspect ratio is approximately 0.979, though there is an uncertainty of 13 mm. The center pixel is somewhat displaced from the true image center (250,250), and the average pixel error between the detected grid dot locations and the best fit projected locations is 2.82 and 3.54 pixels in the x and y axes. By comparison, the modeled homography for the conventional bronchoscope is much more accurate than for the SFE. However, whereas a conventional bronchoscope's image homography is dependent only on the CCD and lensing, construction of SFE depends completely on the mechanical actuation of the scanning fiber. Distortions can therefore be introduced by inaccuracies in the scan path, small changes in temperature, or asymmetry in the fiber's

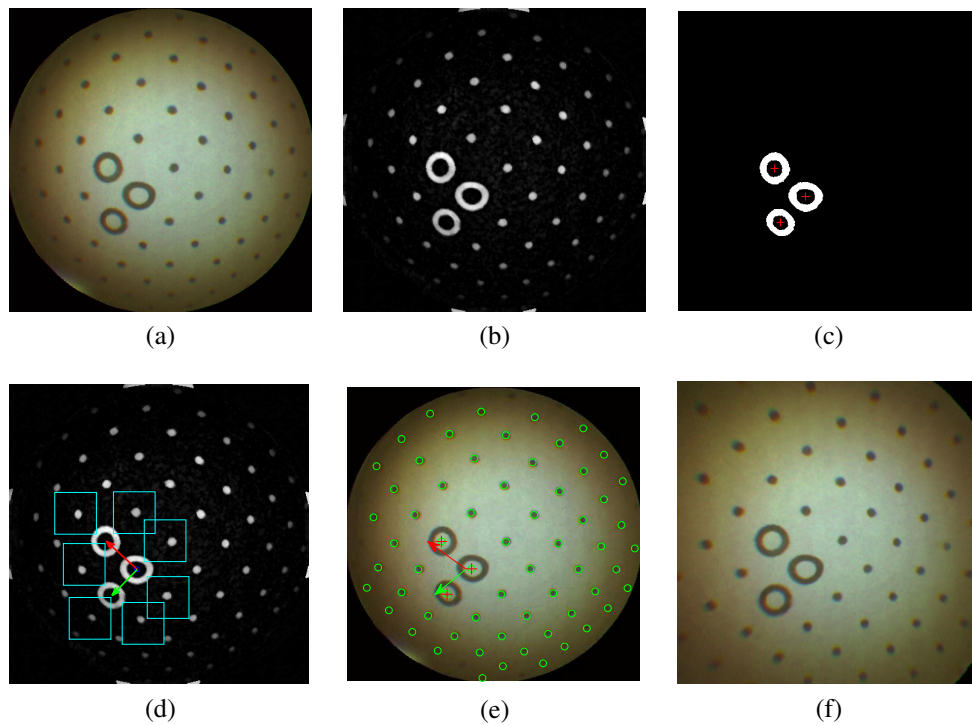


Figure 7.3: Landmark detection and distortion correction of an SFE calibration frame. An input frame (a) is captured while imaging a test target from multiple perspectives. Bottom-hat filtering of the image accentuates dot landmarks in the image (b). The central ring components are identified through adaptive thresholding (c). Grid dots centroids are added by recursively searching neighboring subregions (d), until all visible grid dots have been located (e). Finally, following computation of the intrinsic parameters, the image can be undistorted (f).

Table 7.1: Intrinsic camera parameters of the SFE and EB-1970K bronchoscope computed from multiperspective video images of a test target. The estimates and their error values were calculated from OpenCV, a free open-source software package for camera calibration.

	f_x, f_y	u, v	κ_1, κ_2	pixel error
SFE	421.4±13.67	286.57 ±3.83	-0.522±0.0427	2.82
	412.1±13.01	240.11±3.56	0.213±0.0477	3.54
EB-1970K	407.6±1.27	305.06±0.65	-0.375±0.0025	1.04
	407.9±1.24	243.57±0.63	0.088±0.0013	0.91

vibrational response. Overall, the pixel errors, though larger than that of the EB-1970K, are not significant, and imply that the calibration technique is sufficient for distortion correction of SFE video frames.

7.3 Video Preprocessing

Prior to CT-video registration, preprocessing of each video frame, is necessary. Four main steps are included in the preprocessing and are illustrated, in sequence, in Figure 7.5. These include:

1. distortion correction
2. grayscale conversion
3. vignetting compensation
4. Gaussian smoothing

In the initial distortion correction step (Figure 7.5b), the parameters κ_1 and κ_2 are used to transform undistorted pixel coordinates, to distorted pixel coordinates by equation 7.2. These terms are first and second order radial distortion parameters that specify the barrel distortion present in the image. The undistorted image is then constructed using bilinear interpolation of I^V at the distorted pixel coordinates X_d , for each pixel in the image.

Next, color information is discarded by converting the image to grayscale (Figure 7.5c). Typically, grayscale conversion is performed by computing the image luminance, combin-

ing set percentages of the red, green, and blue pixel components. For the SFB, however, it was noted that the contributions from green and blue tended to die off closer to the image fringe. This introduced large inconsistencies in the illumination model. Instead, the red component alone was extracted for grayscale conversion. The benefits of this approach were first, that illumination by the red laser was far more uniform over the entire image, and second, the red channel is far less affected by surface color variations caused by blood vessels or cartilage, and thus better approximates the illumination model for a uniformly reflective surface.

At the third stage, a vignetting compensation filter is applied to the grayscale image to adjust for a decay in illumination intensity with an increasing angle between a given light ray and the optical axis. The traditional model of image irradiance $I(x, y)$ given a point light source coincident with the camera origin and a lambertian surface is given by:

$$I(x, y) = S_0 \rho \frac{X_c \cdot \mathbf{n}}{\|X_c\|^2} \quad (7.5)$$

where S_0 is the light source illumination, ρ is the surface albedo, and \mathbf{n} is the surface gradient at X_c (Figure 7.4). For clarity, we now assume zero image distortion, such that coordinates (x, y) are normalized pixel coordinates in an undistorted image, such that x and y can be substituted for x_d and y_d in equations 7.3 and 7.4, respectively. Vignetting applies an additional irradiance roll-off in the image that is approximated by an addition $\cos(\phi)^\varepsilon$ term:

$$I(x, y) = S_0 \rho \frac{X_c \cdot \mathbf{n}}{\|X_c\|^2} \cos(\phi)^\varepsilon \quad (7.6)$$

where ε is a user-defined exponent specifying the degree of vignetting. For CT-video registration, vignetting was removed from I^V (Figure 7.5d). For the SFE, ε was assigned a value of 2.0 based on empirical measurement of vignetting by head-on imaging a white background.

In the last stage of the algorithm, a Gaussian filter (3.5 pixels) is applied to the image ,

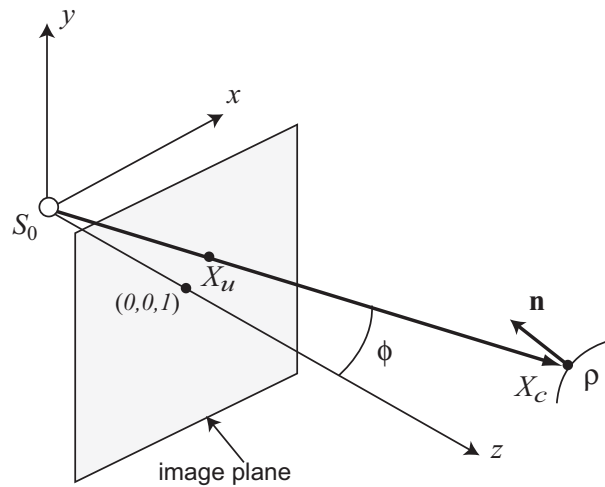


Figure 7.4: Diagram of point light source illumination of a surface point coincident with a pinhole camera

to remove noise.

7.3.1 Frame Rejection

Quite frequently, acquired video images do not contain sufficient information to drive accurate registration between real and virtual bronchoscopic views. Fogging of the lens, blurring caused by mucus, or orienting the scope toward the airway sidewall renders images whose features are not representative of the anatomy being navigated. In such circumstances, continued tracking is best served by foregoing CT-video registration until adequate imaging of the anatomy resumes. Otherwise, CT-video registration may rapidly diverge, making it difficult or impossible to recover the true path of the SFE. Deguchi *et al.* found that the presence of bubbles in video images was concomitant with a noticeable decrease in the correlation between matched real and virtual images [20]. Higgins *et al.* also presented methods to compensate affects of coughing and presence of water in bronchoscopic images [57].

Rejection of SFE video images was found to be crucial for tracking. In particular, video

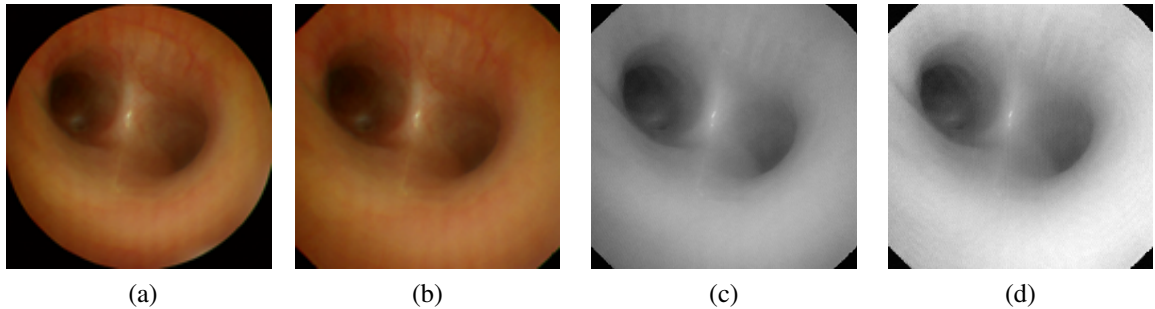


Figure 7.5: Preprocessing stages of the input SFE video image (a) include distortion correction (b), grayscale conversion (c), and vignetting compensation (d).

images tended to suffer from either fouling due to mucus or over-exposure, which results when the SFE view comes in close contact with the airway wall. Figure 7.6 demonstrates images that were insufficient for CT-video registration. In our IBT approach, frame rejection is considered on the basis of the calculated mean local image variance. Local variance is computed at each pixel location from grayvalues within 7×7 neighborhood. Images with a mean local variance of less than 1.9 are rejected.

7.4 Similarity Metrics

Four similarity metrics were tested and validated as a means of optimizing CT-video registration between virtual and bronchoscopic perspectives. The first two metrics used were normalized mutual information (NMI) and a dark-weighted NMI variant (dwNMI) which placed greater emphasis on darker regions of the image. The second two metrics were derived from 3D surface analysis. The first metric measures the surface gradients alignment (SGA) between I^V and $I_{\bar{x}}^{CT}$. Secondly, gradient alignment was further weighted by the in-plane magnitude (mwSGA).

Both NMI and dwNMI are 2D image-based similarity metrics which can be used to drive registration between I^V and the endoluminal perspective image $I_{\bar{x}}^{CT}$ rendered at the corresponding 6D position. For NMI, image similarity is assessed by means of an overlap

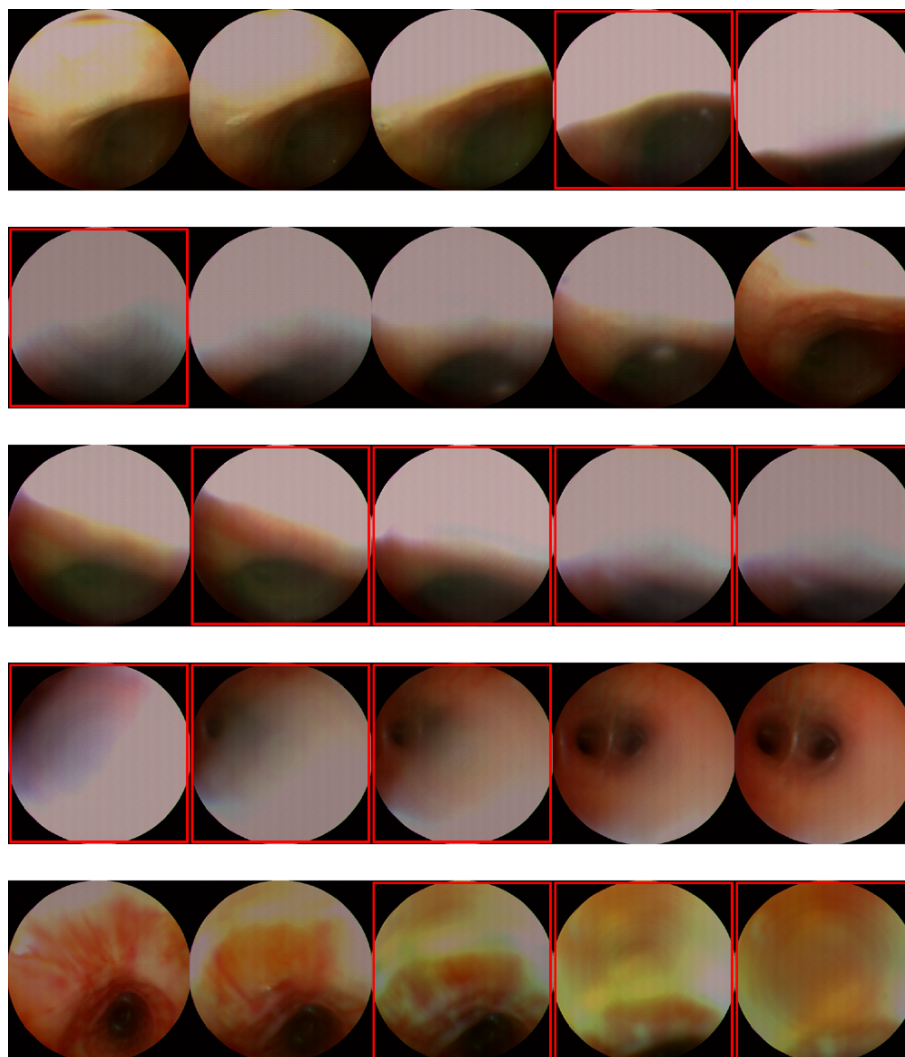


Figure 7.6: Rejection of obscured video images is denoted by a red outline in select frame sequences.

invariant measure of marginal and joint graylevel entropies[136], given by:

$$S_{NMI} = \frac{H(I^{CT}) + H(I^V)}{H(I^{CT}, I^V)} \quad (7.7)$$

where marginal entropies $H(I^{CT})$ and $H(I^V)$ are given by:

$$H(I) = - \sum_{i=0}^{M-1} p(i) \log p(i) \quad (7.8)$$

where $p(i)$ is the probability of each grayvalue occurring in the image, given a total of M grayvalues. The joint entropy $H(I, J)$ is generally given as:

$$H(I, J) = - \sum_{i=0}^{M-1} \sum_{j=0}^{M-1} p(i, j) \log p(i, j) \quad (7.9)$$

where $p(i, j)$ is the joint probability of grayvalues co-occurring at overlapping pixels.

A weighted variant of NMI, proposed by Helferty *et al.* was also tested as part of the CT-video registration[51]. In this adaptation, marginal and joint entropies $H_w(I^{CT})$ and $H_w(I^V)$ include an additional weighting factors. Equations 7.8 and 7.9 are rewritten as:

$$\begin{aligned} H_w(I^{CT}) &= - \sum_{i=0}^{M-1} \sum_{j=0}^{M-1} w_i w_j p_{CT,V}(i, j) \log p_{CT}(i) \\ H_w(I^V) &= - \sum_{i=0}^{M-1} \sum_{j=0}^{M-1} w_i w_j p_{CT,V}(i, j) \log p_V(j) \\ H_w(I^{CT}, I^V) &= - \sum_{i=0}^{M-1} \sum_{j=0}^{M-1} w_i w_j p_{CT,V}(i, j) \log p_{CT,V}(i, j) \end{aligned}$$

By setting $w_i = (M - i)/M$, this similarity metric S_{d_wNMI} places greater emphasis on darker image regions. The rationale for such weighting is that darker regions are further from the camera and contain a higher percentage of feature detail relevant to the anatomy. Conversely, brightly illuminated regions that are closer to the camera tend to suffer from over-exposure, and are subject to more dramatic variation in illumination intensity.

A shape-based similarity metric was tested by computing the 3D surface gradients from both the original image and the extracted surface model. To derive 3D surface gradients from the 2D image, the pq -space based approximation of Rashid and Berger [113] was used, where equation 7.5 is rewritten with respect to the surface gradient $\partial z_c / \partial x_c$ and $\partial z_c / \partial y_c$, given as p and q respectively:

$$I(x,y) = S_0 \rho \cdot \frac{(1 - xp - yq)}{z_c^2 (p^2 + q^2 + 1)^{\frac{1}{2}} (1 + x^2 + y^2)^{\frac{3}{2}}} \quad (7.10)$$

Without fully deriving the solution to p and q at any point (x,y) in I^V , it is given by the form:

$$\begin{aligned} A_1 p + B_1 q &= C_1 \\ A_2 p + B_2 q &= C_2 \end{aligned}$$

where the constants are computed from:

$$\begin{aligned} A_1 &= (-xR_x + 3)(1 + x^2 + y^2) - 3x^2 \\ B_1 &= -R_x(1 + x^2 + y^2)y - 3xy \\ C_1 &= R_x(1 + x^2 + y^2) + 3x \\ A_2 &= -R_y(1 + x^2 + y^2)x - 3xy \\ B_2 &= (-yR_y + 3)(1 + x^2 + y^2) - 3y^2 \\ C_2 &= R_y(1 + x^2 + y^2) + 3y \end{aligned}$$

with $R_x = I_x/I$ and $R_y = I_y/I$.

The resultant gradient image, ∇z_c^V , contains the surface gradient at each pixel (i, j) of I^V given by $\nabla z_c^V(i, j) = [p_{ij}, q_{ij}, -1]$. For the virtual image $I_{\bar{x}}^{CT}$, the gradient image ∇z_c^{CT} is evaluated by spatial differentiation of the z -buffer, which is supplied from OpenGL. The surface gradient is then described at each point (i, j) of $I_{\bar{x}}^{CT}$ as $\nabla z_c^{CT}(i, j) = [p'_{ij}, q'_{ij}, -1]$.

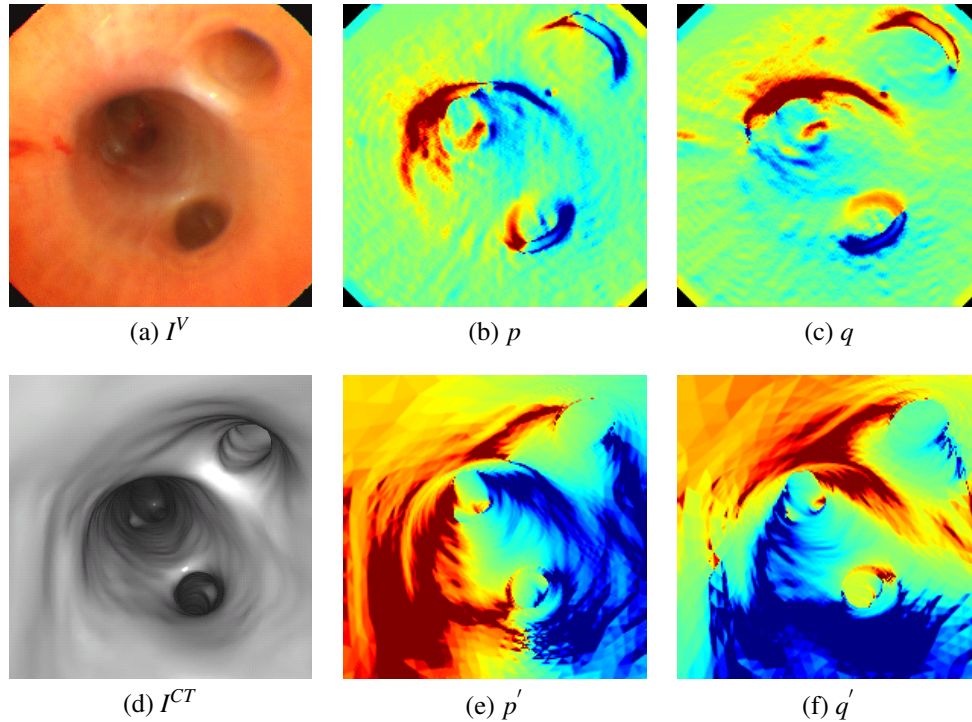


Figure 7.7: Differential surface analysis of real and virtual bronchoscopic images. Using pq -space approximation, the 2D input video frame (a) is converted to a vector image defining the x-(b) and y-(c) gradients, p and q , respectively. The gradients, p' and q' , of the CT-based reconstruction (d) are computed by differentiating the z -buffer (e) & (f).

Figure 7.7 displays the gradient images computed for matched real and virtual bronchoscopic images.

From this, the similarity between the virtual and bronchoscopic perspectives is evaluated on the basis of surface gradient alignment:

$$S_{SGA} = \sum_{i=0}^{N-1} \sum_{j=0}^{N-1} \frac{\nabla_{z_c^V}(i, j) \cdot \nabla_{z_c^{CT}}(i, j)}{\|\nabla_{z_c^V}(i, j)\| \cdot \|\nabla_{z_c^{CT}}(i, j)\|} \quad (7.11)$$

From equation 7.11, the similarity is computed as the normalized dot product of the surface gradients summed over the entire $N \times N$ image. This was further modified to include

a weighting factor w , given by:

$$S_{mwSGA} = \frac{\sum_{i=0}^{N-1} \sum_{j=0}^{N-1} w_{ij} \cdot \nabla_{z_c^V}(i, j) \cdot \nabla_{z_c^{CT}}(i, j) / (\|\nabla_{z_c^V}(i, j)\| \cdot \|\nabla_{z_c^{CT}}(i, j)\|)}{\sum_{i=0}^{N-1} \sum_{j=0}^{N-1} w_{ij}} \quad (7.12)$$

Similar to the approach by Deligianni *et al.*[22], the weighting term w_{ij} is set equal to the gradient magnitude $\|\nabla_{z_c^V}(i, j)\|$ permitting greater influence from high-gradient regions, and improving registration stability. However, limiting the weighting was found to be necessary, lest similarity be dominated by a very small number of pixels with spuriously large gradients. Thus, w_{ij} was set to $\min(\|\nabla_{z_c^V}(i, j)\|, 10)$.

7.4.1 Optimization

Given a similarity metric that appropriately gauges similarity between image pairs, registration requires an optimizer to effectively maximize similarity with the bounds of a search space. For the case of CT-video registration, at each frame an optimization of the position and pose \tilde{x} proceeds by:

$$\tilde{x} = \arg \max(I^V, I_{\tilde{x}}^{CT})$$

Given the dimensionality of the problem (6D), an exhaustive search is not possible, but instead must be bounded to a given subspace. Selection of a specific optimizer is often predicated on speed of convergence and overall robustness [56]. For this work, optimization of the registration was performed using CONDOR, which is a constrained non-linear optimizer for which the source code is publicly available². This optimizer was selected because it provided fairly rapid convergence and could be easily integrated into the custom image registration classes.

²<http://iridia.ulb.ac.be/~fvandenb/CONDORManual/CONDORManual.html>

7.4.1.1 Parameterization

Although a full description of the optimizer parameters is not provided here, it is important to describe the general scheme of the optimization used. First, it was deemed necessary to bound the registration search space to both speed registration and enforce convergence to a local maxima. Because the optimizer does not permit restraints, a penalty was added to the evaluation function to limit searching outside a bounding box of ± 10 mm and $\pm 20^\circ$ centered around the initial prediction of \tilde{x} . Under certain tracking conditions, performance was improved by adaptively resizing the bounding box based on dynamic modeling of the prediction error. For instance, improved tracking results were obtained by establishing a bounding box on the search space that was equivalent to 3 standard deviations of the prediction error measured over the last 10 frames while maintaining a hard maximal limit of ± 10 mm and $\pm 20^\circ$.

Another relevant component of the registration is the search space reference frame. At each frame, optimization was performed with respect to the initial camera coordinate frame rather than that of the CT image. The reason for selecting the camera's reference frame is that it allows characterization of more intuitive motions such as stepping forward or backward, and panning or rolling of the image. Because the virtual image changes far less for a step along the optical axis than perpendicular to it, the search intervals could be uniquely scaled to each of the principal axes of motion. Thus optimization intervals were much larger for movement along or rotation about the optical axis than that of the other two axes. For the optimizer used in this study, step changes in z -axis (the optical axis) motion and rotation were 5 times larger than the other rotations and orientations.

7.4.2 Light Source Calibration

The CT-video registration process is driven by inherent similarities between real and virtual images. This assumes that the virtual renderings adequately capture image features that are represented by the respective measures used for similarity comparison. Though it is

obvious that virtual reconstructions will not capture textural surface features (such as blood vessels) or color variations, overall appearance of the bronchial wall is heavily dictated by the bronchoscopic light source, which is constant (with the exception of *automatic gain control*) and capable of being modeled. Therefore, the registration implementation should consider the lighting dependent image features and their effect on similarity. The lighting calculation in OpenGL [164] for emission intensity of any surface point can be written as:

$$I = \underbrace{S_a \rho_a}_{\text{ambient}} + \frac{1}{k_c + k_l \|X_c\| + k_q \|X_c\|^2} \underbrace{\cos(\phi)^\varepsilon}_{\text{spotlight effect}} \left(\underbrace{\frac{S_d \rho_d \cdot (X_c \cdot \mathbf{n})}{\|X_c\|}}_{\text{diffuse}} + \underbrace{\frac{S_s \rho_s \cdot (X_c \cdot \mathbf{n})^\xi}{\|X_c\|}}_{\text{specular}} \right)$$

for a single light source coincident with the camera and oriented along the optical axis. The first term of the equation permits a user-defined quadratic attenuation function where k_c , k_l , and k_q are the constant, linear, and quadratic attenuation coefficients respectively. The spotlight effect is used to mimic the effect of vignetting described previously. The lighting components are broken into the ambient, diffuse and specular components, where S denotes the light source intensity, and ρ is the material reflectivity. The specular exponent ξ specifies the specular power of shininess of the surface.

The NMI-based registration process relies on direct graylevel entropies between corresponding regions of the real and virtual bronchoscopic images. Careful parameterization of the lighting model is necessary to tune the registration for optimal results. Unfortunately light source calibration and parameterization is rarely described in published findings. Higgins *et al.* is a rare exception, in which they specify the model parameters for simulation using a conventional bronchoscope [56]. In this work, attenuation values were set as $k_c = 1$, $k_l = 0$, and $k_q = 0.0025$, and the spotlight attenuation factor ε was set to 0.50. The specular component is of less critical importance, as it pertains to only a small image region at which the surface is orthogonal to incident light. However, calibration and modeling of the light source has been studied as a means of decoupling contributions from surface

texture, surface structure, and light source in the appearance of airways in bronchoscopic video [16, 111]. The result of such analysis is a lighting-invariant model of the airways that is useful for applications such as mosaicing [94], color analysis [141], and fusion of structural and textural surface information from bronchoscopy and MDCT [112]. Modeling of the light source for the purpose of CT-video registration does not require the same level of analysis. The lighting equations given here embrace a number of simplifications. These include assuming a constant surface reflectivity ρ , neglecting bidirectional reflectance, and disregarding the effects of multiple reflections.

The differential surface equation (7.10) from Rashid and Berger [113] serves as an approximation to the surface gradients assuming a more simple lighting model, as given by equation 7.5. Because similarity is measured from the surface mesh structure rather than the virtual rendering, corrections to the lighting model must be applied to the video frame I^V itself before computing the surface gradients. Namely, compensation for vignetting (see section 7.3) must be applied directly to the image, or else the model assumptions are invalidated. The exponential roll off in illumination intensity was empirically measured to be a function of the squared cosine of the angle ϕ ($\varepsilon = 2$).

7.5 Simulated Tracking of *In-Vivo* Video Images in Swine

From a total of six bronchoscopic sessions, four were selected for analysis. In each session, the SFB began in the trachea and was progressively extended further into the lung until limited by size or inability to steer. Each session constituted 600-1000 video frames, or 40-66 seconds at a 15 Hz frame rate, which provided sufficient time to navigate to a peripheral region. Two sessions were excluded, mainly as a result of mucus, which made it difficult to maneuver the SFB and obscured images. For each session, a starting position and pose $\tilde{\mathbf{x}}_0$ was located by an initial manually matching of $I_{\tilde{\mathbf{x}}_0}^{CT}$ to I_0^V . At each subsequent video frame I_k^V , the starting position and orientation estimate was set to the registered value, $\tilde{\mathbf{x}}_{k-1}$, from the previous frame.

7.5.1 Simulation Framework

The SFE guidance system was tested using data recorded from bronchoscopy. A test platform was developed on the Dell Precision 470 workstation with an ATI FireGL V5100 graphics card running Windows XP. The software test platform was developed in C++ using VTK which provides a set of OpenGL-supported libraries for graphical rendering. Before simulating tracking of the bronchoscope, an initial image analysis stage crops the lung region of the CT image, performs a multi-stage airway segmentation algorithm, and applies a contouring filter from VTK to produce a surface model of the airways.

7.5.2 Evaluation of Simulated Tracking Accuracy

Validation of the tracking accuracy is somewhat limited by the lack a definitive gold standard. As an alternative, registrations were performed manually at a set of key frames, spaced at every 20th frame of each session. Manual registration requires a user to manipulate the position and pose of the virtual camera to qualitatively match the real and virtual bronchoscopic images by hand. The tracking error E^{key} is given as the root-mean-square (RMS) positional and orientational error between the manually registered key frames and IBT outputs.

For each similarity metric, CT-video registration was considered to be accurately tracking the bronchoscope position provided the position error was less than 10 mm and the pose error was less than 20° when compared to the manually registered key frames. Once the registration failed to fall within these imposed limits in three consecutive key frames, the registration was considered to be outside the capture range and thus had diverged from the true bronchoscopic path marked by the manual key frame registrations. The session was then restarted at the position of the manually registered key frame preceding the tracking failure. The selected limits were imposed as a natural limit to the registration. For practicality, the 6D search-space of the registration optimizer was limited to a distance of 10 mm maximum from the initial predicted position. Increasing the size of the search space,

though potentially more robust, increases the time of the registration and increases the likelihood that registration converges to an incorrect local maximum, resulting in inaccurate matches.

7.5.3 Results

The key frame error E^{key} for each of the sessions is provided in Table 7.2 with respect to each similarity metric tested. The RMS position error was 55.17 mm, 46.67 , 28.77 mm and 15.55 mm for S_{NMI} , S_{dwNMI} , S_{SGA} and S_{mwSGA} , respectively. Overall, the tracking accuracy is much better for SGA-based CT-video registration than for NMI-based metrics. While these errors are intolerable for adequate targeting of a 10 mm nodule, the error values largely reflect the results of divergent tracking. To assess stability of the tracking metric, Table 7.3 reports the number of tracking failures that occurred during each of the sessions. Over all frames of all sessions, divergent tracking occurred only twice using the S_{mwSGA} metric. By comparison, divergent tracking was observed a total number of 32, 20, and 10 times for S_{NMI} , S_{dwNMI} , and S_{SGA} metrics, respectively.

Figure 7.8 depicts the tracking time-plot in all 6 dimensions during session 1 with respect to the video frame number. At the start of the session, IBT appears to accurately follow the plot of the key frames. However, at some point, IBT appears to diverge from the path, resulting in aberrant localization of the SFE. Divergent tracking may be the result of obscured video images, insufficient anatomical detail, large interframe motion that cannot be captured by CT-video registration, or simply using a similarity measure that is not sensitive to the most relevant matching features. From the plots in session 1, the SGA-based metrics appear to be more robust in tracking the SFE over multiple frames. However, as evident from the plot of θ_z in Figure 7.8, the SFB was twisted rather abruptly at around frame 550, causing a severe change in orientation that could not be recovered by CT-video registration. This change in the *roll* orientation term causes subsequent misalignment and divergent tracking. The time-plot continues to track the position with reasonable accuracy, however, the orientation is flipped 180° out of alignment, which would severely confuse

Table 7.2: RMS Positional and orientational tracking error E^{key} between IBT output and manually registered key frames.

$E_x^{key} / E_\theta^{key}$ (mm/°)	session 1	session 2	session 3	session 4	Average
NMI	30.05 93.75°	66.84 65.79°	52.82 128.85°	70.98 143.29°	55.17 107.92°
dwNMI	36.75 88.60°	63.15 94.78°	23.06 23.53°	63.73 103.65°	46.67 77.64°
SGA	17.34 98.42°	11.44 134.22°	23.15 79.27°	63.15 94.78°	28.77 101.67°
mwSGA	6.01 110.62°	4.36 10.07°	11.64 23.12°	40.18 56.00°	15.55 49.95°

Table 7.3: Number of tracking failures experienced during each tracking session using each of the three similarity metrics.

Similarity Metric	session 1	session 2	session 3	session 4	Total
NMI	6	12	6	8	32
dwNMI	6	7	2	5	20
SGA	2	2	3	3	10
mwSGA	1	0	1	0	2

the bronchoscopist.

A tracking collage is featured in Figure 7.10, showing selected video frames and the corresponding matched virtual images following CT-video image registration using each of the similarity metrics. In the first two frames (40 and 140), results from both NMI- and SGA- based metrics are comparable. However, around frames 240-340, registration is challenged by lack of anatomical detail. Using NMI, tracking diverges from the true path, while SGA-based registration remains relatively stable. Registration by SGA eventually fails at frame 550 as discussed above.

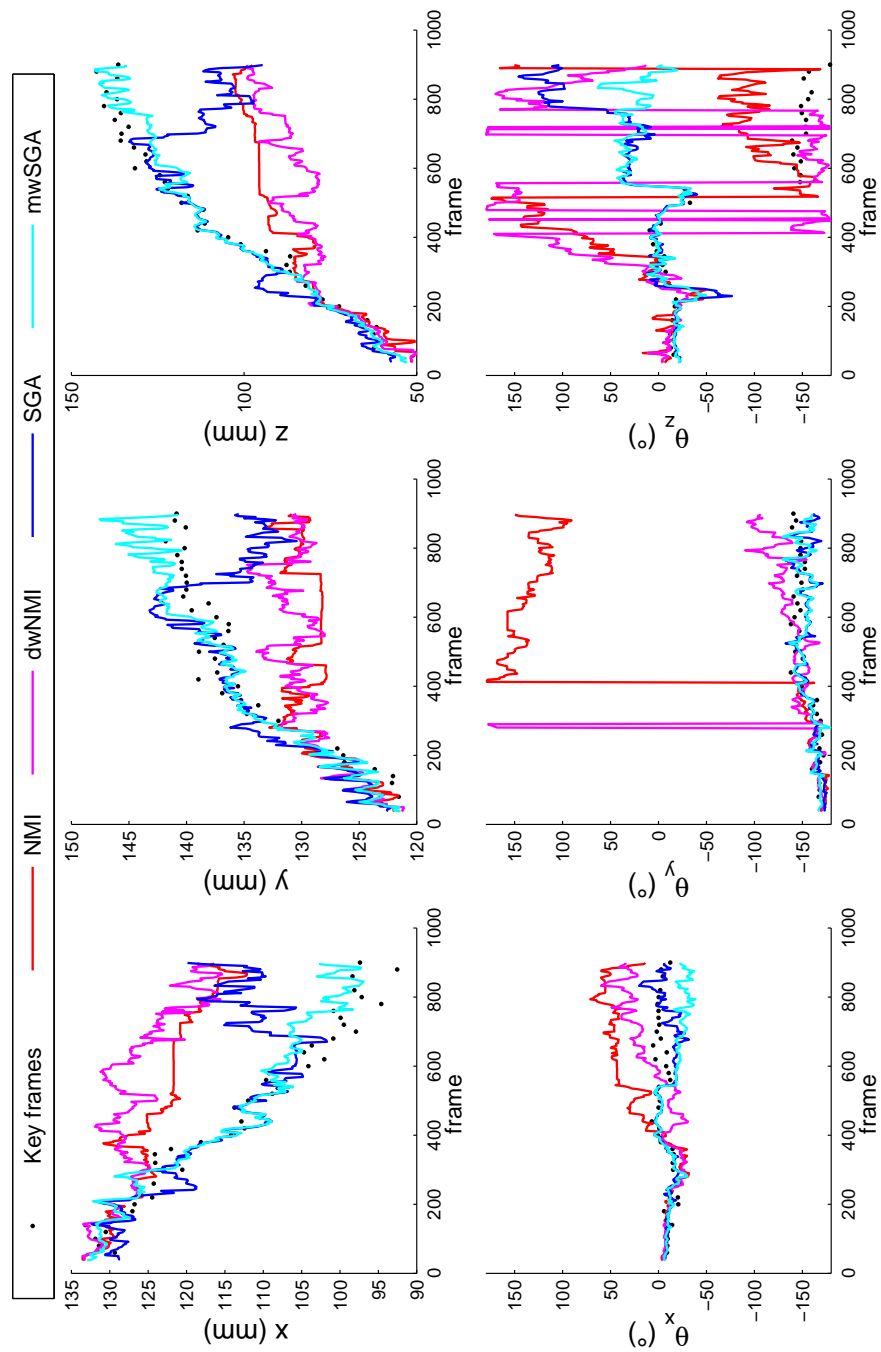


Figure 7.8: Plot of IBT of the SFE during session 1 of a live pig experiment

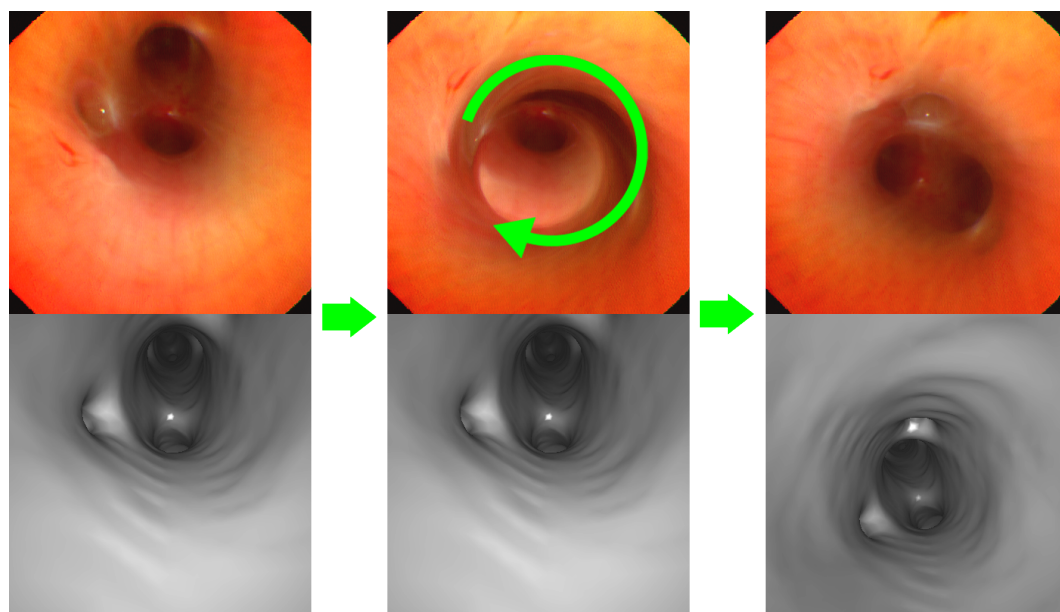


Figure 7.9: Example of divergent tracking resulting from large interframe motion. At approximately frame 550 of session 1, the SFE was abruptly twisted clockwise by 90° . Using IBT, the virtually tracked position cannot overcome the large motion.

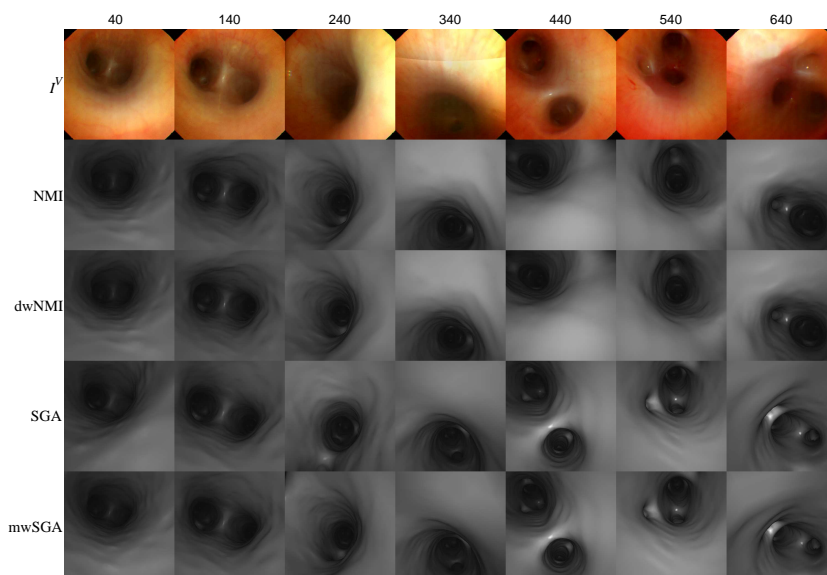


Figure 7.10: Collage of CT-video registration results at selected frames using each of the similarity metrics.

7.6 Conclusions

Results from initial experiments using CT-video registration for IBT of the SFE show that it can provide accurate localization through many frames. This was counterbalanced by the observed sensitivity to obscured video images or large interframe motion, which caused aberrant tracking. Table 7.2 quantifies the localization error for both NMI-based and gradient alignment-based similarity metrics. We found the use of the 3D surface gradients computed from surface analysis provided a more accurate robust means of tracking the SFE with positional errors of 28.77 mm and 15.55 mm for the standard and magnitude-weighted variants, respectively. The NMI-based metrics performed far worse, yielding average localization errors of 55.17 mm and 46.57 mm for standard and dark-weighted variants, respectively. As mentioned, these errors are considerable, and reflect the tendency toward divergent tracking rather than quantifiable estimates of localization accuracy over frames during which the video and virtually tracked images appropriately match. NMI-based metrics produced 32 and 20 failures over the course of four bronchoscopy sessions. The gradient alignment-based metrics produced 10 and 2 failures over the same sessions. From this, it was decided that the surface gradient alignment metric would be used for all future tracking experiments. In particular, the magnitude-weighted variant was applied due to its superior performance, though it is noted that setting an upper limit to the gradient weighting was essential. This helped to limit contributions from spuriously large gradient values computed from the pq -space equations.

7.7 Discussion

The superior performance of the SGA-based similarity metrics is believed to be attributed to its inherent emphasis of more salient image features. Similarity using SGA is more heavily influenced by correspondence of edge features such as bifurcations. With NMI-based metrics, matching is driven by global similarity in intensity variation. Despite superior IBT

results using the SGA metric, localization error of SGA and NMI was far more comparable for the EB-1970K bronchoscope (data not shown). It is our perception that the SGA metric is particularly better suited to video acquired by the SFE. The current SFE embodiment is a working prototype without formalized methods of manual or automatic laser power adjustment and gain control. As a result, scanned illumination is less consistent than that of conventional wide-field sources. The data collected from this experiment was obtained at lower illumination levels which did not penetrate as deeply as that of the conventional bronchoscope. As such, NMI-based metrics, which rely heavily on accurate modeling of the light source, prove to be less ideal for CT-video registration in this application. It is possible that NMI and dwNMI performance could be improved through tuning of the rendering parameters. Adjustment of the material properties, light attenuation coefficients, or spotlight exponent may help to better mimic the appearance of SFE video images. However, the SGA approach is particularly attractive in this respect, as it does not require any tuning of parameters. With regard to the illumination model, however, it was noted that CT-video registration by means of SGA performed particularly poorly prior to inception of the vignetting compensation stage during preprocessing of each video frame. This implies that the pq -space surface gradient approximation can be particularly sensitive to inaccuracies in the lighting model.

7.7.1 Study Limitations

7.7.1.1 Computational Speed

The current CT -video registration algorithms are computationally expensive. On average, 1.92 seconds were required to match each virtual and real bronchoscopic image. This is also a low estimation of the processing time, as it is influenced by faster registration times from portions of the procedure during which aberrant tracking occurred. This is particularly evident in video sequences where the virtual endoscope has stepped outside the virtual airway model altogether, producing only a black screen: in this case similarity

is uniform and more rapidly converges to a trivial solution. For each match, approximately one hundred evaluations of the objective function are performed by the optimizer. That is to say, one hundred virtual bronchoscopic reconstructions are rendered and evaluated to produce a final match.

This is considerable time required for CT-video registration and would not support any real time tracking endeavor. However, maximizing computation time was not a major focus of this work. In Chapter 9, possible amendments to the code and alternative hardware configurations are discussed for future live guidance scenarios. Though the means of CT-video registration are not identical to those of other researchers, optimism is warranted as investigation into rapid CT-video registration schemes has produced per-frame processing times of $1/15^{th}$ of a second [93, 138].

7.7.1.2 Interframe Motion Estimation from Video Images

Aberrant tracking of the scope was affected in this study by large interframe motion. However, improved CT-video registration has been achieved in previous work by implementing an initial motion estimation stage by direct comparison of subsequent video frames. Given only a rough estimation of the interframe motion, a more precise initial estimate of the scope position and orientation can be acquired, thereby reducing the potential for divergent tracking. A number of studies estimate motion of the scope by computing motion vectors of smaller subregions of the image. Mori *et al.* computed motion vectors of image subregions by locating the maximum correlation of small image tiles between consecutive images [101]. For simplicity, motion was categorized as forward, backward, or otherwise motion, which limited the optimization of the bounds during CT-video registration. Bulat *et al.* expanded on the motion characterization to four dimensions by including orientation components [11]. A similar approximation of the scope motion was also computed using epipolar geometry analysis [98].

Alternatively, interframe motion can also be assessed on the basis of mathematical modeling of the scope motion over several frames. Nagao *et al.* implemented a Kalman filter to

model bronchoscope motion using first and second order kinematic equations [104]. Deligianni *et al.* also researched a predictive tracking algorithm based on a particle filters, where motion was approximated by a second-order auto-regressive model [22]. For this work, interframe motion was not computed prior to CT-video registration. Methods, such as those mentioned here may provide an improved approach to tracking. Future modifications may employ such models for improved IBT, though future chapters discuss use of EMT to predict interframe motion.

7.7.1.3 SFE Limitations

IBT applied to bronchoscopic sessions using the SFE are affected by limitations in the scope design and imaging capabilities. From the results of camera calibration, it could be seen that estimation of the SFE homography was far less accurate than that of a conventional bronchoscope. This is due to the fact that distortion present in the SFE images is not only introduced from the lens system, but also nonparameteric distortion in the electromechanical actuation of the fiber in a spiral scan path, particularly at the image center. Unfortunately, the radial distortion model from equation 7.2 cannot effectively model this eccentricity, producing an incomplete correction. A more thorough calibration may need to be implemented. However, the effective scan profile varies after each calibration. Thus, any distortion correction procedure would need to be performed during each use.

Inability to steer the SFE presented a further obstacle to IBT. For the animal experiments, the SFE had to be passively extended through multiple airway generations. This resulted in a number of situations where video images either became obscured by mucus, or were dominated by airway wall regions, and thus lacked sufficient detail to inform the CT-video registration algorithm. Such frames contributed heavily to aberrant tracking. Future incorporation of a steering mechanism will allow the bronchoscopist to better stabilize the scope by reorienting its view toward more prominent features, as well as avoiding or removing mucus.

Chapter 8

HYBRID TRACKING

In Chapter 5 guided navigation of a rigid benchtop model was performed using EMT. Accurate registration between real-world and CT image coordinates permitted real-time localization of the scope within defined airways. However, translation of this methodology to deformable system resulted in large registration errors. Simultaneously, the IBT methodology discussed in Chapter 7 provides a means of accurate tracking, though it is highly perceptible to disruption caused by obscuring or obstruction of the SFE view or large by interframe motion.

In a hybrid tracking system, the stability of EMT and accuracy of IBT are simultaneously leveraged. Using EMT, the CT-video registration search space is effectively bound to the sensor position and pose, thereby preventing divergent tracking. In the hybrid strategy proposed by Mori *et al.*, successful tracking was validated within an airway phantom using simulated respiratory motion [96]. This system and its validation were, however, limited. First, the EMT sensor was only 5 DoF and required an additional 1D image-based optimization stage to recover the roll term. Second, the system was evaluated within a rigid model and applied only simulated respiratory motion to the EMT sensor. Deligianni *et al.* later noted that the respiratory-induced misalignment between EMT and IBT significantly hampered tracking accuracy [23]. They therefore compensated for respiratory deformation using Active Shape Models derived from multiple CT scans of a deformable phantom. Although results were promising, modeling of the airway deformation by repeated CT scanning may prove to be clinically infeasible.

For navigation of the SFE in peripheral airways, a custom hybrid tracking system was

developed using an EMT system and miniature sensor (Ascension Technology Corporation, Burlington, VT) and IBT of the SFE video with a preoperative CT [135]. First, a free-hand system calibration technique is described for registering the 2D pixel space of the SFE to the 3D operative environment defined by the EMT system. As part of the intraoperative localization framework, a Kalman filter is employed to adaptively estimate the positional and orientational error between these two tracking inputs. Furthermore, a means of compensating for respiratory motion by intraoperatively estimating the local deformation at each video frame is proposed. The hybrid tracking model is described further in the methods section and was evaluated by using it for *in vivo* navigation within a live pig.

8.1 SFE-EMT System Registration

In section 7.2, intrinsic and extrinsic camera parameters were computed by free-hand multiperspective imaging of a test target. This established a mapping between the 3D camera coordinate frame and the 2D pixel space of the video buffer. In the hybrid approach, the SFE is tracked by attaching miniature 6DoF position sensor to the distal tip. This introduces the additional coordinate frames of the EMT field generator and the sensor. As part of the SFE-EMT calibration, we seek the transformation T_{sc} gives the position and pose of the camera in sensor coordinates.

SFE-EMT registration is performed using the same free-hand calibration technique described previously. The only modification is that the test grid is arbitrarily placed within the trackable volume of the EMT system, and the sensor position and pose is recorded with each acquired video frame. Figure 8.1b depicts the calibration setup. Because the SFE is tracked within an operative volume defined by the EMT system, the field generator serves as the world coordinate frame. As such, the extrinsic camera parameters, denoted as T_{wc} in section 7.2, are denoted here as T_{gc} , or the variable transformation between the test grid and the moving camera. For each of the N calibration images used, the transformations $T_{gc}^1, T_{gc}^2, \dots, T_{gc}^N$ are computed from the camera calibration toolbox, for which there are also

corresponding sensor readings $T_{ws}^1, T_{ws}^2, \dots, T_{ws}^N$. These are combined with the unknown constant transformations T_{sc} and T_{gw} to form the following system of equations:

$$\begin{aligned} T_{gc}^1 &= T_{sc} \times T_{ws}^1 \times T_{gw} \\ &\vdots \\ T_{gc}^N &= T_{sc} \times T_{ws}^N \times T_{gw} \end{aligned} \quad (8.1)$$

or in respective rotational and translational components, R and \mathbf{t} :

$$R_{gc}^i = R_{sc}(R_{ws}^i(R_{gw})) \quad (8.2)$$

$$\mathbf{t}_{gc}^i = \mathbf{t}_{sc} + R_{sc}(\mathbf{t}_{ws}^i) + R_{sc}(R_{ws}^i(\mathbf{t}_{gw})) \quad (8.3)$$

To solve for the two fixed transformations, T_{sc} and T_{gw} , we employ the direct linear solution proposed by Konen *et al.* [77]. First, the unknown rotations R_{sc} and R_{gw} computed by solving the linear system from equation 8.1. Using the constraint of orthogonality, where $R_{sc}^T R_{sc} = R_{gw}^T R_{gw} = 1$, the problem can be rewritten in a simplified linear form as:

$$\mathbf{Cz} = 0$$

where \mathbf{z} is an 18-element column vector containing the concatenated elements of R_{sc} and R_{gw} :

$$\mathbf{z} = [R_{sc11}, R_{sc12}, \dots, R_{sc33}, R_{gw11}, R_{gw12}, \dots, R_{gw33}]^T$$

and \mathbf{C} is a $9N \times 18$ matrix. For each calibration image, the corresponding i th element of \mathbf{C} is given as:

$$\mathbf{C}^i = \begin{pmatrix} -r_{ws1}^i & 0 & 0 & r_{gc1}^i & 0 & 0 \\ -r_{ws2}^i & 0 & 0 & 0 & r_{gc1}^i & 0 \\ -r_{ws3}^i & 0 & 0 & 0 & 0 & r_{gc1}^i \\ 0 & -r_{ws1}^i & 0 & r_{gc2}^i & 0 & 0 \\ 0 & -r_{ws2}^i & 0 & 0 & r_{gc2}^i & 0 \\ 0 & -r_{ws3}^i & 0 & 0 & 0 & r_{gc2}^i \\ 0 & 0 & -r_{ws1}^i & r_{gc3}^i & 0 & 0 \\ 0 & 0 & -r_{ws2}^i & 0 & r_{gc3}^i & 0 \\ 0 & 0 & -r_{ws3}^i & 0 & 0 & r_{gc3}^i \end{pmatrix},$$

where $r_{ws_j}^i$ is the transposed j th column of R_{ws}^i , and $r_{gc_j}^i$ is the j th row of R_{gc}^i . Given a sufficient number of input images at varied positions and orientations, a nontrivial solution \mathbf{z} is a vector in null space of \mathbf{C} . The solution, is calculated from singular value decomposition of \mathbf{C} , given by:

$$\mathbf{C} = \mathbf{U}\mathbf{S}\mathbf{V}^T$$

where \mathbf{z} is the column vector of \mathbf{V}^T corresponding to the smallest value of \mathbf{S} . Lastly, for the solution \mathbf{z} to be orthogonal, it is scaled to satisfy the boundary condition $\|\mathbf{z}\| = \sqrt{6}$. Likewise, the translation components \mathbf{t}_{sc} and \mathbf{t}_{gw} are computed as the least-square solution to $\|\mathbf{L}\mathbf{x} - \mathbf{b}\|$ by substitution from equation 8.3, where:

$$\mathbf{L} = \begin{pmatrix} I & R_{sc}R_{ws}^1 \\ \vdots & \vdots \\ I & R_{sc}R_{ws}^N \end{pmatrix}, \text{ and } \mathbf{b} = \begin{pmatrix} \mathbf{t}_{gc}^1 - R_{sc}\mathbf{t}_{ws}^1 \\ \vdots \\ \mathbf{t}_{gc}^N - R_{sc}\mathbf{t}_{ws}^N \end{pmatrix}$$

and I is a 3×3 identity matrix.

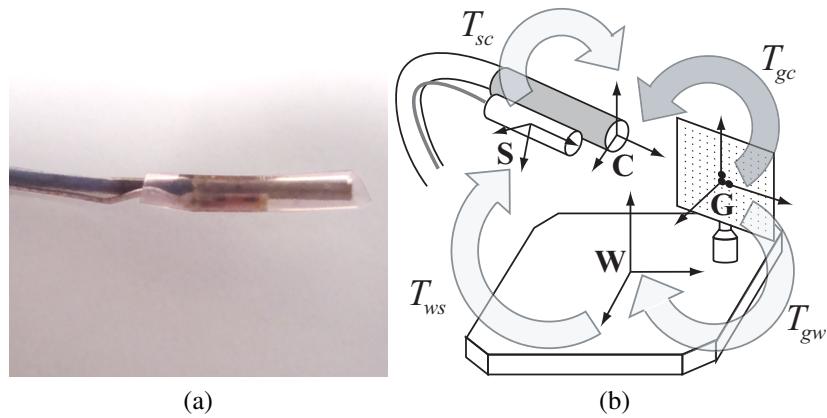


Figure 8.1: The miniature 1.3 mm OD, 6 DoF EMT sensor is fixed to the SFE distal tip using a thin piece of Silastic tubing (a). The free-hand calibration diagram is shown in (b). From the set of paired video frames and sensor readings, four transformations are computed that map the coordinate systems of the world (W), sensor (S), camera (C), and test target (T).

8.1.1 Results

Calibration and system registration was performed in the same manner as that for camera calibration previously. The same test target was placed within the tracked volume and imaged using the SFE from multiple perspectives, just prior to bronchoscopy. The 1.3 mm position sensor was affixed to the SFE using a small piece of Silastic tubing (Figure 8.1a). Affixing the sensor using tape was also tried, but proved to be ineffective. First, when wetted by mucus, the tape fails to hold the sensor rigid, allowing it to twist and move independent from the SFE. Also, the tape edges appeared to irritate the airways, causing bleeding and increased mucus production.

From a set of approximately 20 calibration images, the SFE and EMT sensor was calibrated prior to bronchoscopy. Figures 8.2a and 8.2b depict each 6D camera position T_{gc}^i located from camera calibration (*magenta*) as well as the 6D position $T_{gw} \cdot T_{ws} \cdot T_{sc}$ predicted by SFE-EMT registration (*cyan*). Table 8.1 lists the computed values for the translation t_{sc} and the rotation angles θ_{sc} , which define the camera position and orientation in sensor coordinates. The system registration errors are also given, where E_x is the mean position error,

given by:

$$E_x = \frac{\sum_{i=1}^N \|\mathbf{t}_{gc}^i - [\mathbf{t}_{sc} + (R_{sc} \times \mathbf{t}_{ws}^i) + (R_{sc} \times R_{ws}^i \times \mathbf{t}_{gw})]\|}{N}$$

and the mean orientation error E_θ is:

$$E_\theta = \frac{\sum_{i=1}^N \cos^{-1}(\text{trace}([R \times R_{ws}^i \times R_{gw}]^{-1} \times R_{gc}^i) - 1)}{N}$$

For two calibration procedures performed with the SFE, the registration error was 1.51 mm and 2.35° in the first procedure and 1.49 mm and 2.12°. These small error values are very positive and validate the accuracy of the registration procedure. Furthermore, this is accomplished by an easy free-hand calibration procedure using an arbitrarily placed test grid. There is no need to control or directly specify transformations between the world, test grid, sensor, and camera coordinate frames as has been done previously [66]. An error value within 1-2 mm is within the range of the EMT system itself and the camera calibration with some discernible distortions. The values of \mathbf{t}_{sc} are also very sensible. From the sensor coordinate frame, the offset of the camera is primarily along the sensor's x (long) axis. There is also a much smaller in-plane offset between the sensor axis and SFE axis. The inconsistent registration values between the two calibrations reflect the random attachment location of the sensor to the SFE prior to each session.

Table 8.1: The translation \mathbf{t}_{sc} , rotation angles θ_{sc} , and mean registration errors E_x and E_θ are provided for two SFE-EMT registration procedures.

	\mathbf{t}_{sc}	θ_{sc}	$E_x(\sigma)$	$E_\theta(\sigma)$
SFE cal 1	5.04, -1.17, -0.11	18.4°, 41.5°, 164.2°	1.51 (0.99)	2.35° (3.27°)
SFE cal 2	15.52, 0.31, 3.79	18.8°, 17.0°, -125.0°	1.49 (1.18)	2.12° (1.07°)

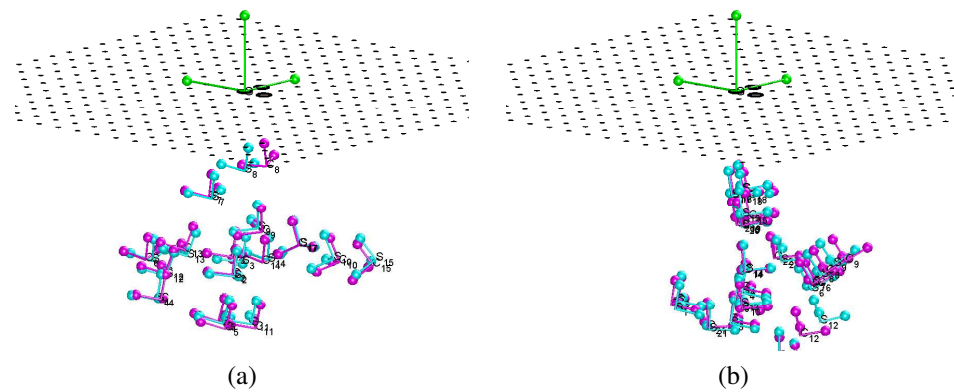


Figure 8.2: The results of SFE-EMT registration are shown from two separate free-hand calibration procedures. The *magenta* coordinate frames were computed using the calibration toolbox from multiple images of a test target, yielding the extrinsic camera parameters T_{gc}^i for each image. Agreement is compared to the camera position and orientation $T_{sc} \times T_{ws}^i \times T_{gw}$ estimated from the EMT sensor.

8.2 CT Image – World Registration

Following system calibration, the transformation between coordinate systems within the operative environment are defined. In particular, that of the camera with relationship to the tracked sensor, or T_{sc} . Still lacking is the coordinate of the anatomy, which to this point, has no relationship to the operative environment. To map the position of the SFE, tracked in world coordinates, into CT image coordinates, relative to a targeted nodule, a rigid registration must be performed between the actual and virtual anatomies. To compute this mapping, a point based registration was performed using corresponding landmarks.

The registration first required localization of branchpoint features within the airway anatomy. Although external markers can be used, anatomical landmarks within the airways provide a more accurate registration [131]. For this task, the EB-1970K bronchoscope was used to bronchoscopically image and locate points throughout the central airways. A custom plastic stylus was made to fit snugly into the distal end of the working channel of the bronchoscope while fitting over the EMT sensor so as to track the stylus tip. A plastic guard was placed over the stylus to prevent scraping of puncturing of the airways. As part of the localization, the stylus offset had to be calibrated into the sensor measurement. This

was done using the method of Hartov *et al.* [48] by tracking the scope-sensor-stylus system while rigidly rotating the stylus around a pivot point.

During landmark localization, ventilation of the animal was momentarily suspended to match the same static lung pressure used during CT scanning in an effort to reproduce the same airway configuration. A total of 8 to 10 branch points were located using the stylus along the trachea and the left and right mainstem bronchi. The corresponding points were later located within the virtual airway model. Two examples of branchpoints located during bronchoscopy and the corresponding points in the virtual airway model are depicted in Figure 8.3. From these points, an optimal rigid registration T_{wi} was computed between world and CT image coordinates using the closed-form solution proposed by Horn [61].

Figure 8.4 depicts the registration of EMT-located anatomical landmarks to corresponding virtual landmarks located in the CT image. A total of ten points were selected from the trachea, main carina, and branchpoints along both the right and left mainstem bronchi. The degree of landmark overlap expresses the accuracy of the registration procedure. Though some landmarks align reasonably well, there is a perceptible degree of fiducial registration error (FRE) in the alignment of several landmarks. The FRE for this example was approximately 2.28 mm, and is consistent with other experiments.

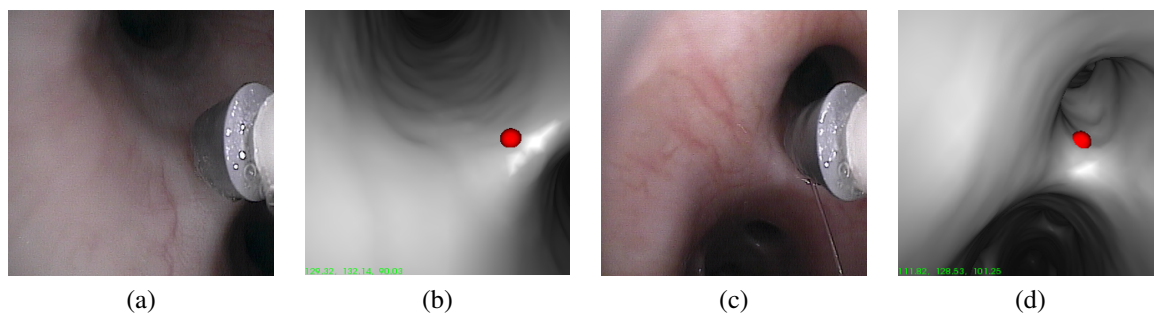


Figure 8.3: Localization of corresponding landmarks in both real and virtual anatomies is the basis of registration between world and CT image coordinates. Branchpoint features were located using by a tracked stylus (a&c), for which the corresponding CT image locations were manually identified (b&d).

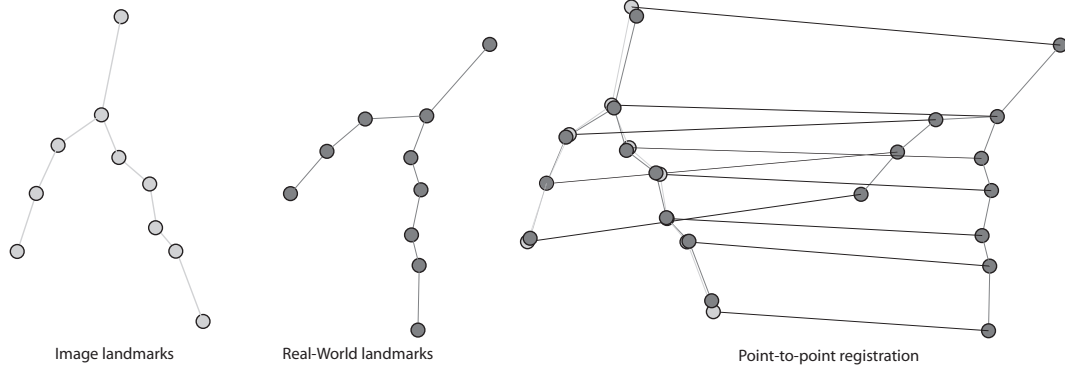


Figure 8.4: World to CT image rigid point registration is performed using corresponding landmarks.

8.3 Hybrid Tracking Model

Both EMT and IBT constitute independent estimates of the position and pose, $\tilde{x} = [x^T, \theta^T]^T$, of the SFE in static CT coordinates, as it navigates through the airways. For clarity, the 6D position \tilde{x} (including the tilde) is a 6-element column vector expressed as the concatenation of the 3-element position and orientation column vectors, x and θ , where θ is expressed in Euler angles. In the hybrid implementation, the position and pose recorded by the EMT sensor \tilde{x}_{E_k} provides an initial estimate of \tilde{x}_k at the k th video frame. Here, \tilde{x}_E is used for convenience to mean the 6D position of the SFE as estimated by the EMT sensor in CT coordinates, such that:

$$x_E = t_{wi} + R_{wi} \times t_{ws} + R_{wi} \times R_{ws} \times t_{sc} \quad (8.4)$$

$$R(\theta_E) = R_{wi} \times R_{ws} \times R_{sc} \quad (8.5)$$

where $R(\theta)$ denotes the 3×3 rotation matrix computed from the Euler angles in θ . The EMT-predicted SFE position is then optimized to \tilde{x}_{I_k} by IBT. Using this approach, the 6D SFE position is first roughly estimated by the EMT sensor and then more subtly refined by IBT.

The positional registration error between the real anatomy in world coordinates and the

virtual anatomy in CT image coordinates is modeled as a discrepancy between two tracking sources, and given by:

$$\mathbf{x}_{I_k} = \mathbf{x}_{E_k} + \boldsymbol{\delta}_k \quad (8.6)$$

Assuming \mathbf{x}_{I_k} to be an accurate measure of the true SFE position in the static CT image, $\boldsymbol{\delta}$ is the local registration error between the actual and virtual airway anatomies, given by $\boldsymbol{\delta} = [\delta_x, \delta_y, \delta_z]^T$. This can be thought of as a slowly varying, position-dependent secular registration error between the real and virtual anatomies as demonstrated in Figure 8.5. To optimize tracking performance, it is ideal to provide an accurate prediction $\tilde{\mathbf{x}}_{I_k}^-$ of the 6D SFE position prior to CT-video registration. Thus at each frame k , the predicted position of the SFE is given by $\mathbf{x}_{I_k}^- = \mathbf{x}_{E_k} + \boldsymbol{\delta}_k^-$ prior to CT-video registration, where $\boldsymbol{\delta}_k^-$ is the predicted positional registration error at the current frame.

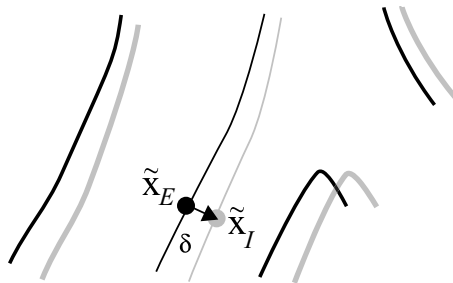


Figure 8.5: Registration error between the real anatomy (*black*) and the virtual anatomy (*gray*) is modeled by a secular error $\boldsymbol{\delta}$.

8.3.1 The Kalman Filter

Equation 8.6 defines a discrete process model given two inputs measurements, \mathbf{x}_E and \mathbf{x}_I , and an unknown variable $\boldsymbol{\delta}$. As part of the tracking algorithm, a *Kalman filter* is used to adaptively model the process.

Generally, the Kalman filter estimates the unknown state of any time-controlled process from a set of noisy and uniformly time-spaced measurements [69]. The unknown process

state y is generally modeled as:

$$y_k = Ay_{k-1} + w_{k-1} \quad (8.7)$$

with a set of measurements z given by:

$$z_k = Hy_k + v_k \quad (8.8)$$

where w and v are the process and measurement noise variables given by the normal distribution:

$$p(w) = N(0, Q)$$

$$p(v) = N(0, R)$$

where Q and R are the *process noise covariance* and *measurement noise covariance*, respectively. For an n -dimensional process state vector y , A is an $n \times n$ state transition matrix, which relates the current state y_k to the state at the previous timestep y_{k-1} . For an m -dimensional measurement z , the $m \times n$ measurement matrix H relates the measurement z to the process y with added measurement error v .

The discrete Kalman filter uses the measurements as a form of feedback from which the process noise is estimated and a future process state is predicted. The Kalman filter essentially uses *a posteriori* measurements of a process to predict future process states *a priori*. The discrete Kalman filter is composed of a recursive two-step prediction stage and subsequent measurement-update correction stage. At each measurement k , an initial prediction of the Kalman state \hat{y}_k^- and process error P_k^- is given by:

$$\begin{aligned} \hat{y}_k^- &= A\hat{y}_{k-1} \\ P_k^- &= AP_{k-1}A^T + Q \end{aligned} \quad \text{(time-update prediction)} \quad (8.9)$$

In the second step, the corrected state estimate \hat{y}_k is calculated from the measurement z_k using:

$$\begin{aligned} K_k &= P_k^- H^T (H P_k^- H^T + R) && \text{(measurement-} \\ \hat{y}_k &= \hat{y}_k^- + K_k (z_k - H \hat{y}_k^-) && \text{update} \\ P_k &= (I - K_k H) P_k^- && \text{correction)} \end{aligned} \quad (8.10)$$

where K is an $m \times n$ matrix, referred to as the Kalman gain matrix. It serves as a blending factor that adaptively adjusts weights between the current and past measurements to minimize the process error P . Matrix I is simply an $m \times m$ identity matrix.

From the stochastic Kalman equations, an optimal prediction of a process state can be computed in a Bayesian sense. For such reasons, Kalman filters have found wide use in a number of tracking applications using single-source or multiple-source observations. A good introduction to the Kalman filter and its use is provided by Welch and Bishop [160], which can be found online, along with a number of other educational resources¹.

8.3.2 Hybrid Tracking Using an Error-State Kalman Filter

From the process definition given in (8.6), an error-state Kalman filter is used to recursively compute the registration error between x_E and x_I from the error state $\hat{y} = \delta$. At each new frame, an improved initial position estimate $x_{I_k}^-$ is computed from the predicted error state \hat{y}_k^- in (8.9), where $x_{I_k}^- = x_{E_k} + \delta_k^-$. Following CT-video registration from $x_{I_k}^-$ to x_{I_k} , the measured error z_k is computed from $z_k = x_{I_k} - x_{E_k}$. A measurement update is then performed in (8.10). In this way, the Kalman filter adaptively recomputes updated measurements of δ , which varies with time and position in the airways. The hybrid tracking methodology is outlined further in Algorithm 1. At the start of each hybrid tracking simulation, A and H were initialized to identity.

Further optimization of the tracking algorithm was attempted through the addition of a rotational correction term in addition to the positional offset given in equation 8.6. The

¹<http://www.cs.unc.edu/~welch/kalman/>

correctional term θ_{Δ} was used to denote the set of three Euler angles, $\theta_{\Delta} = [\theta_{\Delta_x}, \theta_{\Delta_y}, \theta_{\Delta_z}]^T$ to correct for the orientation error by:

$$R(\theta_{I_k}) = R(\theta_{E_k}) \times R(\theta_{\Delta_k}) \quad (8.11)$$

The process state \hat{y} is now given as $\hat{y} = [\delta^T, \theta_{\Delta}^T]^T$. From the time-update stage of the Kalman filter, an improved orientation prediction can be obtained from $R(\theta_{I_k}^-) = R(\theta_{E_k}) \times R(\theta_{\Delta_k}^-)$. An updated measurement z_k is given by $z_k = [z_{x_k}^T, z_{\theta_k}^T]^T$, where z_x is the position error and z_{θ} is the orientation error expressed as Euler angles. The rotational error z_{θ} is measured from $R(z_{\theta_k}) = R(\theta_{E_k})^{-1} \times R(\theta_{I_k})$. While the Kalman filter is effective at tracking changes in orientation using Euler angles, care must be taken to avoid angle rollover, which occurs at either $\pm 180^\circ$, using instead, a continuous expression of orientation.

Algorithm 1 General hybrid tracking strategy

for each frame k :

1. Calculate \tilde{x}_{E_k} from the EMT sensor using equations 8.4 and 8.5.
 2. Update the prediction $\tilde{x}_{I_k}^-$ from the time - update prediction equations from 8.9.
 3. Compute the refined estimate \tilde{x}_{I_k} from CT-video registration.
 4. Calculate the measured error z_k and perform update correction using 8.10.
-

8.4 Respiratory Motion Compensation

Respiratory motion has been frequently discussed as a potential limitation in bronchoscopic navigation and studies vary in the degree to which this limitation is addressed. Means of overcoming deformation due to respiratory motion have been explored. Mori *et al.* simulated respiratory motion within a rigid phantom by adding a sinusoidal offset to the EMT sensor position and showed that a hybrid tracking was still effective [96]. Wegner *et al.* implemented a centerline matching technique that projected each EMT position to the nearest centerline path within the current branch being navigated during bronchoscopy within an excised sheep lung [156]. Later, this group adopted a particle filter approach to

improve localization within a purely simulated bronchoscopic framework [157].

An alternative approach uses externally position sensors as a surrogate for internal motion. Wong *et al.* demonstrated that an EMT position sensor could predict internal organ motion to within 1 mm [163]. Timinger *et al.* used an affine transformation to account for respiration during navigation of the heart using EMT [149]. Solomon *et al.* noted that respiratory motion was the foremost contributor to localization error using an EMT system within airways of a real patient [131]. After compensation for motion using an externally mounted position sensor, localization errors were reported around 2-3 mm within the central airways. Deligianni *et al.* modeled respiratory using active shape models derived from multiple CT scans acquired over a respiratory cycle [23].

These methods, however, are somewhat limited in their approaches to navigation. First, in many cases respiration is merely simulated, which does not adequately mimic the more complex motions observed by both the sensor and bronchoscopic video. Furthermore, these techniques are typically limited to the more central lung due to the use of larger conventional bronchoscopes. Within the peripheral airways, localization is challenged both by larger respiratory excursions and airways that are more closely aligned, allowing for potential misregistration of the scope to an incorrect airway. In the work by Deligianni *et al.* a more sophisticated and comprehensive motion model is employed, but due to the need for repeated CT scanning, may not be clinically feasible. Respiratory motion models using deformable registration of CT images may further prove insufficient for the reason that deformation may change due to patient orientation or the physical presence of the scope within the airways.

In this work, the model presented from equation 8.4 is limited by its assumption that the registration error is slowly varying in time. When considering the effect of respiratory motion, the registration error can be differentiated into two components: a slowly varying error offset λ and an oscillatory component that is dependent on the respiratory phase ϕ , where ϕ varies from 1 at full inspiration and -1 at full expiration (Figure 8.6). Therefore, the model was extended to include respiratory motion compensation (RMC), given by the

form:

$$\mathbf{x}_{I_k} = \mathbf{x}_{E_k} + \lambda_k + \phi_k U_k \quad (8.12)$$

In this model, λ represents a slowly varying secular error between the EMT system and the zero-phase or “average” airway shape at $\phi = 0$. The process variable U is the maximum local deformation between the zero-phase and full inspiration ($\phi = 1$) or expiration ($\phi = -1$) at $\tilde{\mathbf{x}}_{I_k}$. From Chapter 6, deformable registration of chest CT images taken at various static lung pressures showed that the respiratory-induced deformation of a point in the lung roughly scales linearly with the respiratory phase between full inspiration and full expiration[133]. Instead of computing ϕ from static lung pressures, as done previously, an abdominal-mounted position sensor serves a surrogate measure of respiratory phase.

With the new RMC model, Kalman variables are altered to reflect equation 8.12. The process state is revised to the state: $\hat{\mathbf{y}} = [\lambda^T, \theta_{\Delta}^T, U^T]^T$. The predicted position is subsequently changed to $\mathbf{x}_{I_k}^- = \mathbf{x}_{E_k} + \lambda_k^- + \phi_k \cdot U_k^-$. From the measurement update equations, H is updated at each new frame to include the current measurement of ϕ such that:

$$H = \begin{bmatrix} I_3 & 0 & \phi \cdot I_3 \\ 0 & I_3 & 0 \end{bmatrix}$$

where each element is a 3×3 matrix and I_3 is identity.

8.4.1 Computing Respiratory Phase

Three EMT sensors were affixed to the animal during bronchoscopic examination (Figure 8.7a). One sensor was placed on the sternum to track gross movement or shifting while the abdominal sensors were used for tracking respiratory phase. To monitor respiratory phase, the z -axis displacement of an abdominal sensor was used. The respiratory phase ϕ was calculated by remapping the sensor signal to within a range of -1 to 1. To account for variation in deformation and drift, ϕ was computed as a fractional (negative or positive) displacement of the average of the previous two breath cycles. This can be expressed

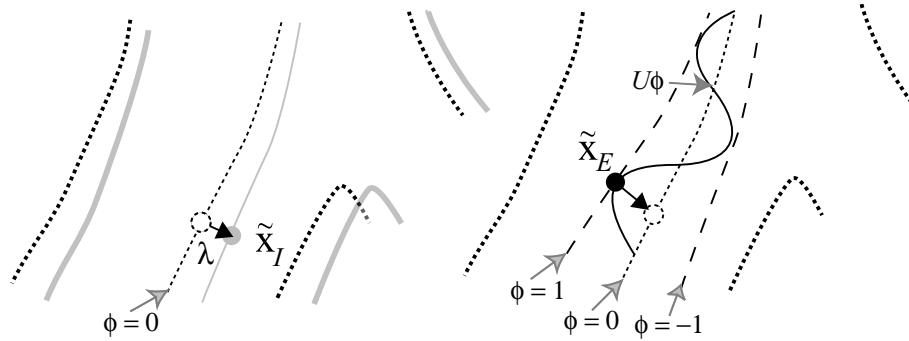


Figure 8.6: Hybrid tracking strategy using respiratory motion compensation. The position disagreement between x_{E_k} (black trace) and x_{I_k} (gray trace) was modeled by two components, including a zero-phase (black dash) offset λ (left) and a higher frequency phase-dependent component $U\phi$ (right).

mathematically as:

$$\phi_{i,k} = \frac{z_k - z_{i-1}^{\min}}{z_{i-1}^{\max} - z_{i-1}^{\min}} + \frac{z_k - z_{i-2}^{\min}}{z_{i-2}^{\max} - z_{i-2}^{\min}} - 1$$

where i denotes the i th respiratory cycle over which the maximum and minimum values are given by z_i^{\max} and z_i^{\min} , respectively.

8.4.2 Results

To evaluate the hybrid tracking algorithms, results were compared to that of independent EMT and IBT in four separate bronchoscopic sessions. Tracking results are depicted in Figures 8.8 and 8.9 for EMT, IBT, and hybrid strategies using both the 3D (position only) and 6D (positional and rotational) correction terms. Figures 8.10 and 8.11 depict the tracking results of hybrid tracking both with and without RMC. Tracking results obtained from the simulations were heavily dependent on the measurement and process errors, v and w . Using the 3D and 6D tracking methods,

For initial evaluation, tracking accuracy was assessed on the basis of the RMS localization error E^{key} between each of the tracking scenarios and the manually registered key frames. The positional tracking error was over 14 mm for independent EMT and IBT of

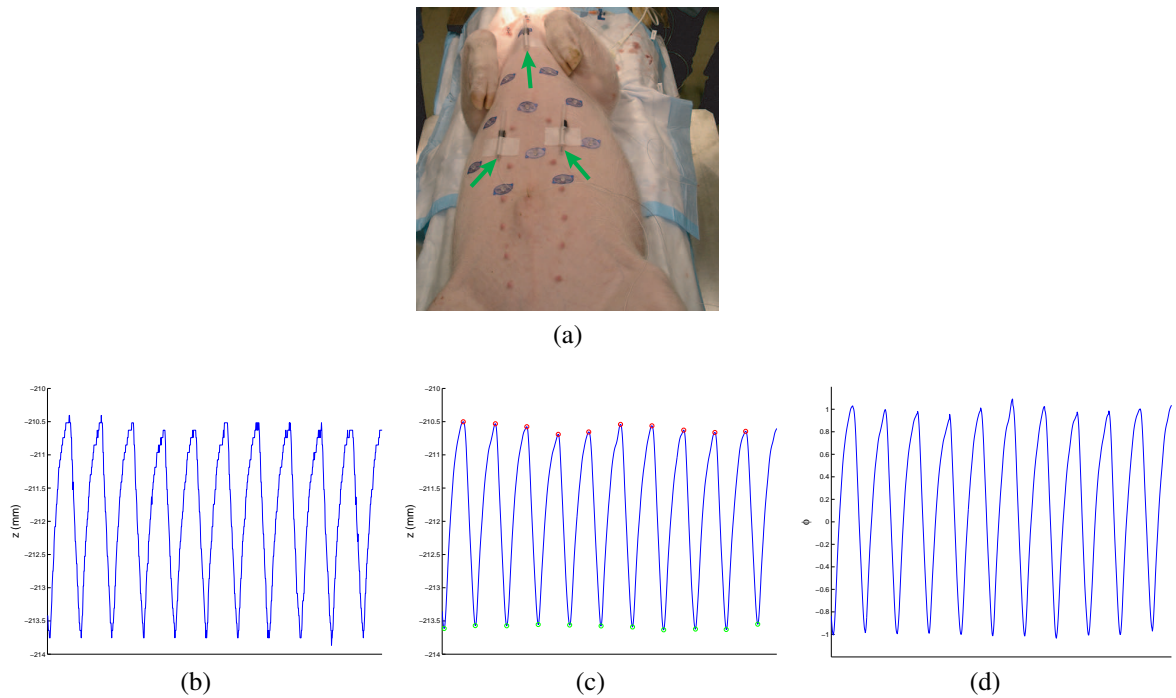


Figure 8.7: Computing respiratory phase ϕ from an externally mounted position sensor. A sensor were placed on the sternum and two placed on the abdomen indicated by *green arrows* (a). The displacement of one of the abdominal sensors in the z -axis was used as the phase input signal (b). The signal was smoothed and the position peaks were detected at full inspiration (*red dots*) and full expiration (*green dots*) (c). The signal was then normalized to a value ϕ expressed as a fraction of the peak and trough values observed during the previous two breath cycles (d).

the SFE averaged over all frames. The error $E_{\mathbf{x}}^{key}$ diminished to 6.74 mm, 4.20 mm, and 3.33 mm for 3D, 6D, and 6D+RMC hybrid tracking strategies, respectively. The orientational error E_{θ}^{key} was 14.30° , 11.90° , and 10.01° for 3D, 6D, and 6D+RMC, respectively. From Figures 8.10 and 8.11, hybrid tracking appears to follow the same 6D path, however, with RMC, tracking is far less erratic. Tracking noise was quantified by computing the average interframe motion $\Delta\tilde{\mathbf{x}}$ between subsequent localizations at $\tilde{\mathbf{x}}_{I_{k-1}}$ and $\tilde{\mathbf{x}}_{I_k}$. Average interframe motion $\Delta\tilde{\mathbf{x}}$ was 4.53 mm and 10.94° for 3D, 3.33 mm and 10.95° for 6D, and 2.37 mm and 8.46° for 6D+RMC.

To eliminate the subjectivity inherent in manual registration, prediction error E^{pred} was computed as the average per-frame error between the predicted position and pose, $\tilde{\mathbf{x}}_{I_k}^-$ and

the measured position $\tilde{\mathbf{x}}_{I_k}$. The positional prediction error $E_{\mathbf{x}}^{pred}$ was 4.82 mm, 3.92 mm, and 1.96 mm for 3D, 6D, and 6D+RMC embodiments, respectively. The orientational prediction error E_{θ}^{pred} was 18.64°, 9.44° and 8.20° for 3D, 6D, and 6D+RMC embodiments, respectively. Figure 8.12 depicts the z -axis tracking results for each of the hybrid methods within a peripheral region of session 4. For each plot, the tracked position is compared to the predicted position and key frames spaced every 4 frames. In the 3D hybrid method, prediction error results in divergent tracking. In the 6D method, the addition of orientation improves tracking accuracy, though prediction error is still large, as δ does not react quickly to the positional error introduced by respiration. With the inclusion of RMC, the tracking accuracy is modestly improved, though the predicted position more closely follows the tracked motion. The z -component was selected because it was the axis along which motion was most predominant. Figure 8.13 shows registered real and virtual bronchoscopic views at selected frames using all three methods.

From the proposed hybrid models, the error terms in $\hat{\mathbf{y}}$ are considered to be locally consistent and physically meaningful, suggesting that these values are not expected to change dramatically over a small change in position. Provided this is true, $\tilde{\mathbf{x}}_{I_k}$ at each frame should be relatively consistent with a blind prediction of the SFE position and pose computed from $\hat{\mathbf{y}}_{k-\tau}$, at some small time in the past. Formally, the blind prediction error for position can be computed as:

$$E_{\mathbf{x}_k}^{blind}(\tau) = \begin{cases} \|\mathbf{x}_{I_k} - (\mathbf{x}_{E_k} + \delta_{k-\tau})\| & \text{no RMC} \\ \|\mathbf{x}_{I_k} - (\mathbf{x}_{E_k} + \lambda_{k-\tau} + \phi_k U_{k-\tau})\| & \text{w/ RMC} \end{cases}$$

and

$$E_{\theta}^{blind}(\tau) = \arccos(\text{tr}(R(\theta_{I_k}) \times [R(\theta_{E_k}) \times R(\theta_{\Delta_{k-\tau}})]^{-1}) - 1)$$

For time a time lapse of $\tau \sim 1$ second, $E_{\mathbf{x}}^{blind}$ was 4.53 mm, 3.33 mm, and 2.37 mm for 3D, 6D, and 6D+RMC tracking methods, respectively. The rotational error E_{θ}^{blind} was

22.61°, 17.83°, and 16.65° for 3D, 6D, and 6D+RMC tracking methods, respectively.

Table 8.2: Average statistics for each of the SFE tracking methodologies. Error metrics E^{key} , E^{pred} , E^{blind} and $\Delta\tilde{x}$ are given as RMS position and orientation errors over all frames. The mean number of optimizer iterations and associated execution times are listed for CT-video registration under each approach.

	EMT	IBT	hybrid(3D)	hybrid(6D)	hybrid(6D+RMC)
E^{key} (mm/°)	14.22 18.52°	14.92 51.30°	6.74 14.30°	4.20 11.90°	3.33 10.01°
E^{pred} (mm/°)	—	—	4.82 18.64°	3.92 9.44°	1.96 8.20°
E^{blind} (mm/°)	—	—	5.12 22.61°	4.17 17.83°	2.73 16.65°
$\Delta\tilde{x}$ (mm/°)	—	1.52 7.53°	4.53 10.94°	3.33 10.95°	2.37 8.46°
# iter.	—	109.3	157.1	138.5	121.9
time (s)	—	1.92	2.61	2.48	2.15

The hybrid RMC model produces an estimate of the local and position-dependent airway deformation, $U = U(\mathbf{x}^{CT})$. Unlike the secular position and orientation errors, δ and θ , U is assumed to be a physiological measurement, and therefore independent of the registration. For comparison, the computed deformation was also independently measured through deformable image registration of two CT images taken at full inspiration and full expiration (lung pressures of 22 and 6 cmH₂O, respectively)[133]. From this process, a 3D deformation field \vec{U} was calculated, describing the maximum displacement of each part of the lung during respiration. Fig. 8.14 compares the maximum deformation approximated by the Kalman filter, $U(\mathbf{x}^{CT})$, over every frame of the first bronchoscopic session to that calculated from the deformation field, $\vec{U}(\mathbf{x}^{CT})$. The maximum displacement values at each frame U_k and \vec{U}_k represent the respiratory-induced motion of the airways at each

point in the tracked path \mathbf{x}^{CT} from the trachea to the peripheral airways. As evident from the graphs, deformation is most predominant in the z -axis and in peripheral airways where displacements of ± 5 mm z -axis were observed.

8.5 Conclusions

Our results show that the hybrid approach provides a more stable and accurate means of localizing the SFE intraoperatively. The positional tracking error E_x^{key} for EMT and IBT was 14.22 mm and 14.92 mm, respectively, as compared to 6.74 mm in the simplest hybrid approach. Moreover, E_x^{key} reduced by at least two-fold from the addition of orientation and RMC to the process model. After introducing the rotational correction, the predicted orientation error E_θ^{pred} , reduced from 18.64° to 9.44° . RMC likewise reduced the predicted position error E_x^{pred} from 3.92 mm to 1.96 mm and the blind prediction error E_x^{blind} from 4.17 mm to 2.73 mm. These improved prediction estimates are reflected by reduced computation time in Table 8.2. With the 6D+RMC tracking approach, the number of optimizer iterations was reduced as well as the computation time (from 2.61 s to 2.15 s). Though performance of the hybrid system could be directly compared the commercially available, EMT-based superDimension system, we believe that bronchoscopic tracking is greatly advantaged by the use of IBT, not only for improved accuracy, but for direct visualization of pathology at the point of biopsy.

Using RMC, the Kalman error model managed to more accurately predict SFE motion, particularly in peripheral lung regions that are subject to large respiratory excursions. From Fig. 8.14, the maximum deformation, U , estimated by the Kalman filter was around ± 5 mm in the z -axis, or 10 mm in total, which agrees well with the deformation computed from nonrigid registration of CT images at full inspiration and full expiration. It is unknown, however, how displacement within the breathing lung compares with that, measured by deformable registration of images at static lung pressures. The more erratic estimate of U may reflect the localization error that is inherent in CT-video registration. However,

estimates of U may also be affected by the SFE itself, either by increasing airway rigidity or exerting forces which actively deform the airways. It is also admitted that presented results are from bronchoscopic examination of airways in the lower lung, as they are accessible to the SFE without steering. In patients, however, a large number of nodules occur in the upper lung where deformation is smaller, suggesting that the tracking errors reported here are potentially exaggerated compared to other regions. Deformation due to cardiac motion was not addressed in this study, though there was no perceived effect. However, by monitoring cardiac phase, addition of a similar displacement term would be feasible to account for such motion.

Accurate tracking is further limited by measurement of respiratory phase, ϕ , from the abdominal sensor. This is only a surrogate measure of ϕ , as not all regions of the lung can be assumed to move in phase. Respiratory phase was certainly more tractable using a ventilator than would be in a clinical setting. Changes in depth of respiration or coughing would certainly disrupt phase measurements, if only momentarily. It is also unknown how these issues might manifest in a diseased lung, where motion may be more atypical.

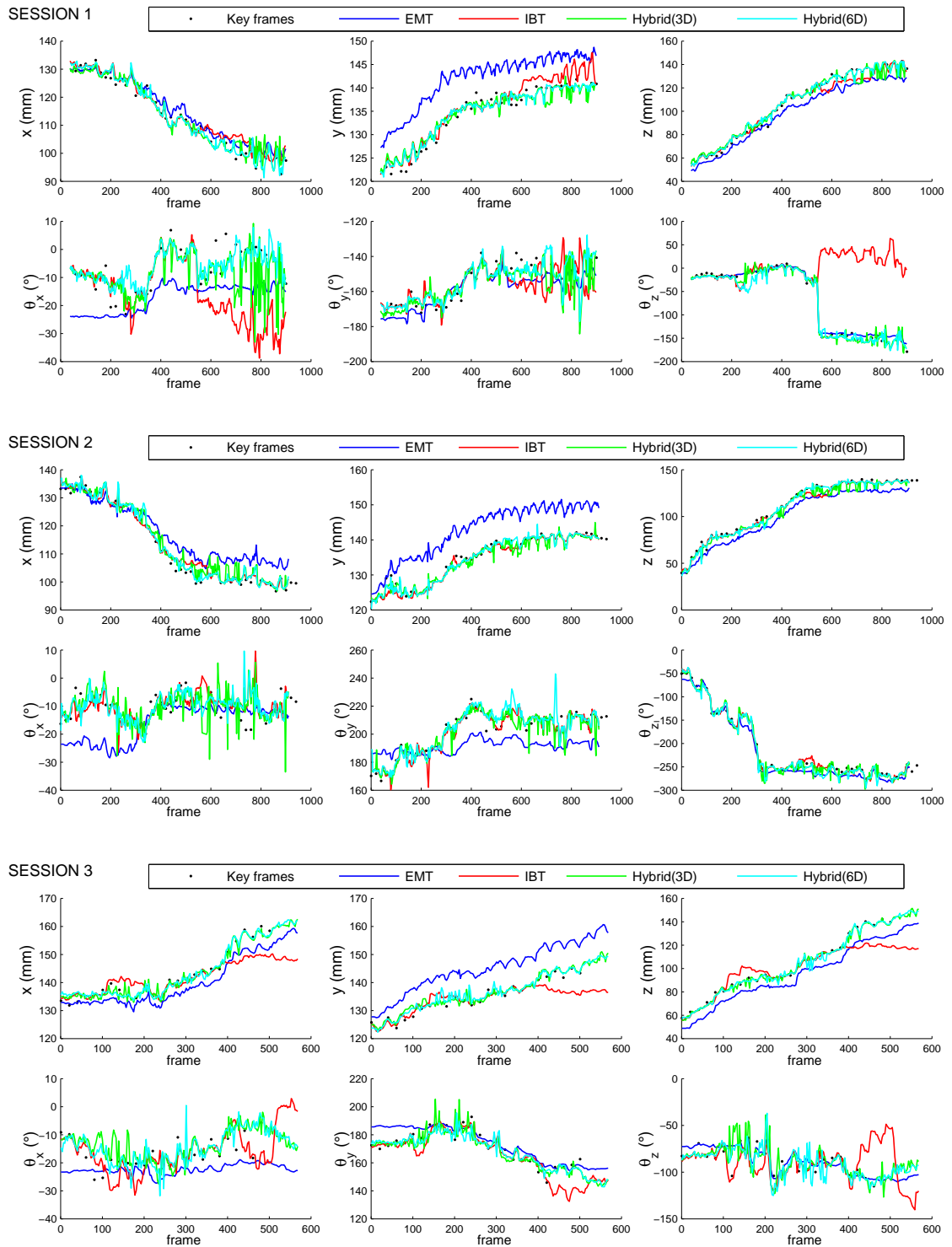


Figure 8.8: Hybrid tracking results compared to independent EMT and IBT for sessions 1-3

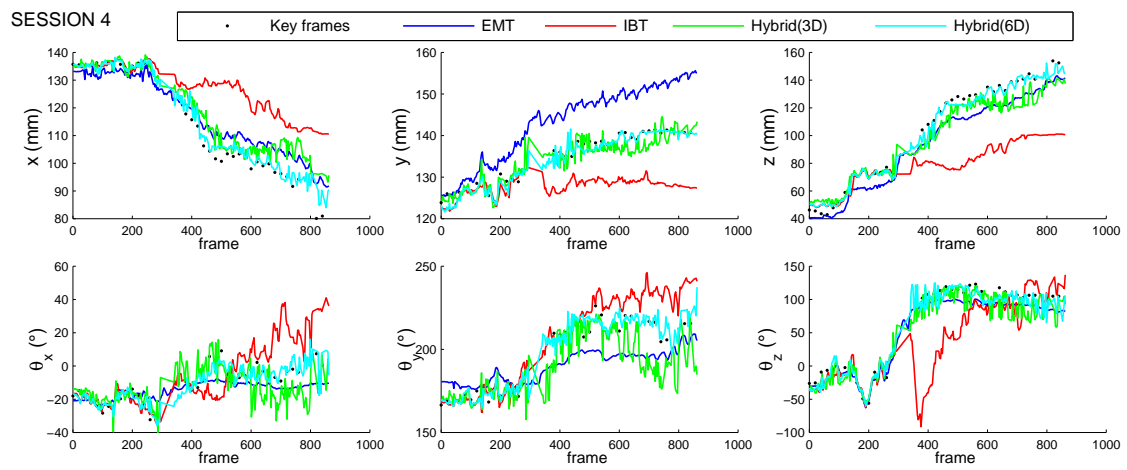


Figure 8.9: Hybrid tracking results compared to independent EMT and IBT for session 4

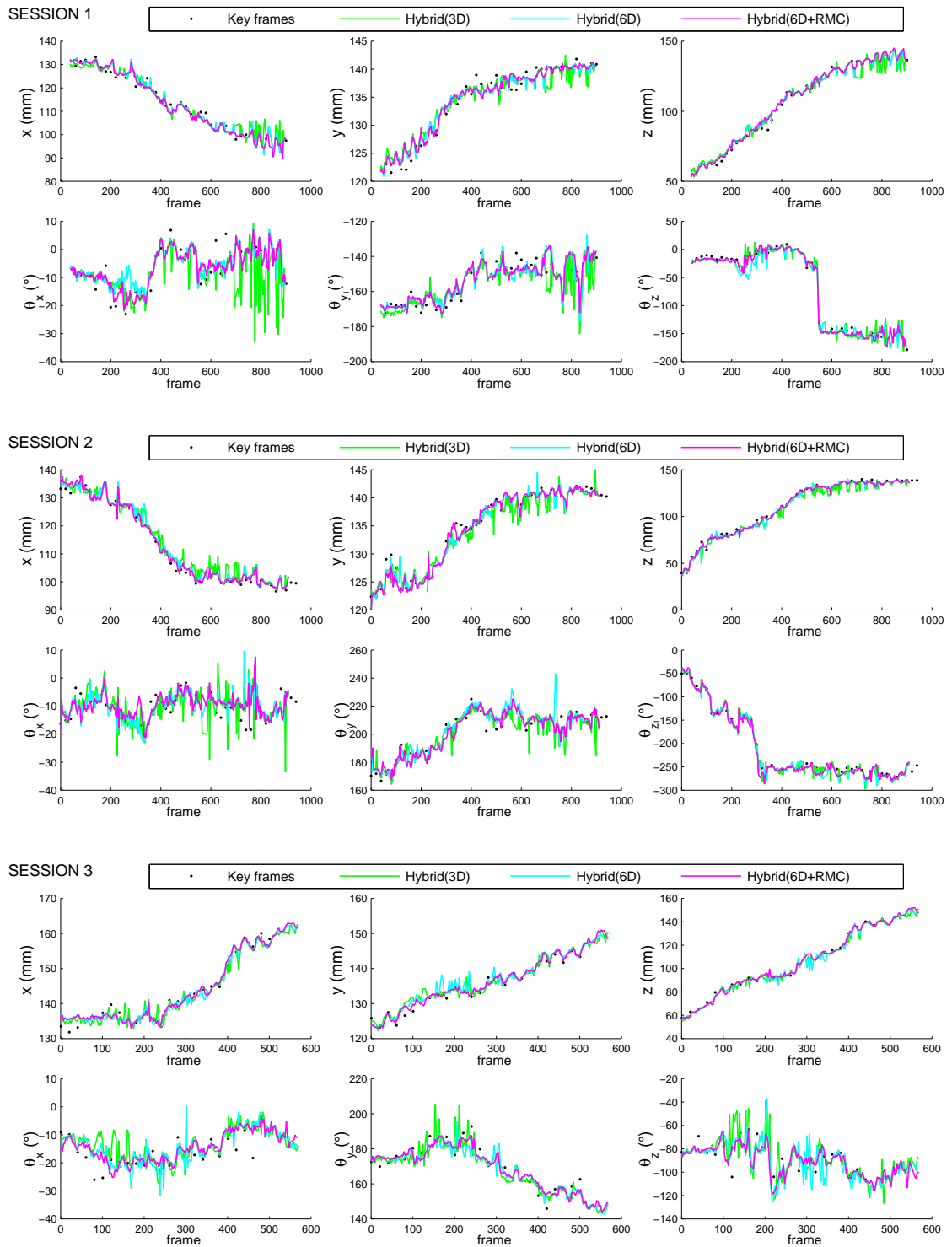


Figure 8.10: Hybrid tracking results with and without RMC for sessions 1-3

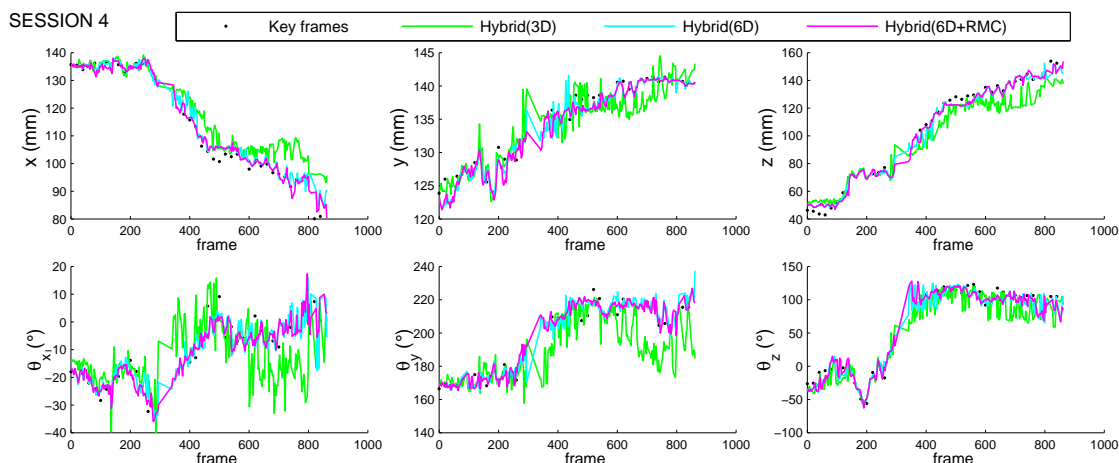


Figure 8.11: Hybrid tracking results with and without RMC for session 4

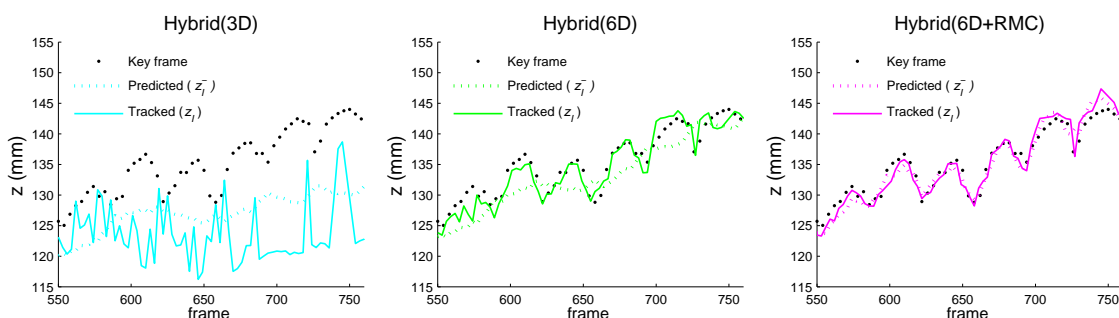


Figure 8.12: Hybrid z -axis tracking results are plotted over frames at the end of session 4 within peripheral airways using all three methods. Key frames (*black dots*) were manually registered at four frame intervals. For each method, the predicted z position, $z_{I_k}^-$ (*dotted line*) is plotted along with the tracked position z_{I_k} (*solid line*). Using the 3D offset method, tracking deviated from the true SFE path. In the 6D version, the plotted position of the scope follows the true SFE path, though the prediction does not adapt to respiratory motion. Using RMC, the predicted and tracked positions are in close agreement,

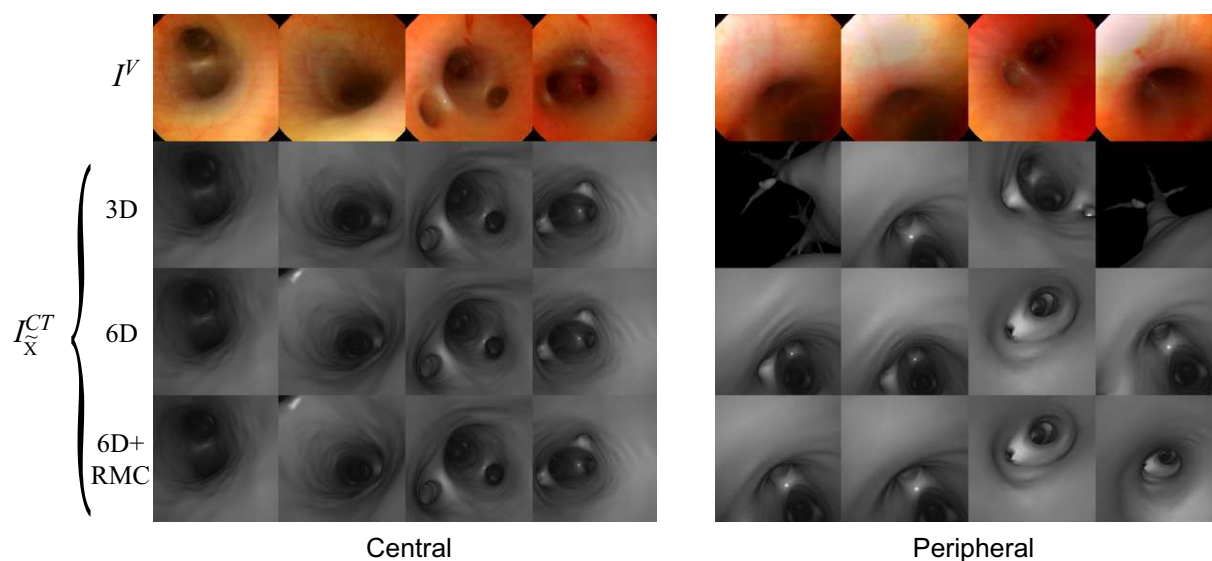


Figure 8.13: Selected frames illustrate the localization accuracy using each of the hybrid tracking methods. Tracking accuracy is somewhat more comparable in the central airways as represented by the right four frames. In the more peripheral airways (left four frames), the positional offset model could not reconcile the prediction error, resulting in frames that fall outside the airways altogether. Once orientation was added, tracking stabilizes, though respiratory motion at full inspiration or full expiration was observed to cause misregistration. With RMC, smaller prediction errors resulted in more accurate tracking.

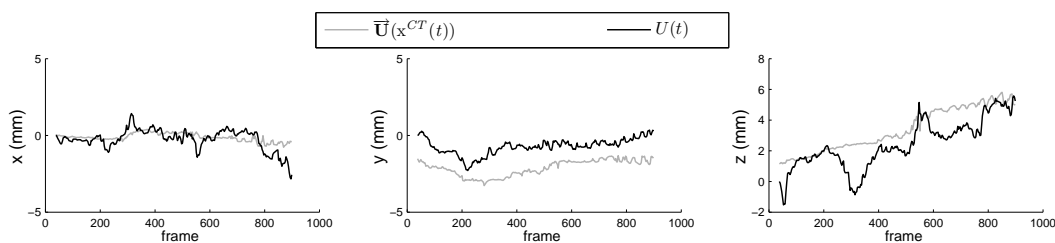


Figure 8.14: Comparison of the airway deformation U computed from the Kalman filter and the deformation $\vec{U}_{max}(x_I)$ acquired from deformable registration of CT images over the SFE path.

Chapter 9

CONCLUSIONS AND FUTURE WORK

The focus of this dissertation research was the design, construction, and testing of a bronchoscopic guidance system for navigation into peripheral airways. Development and testing of the navigation system for guided SFE was progressed in three arenas. First, software elements were created for the extraction and virtual visualization of the airway anatomy and a utility was constructed to permit preoperative planning for an SFE procedure [2]. Second, the potential for accurate tracking of the SFE into peripheral lung regions using EMT was evaluated through quantitative assessment of airway deformation using nonrigid registration of CT images [133]. Third, conventional tracking methods were tested and validated during bronchoscopy in a live pig [135, 134]. This included electromagnetic and image-based tracking technologies. A novel hybrid approach demonstrated improved localization of the SFE within peripheral lung regions, which undergo relatively large respiratory deformations. In this chapter, I detail the specific accomplishments of this dissertation, present my conclusions of this research, and outline the critical next steps in translation of this technology to clinical use.

In Chapter 3 software was produced to segment the airway regions of a chest CT, generate a virtual surface model of the airways, and the airway centerlines. Segmentation of the airways was achieved using a modified version of the method used by Kiraly *et al.* [74], which involved region growing and mathematical morphology. Morphological filtering was performed in this work for large and small airways separately to reduce run times. With the isotropic image resolutions used, morphological filtering was conducted in all three image planes, resulting in more extensive segmentation results. A virtual surface

mesh model was generated from the airways using templated code found within VTK software. Medial axis thinning was also developed in-house to compute a centerline model of the airways. In Chapter 4, a preoperative planning utility was effective for defining a path to a target lesion using the centerline model. The interface permitted visualization of the CT image in each image plane to locate a lesion and establish a target region that can be seen during bronchoscopy. The software was further equipped with a number of editing tools for manual segmentation of missed airway branches and path extension.

As part of the evaluation for potential EMT of the SFE during bronchoscopy, a study of respiratory induced airway deformation was conducted in Chapter 6. First, a framework was successfully developed for deformable registration of CT images using the demons algorithm. Accuracy of the deformable registration was found to be reliant on an initial histogram matching (to account for lung volume changes), and the degree of field smoothing. A new gradient-weighted variation of the demons algorithm was proposed, which reduced the error of the registration. Interpolating airway deformation from the fractional lung pressure between full expiration and full inspiration proved to be a reasonable model of the true airway geometry. This finding served as the basis for later modeling of the deformation using a surrogate measure of respiratory phase from a abdominal sensor.

The large deformations (10-20 mm) observed in the lung discouraged future use of the EMT as a sole tracking source during bronchoscopy. Therefore, an alternative image-based tracking method was investigated by matching virtual bronchoscopic perspectives to the real bronchoscopic video frames (Chapter 7). First, a free-hand calibration routine was established to model intrinsic imaging properties of the SFE and remove radial distortion of the images. A number of video preprocessing stages were also discovered to be crucial to accurate CT-video registration. This included grayscale conversion, vignetting compensation, and image smoothing filters. From the SFE video images, IBT was tested using recorded bronchoscope within a live pig experiment. A similarity metric based alignment of surface gradients provided superior performance over other proposed methods. For SFE images, a gradient magnitude-weighted version of the metric resulted in the most robust

tracking solution with only 2 aberrant tracking instances observed over four sessions (2 frames out of 1,100).

Electromagnetic tracking (EMT) was combined with the image-based tracking configuration developed in Chapter 7 to produce a hybrid tracking strategy. The free-hand calibration technique was successfully expanded to register the EMT coordinate system to the SFE image coordinate system prior to bronchoscopy, resulting in small disagreement between image-based and sensor-based SFE localization. In the hybrid tracking approach, an error-state Kalman filter was used to adaptively estimate the local registration error between the real and virtual anatomies. Results showed improved tracking accuracy and resiliency to aberrant tracking. Inclusion of a rotational correction term further improved tracking accuracy. Respiratory motion was also adaptively modeled by using the Kalman filter and a measure of the respiratory phase from a sensor attached to the animal's abdomen. Compensation of respiratory motion resulted in minimal tracking error with regard to the true SFE path, and provided the best estimate of the SFE position prior to CT-video registration. With RMC tracking error reduced by approximately two-fold in each category compared to the 3D hybrid model. Finally, intraoperative guidance was effectively simulated by overlaying a virtual path to a target site onto the bronchoscopic video with a display of the SFE position relative to the airway or on the CT scan itself.

9.1 Future Work

The guidance system has demonstrated effective simulated tracking and display of the SFE position for virtual navigation in a live pig study. However, translation of the technology to clinical use requires several advancements in the design of the hardware, software, and clinical aspects of the system. The most critical challenges are the acceleration of the tracking algorithm to permit real-time guidance, and the incorporation of a steering mechanism to allow manual manipulation of the scope into more peripheral regions, including the upper airways. Within the near future, a radically smaller 5DoF EMT sensor will be incorporated

into the system to further miniaturize the tracked distal tip. A number of other optimizations are more immediately feasible such as more accurate distortion correction of SFE images and an automated global registration of real and virtual anatomies prior to bronchoscopy.

9.1.1 Image Analysis and Path-Planning Software

The image analysis and interface software developed in this dissertation was developed completely in-house with minimal use of some open-source toolkits. Several facets of the software project, though deemed appropriate for the scope of this dissertation, would benefit from more extensive research and refinement with regard to areas such as image segmentation, surface extraction, centerline analysis, and user interaction. Currently, segmentation is limited within peripheral airways and does not reach into many of the regions. More advanced segmentation schemes, such as that proposed by Graham *et al.* [42] present avenues for advancement, though it is unknown what benefit would be realized from more sophisticated algorithms with regard to the number of additional peripheral branches detected. Such research efforts, however, require larger scale collaborations to acquire the necessary number of data sets and clinician time for training of a robust airway classifier. Improved segmentation and path-planning may be achieved through semi-automatic means. In the work of Gibbs *et al.* [37], enhanced manual segmentation of small peripheral airways, not identified by automated segmentation, were easily added using the live-wire method [85]. Semi-automated approaches offer potential advantages in that it offers the user a means of compensating for local inadequacies in the automated segmentation as part of a procedural planning session.

Future tracking in the peripheral airways is also currently limited by the resolution of the airway surface model. Small airways, only one or a couple voxels in diameter, are represented by a blocky surface mesh that will hinder CT-video registration. The constructed surface of small peripheral airways, as depicted in Figure 8.13, suffer holes, narrowing, or pinching, which result from inadequate segmentation in these branches or over-smoothing of the surface. Improved methods of generating realistic mesh models of airways at this size

should be investigated further. Gibbs *et al.* developed a variable-HU isosurfacing function based on topological dilation of small airways, which resulted in fewer ill-defined or missing airways [37]. Geiger *et al.* used virtual angioscopic images through pulmonary arteries as a surrogate for small airways [34]. Because CT resolution of the bright pulmonary arteries is much better than that of small airways, and because each airway is closely accompanied by such an artery, guidance by virtual angioscopy may provide anatomical perspectives quite equivalent to those generated from virtual bronchoscopy.

9.1.2 Real Time Tracking

The computation time for CT-video registration is currently the main limitation in the advancement toward live bronchoscopic guidance. The average per-frame processing speed of 2.15 s (Table 8.2) is not sufficient for real time tracking. The work of this dissertation has primarily focused on overall feasibility of bronchoscopic guidance, but requires dramatic increase in the overall computational speed. Real time tracking would not only provide a means of live guidance, but would also allow for more rapid validation of algorithms during offline simulation. Though optimizations to the code alone are unlikely to achieve the necessary processing speeds for real time use, such improvements would be helpful.

The present system utilizes VTK libraries for streamlined processing of image data using multithreaded classes, which provided templates for developing custom software. While this provided a robust and reliable test platform for simulated tracking, speed improvements may be realized by altering the software or modifying the means by which image data is streamed through the processing pipeline. This might include a more efficient filtering algorithms, or eliminating unnecessary operations. One such example might be to reduce the image sizes being used prior to computational analysis. Larger scale changes would include abandonment of the toolkit altogether. Because application development is largely peripheral to the scope of this project and somewhat beyond my level of programming experience, further professional consultation or development may be merited.

Design and incorporation of the registration algorithms are also relevant to speed per-

formance. A comprehensive analysis of different optimizers for 2D/3D image registration, as performed by Helferty *et al.* [50], may indicate other methods are superior with regard to execution time or number of iterations necessary. Optimization of the registration parameters in the current system may also reduce computation time. For instance, the number of CT-video registration iterations is set to a maximum of 100 and a minimum step size of 0.1 mm in Cartesian coordinates and a 5° change in Euler orientation angles. For the simulations conducted in this work, the bounding box of the registration search space was limited to 10 mm in each direction and a change in orientation of 20°. Improved localization accuracy, as shown using the hybrid tracking strategy with RMC, reduces the necessary search space for CT-video registration. However, while decreasing the number of registration iterations search space size, or search space resolution may increase processing speed, the potential trade-off in tracking accuracy should be carefully weighed. Other optimizations may similarly be achieved by reducing the size of the video and virtual images, computing similarity from subsampled regions, modifying the similarity metric, or simply tracking at a lower frame frequency. The progression of the guidance system should more thoroughly evaluate the impact of these potential changes using a number of bronchoscopic sessions.

Ultimately, it is anticipated that real time tracking will require more substantive changes in the current CT-video registration algorithm or computer hardware. In the work of Merritt *et al.* live guidance was achieved through a gradient-based registration optimizer that resulted in a per-frame processing time of $\frac{1}{15}$ th of second [93]. Using this approach, similarity between real and virtual bronchoscopic images were assessed, but correlation between subregions of the video and virtual images was used to instruct re-positioning of the virtual camera to rapidly converge to an optimal solution. Unlike the more brute-force search space method used in this dissertation, the gradient-based optimizer uses only a small number of iterations during CT-video registration, and may be feasible for implementation in guidance of the SFE. Alternatively, changes to the hardware provide additional avenues for optimizing registration speed. In the work by Sugiura *et al.* accelerated matching speeds were achieved by performing rendering functions and image similarity calculations on a

dedicated multiprocessor GPU [138]. For future live guidance using the SFE, a new workstation including a high-end multi-processor GPU that takes advantage of C-based parallel computing architecture (CUDA) could be considered for more rapid virtual image generation and registration to bronchoscopic video.

9.1.3 Intraoperative Guidance

Live guidance of the SFE will require future design of an intraoperative utility to direct steering the SFE through multiple airway generations to an established target. Postprocessing of a simulated tracking session are depicted in Figure 9.1. Guidance is provided in a four window GUI, which displays the bronchoscopic video, registered virtual image, global perspective, and position on a reconstructed CT slice. As an option, the route to a defined target is represented by a green path that is displayed in the virtual image, and overlaid onto the real bronchoscopic video for augmented guidance. This was achieved using a custom VTK filter to select the polygonal data of the path in the image buffer, and overlay the coordinates onto the video image data. A virtual model of the SFE displays its current position from an external perspective within the slightly transparent virtual model. Subsurface anatomy can likewise be identified on the CT slices where the SFE position is represented by the cross hairs.

To assist with guidance to peripheral lesions in the future, a number of intraoperative tools should be developed. First, visualization of subsurface anatomy from the virtual bronchoscopic perspective would allow the bronchoscopist to guide biopsy or needle insertion to a nodule that is not bronchoscopically visible. This would also help to prevent unintended puncture of arteries or the airway wall, which could cause excessive bleeding. In the work by Merritt, such considerations of work flow and usability by the bronchoscopist are considered for real time image-based guidance [92]. Finally, an intraoperative interface would promote digital annotation and storage of bronchoscopic guidance information that could later be reviewed and simulated for later reference or planning of future procedures.

9.1.4 Distortion correction

Clinical use of the SFE is still somewhat cumbersome as a result of the necessary calibration process. The SFE scanner dynamics, and hence the acquired video images, are sensitive to the environment and tend to change slightly over time. This requires some level of user manipulation of the scan parameters to optimize the scan path so that it is primarily circular and is not highly distorted. In this dissertation, camera calibration considered only the effects of radial lens distortion, and not the nonlinear distortions that arise from multiple variables that effect the central fiber's scan mechanics. These distortions are distracting to the bronchoscopist and may negatively impact CT-video registration.

A nonparametric distortion correction method was also devised as a means of eliminating such effects regardless of the scan path of the illumination fiber. This was not implemented as part of the tracking experiments performed in this work, but was shown to be effective for minimizing distortion present in images of a known target. With this technique, undistortion was achieved using a single calibration image acquired from the SFE a set distance from a target grid. Figure 9.2a shows the calibration setup. The SFE was inserted into a plastic chamber held a fixed distance from a mounted calibration grid such that the SFE was orthogonal to the plane of the target image. A dense grid of dots were printed onto a white background to comprise the test target. This was done to more thoroughly define the SFE distortion at each pixel position. Figure 9.2b is a sample image acquired by an SFE probe. The image contains radial lens distortion introduced by the lens, but a subtle 'S' curve in the grid rows is apparent and is related to errors in the estimated scan phase, and is more accentuated at the image center. Figure 9.2c illustrates the scan distortion of the SFE over the image plane.

First, the dense grid dots are located using the method described during the SFE calibration prescribed in section 7.2. To correct for this distortion, a thin-plate spline was used to rigorously define the displacement at each pixel as a weighted basis function of each grid dot located. By remapping the located grid positions to a uniform grid of arbitrary scale, an

undistorted image can be acquired as in Figure 9.2d. Figure 9.3 presents a series of sample images acquired by SFE probes with various degrees of distortion and the nonparametric corrections achieved using this method.

9.1.5 SFE Design

9.1.5.1 Integrated Steering Mechanism

An integrated steering/tip deflection mechanism is an essential design component for future use of the SFE within the airway tree. In particular, articulation of the distal tip is required to access side branching airways and negotiate the sharp branching angles leading into the upper airways. Another advantage of steering is the ability to keep the SFE tip off the endobronchial wall, producing less obscured video images as well as preventing fluid such as mucus or blood from contacting the front lens. Tip deflection also allows the user to sweep the tip across the airway wall as a means of dislodging mucus or fluid attached to the lens.

Although the tip-bending mechanism has not been solidified, initial design and testing of an articulation method has already been performed without drastically affecting the dimensions of the current SFE. Tip deflection is achieved by using the optical fibers themselves as tensile and compressive elements. During articulation, a handheld dual-axis lever is manipulated, thereby bending the distal tip by counter-balanced shortening and lengthening of axially paired collection fibers. Figure 9.4 shows the tip-bending achieved using the method described. However, the 90° deflection is produced under held tension. Passive deflection produces a more minimal degree of deflection that would still be advantageous. Other tip-bending designs, such as the use of small wires, will be investigated and will require future *in vivo* validation.

9.1.5.2 Incorporation of Ultrasmall EMT Sensors

A criticism of conventional ultrathin endoscopes and EBUS technologies is that they are relatively large, and preclude extension into peripheral airways. While the SFE is much smaller in size, the proposed hybrid tracking system requires an equivalently large EMT sensor to be piggy-backed onto the SFE, effectively doubling the diameter of the scope along one axis (Figure 8.1a). Though seemingly contradictory, the argument for electromagnetic tracking of a miniature endoscope is largely predicated on the use of even smaller miniature sensors that will likely be housed within the tip of future SFE probes.

Ascension Technology Corporation has recently developed an ultrasmall 5 DoF 0.30 mm sensor that is revolutionary for the field of minimally invasive procedures. Previously, the current smallest sensors are closer to or over 1 mm in diameter, which despite being small, limits tracking applications within small vessels. With these sensors, tracking can be accomplished with relatively no change to the SFE dimensions. Figure 9.5a displays the sensor and Figure 9.5b shows two configurations for 5 DoF and 6 DoF.

In the 5DoF configuration, the position and orientation of the sensor is tracked with the exception of the roll term, which specifies orientation along the sensor or SFE axis. To account for this, a 6 DoF tracked SFE can be configured by using two 5DoF sensors (Figure 13b). The roll can then be computed by differential position measurements of the two sensors approximately 1 mm apart. As a default, the 6 DoF configuration will be used for tests unless space requirements justify using the 5 DoF implementation.

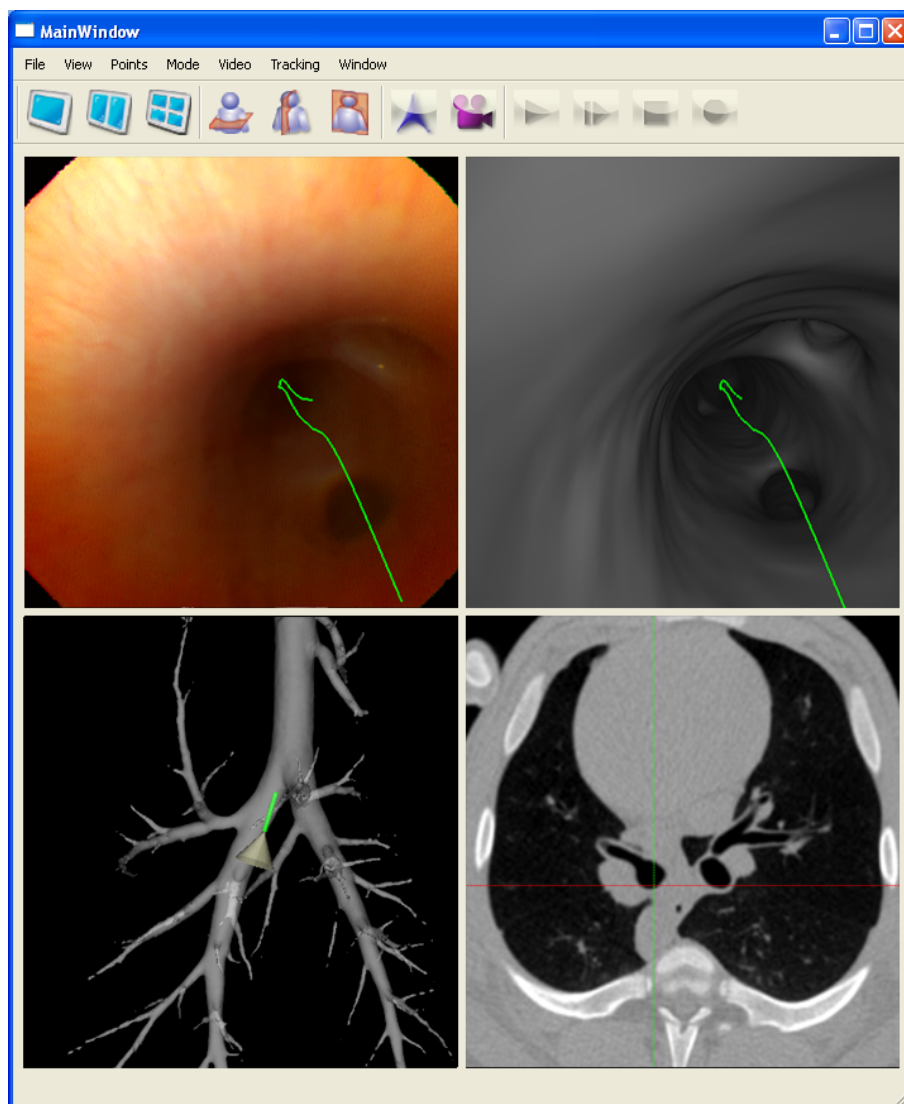


Figure 9.1: A simulated intraoperative guidance interface includes bronchoscopic video, virtual bronchoscopic perspective, and display of the SFE position on both a global virtual airway view and on the intersecting CT slice. A virtual path is used to navigate the SFE and is overlaid onto the bronchoscopic video for an augmented reality display.

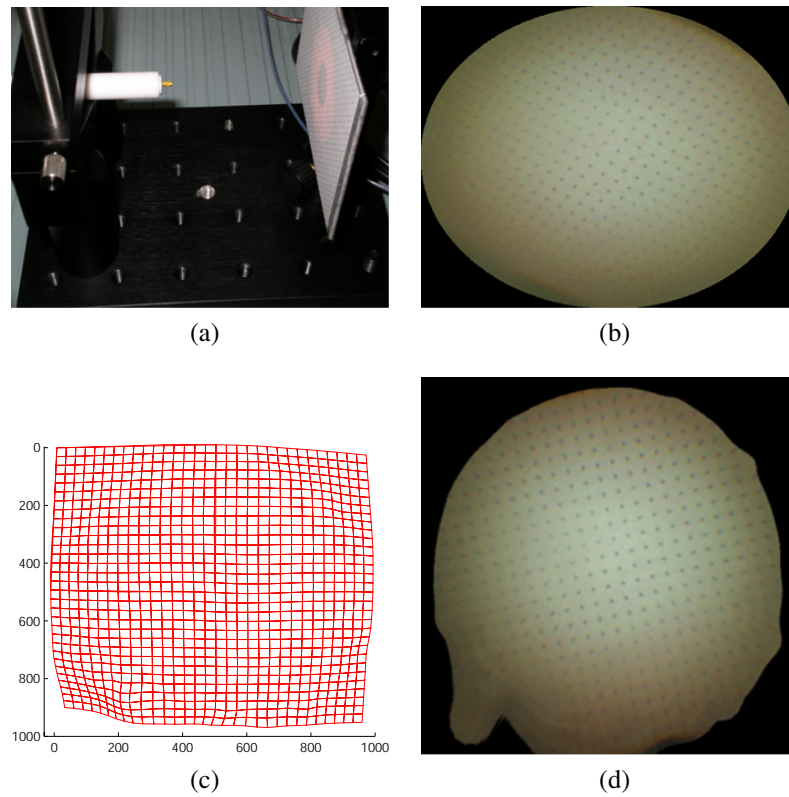


Figure 9.2: Nonparametric distortion correction procedure. The SFE is placed in a calibration jig so that the optical axis is orthogonal to the plane of the test grid (a). A simple calibration image is acquired (b), and the grid dots are automatically detected. A thin plate spline is used to model the distortion (c) of each point between the distorted and corrected images. The output is a corrected image of the grid with uniform spacing (d).

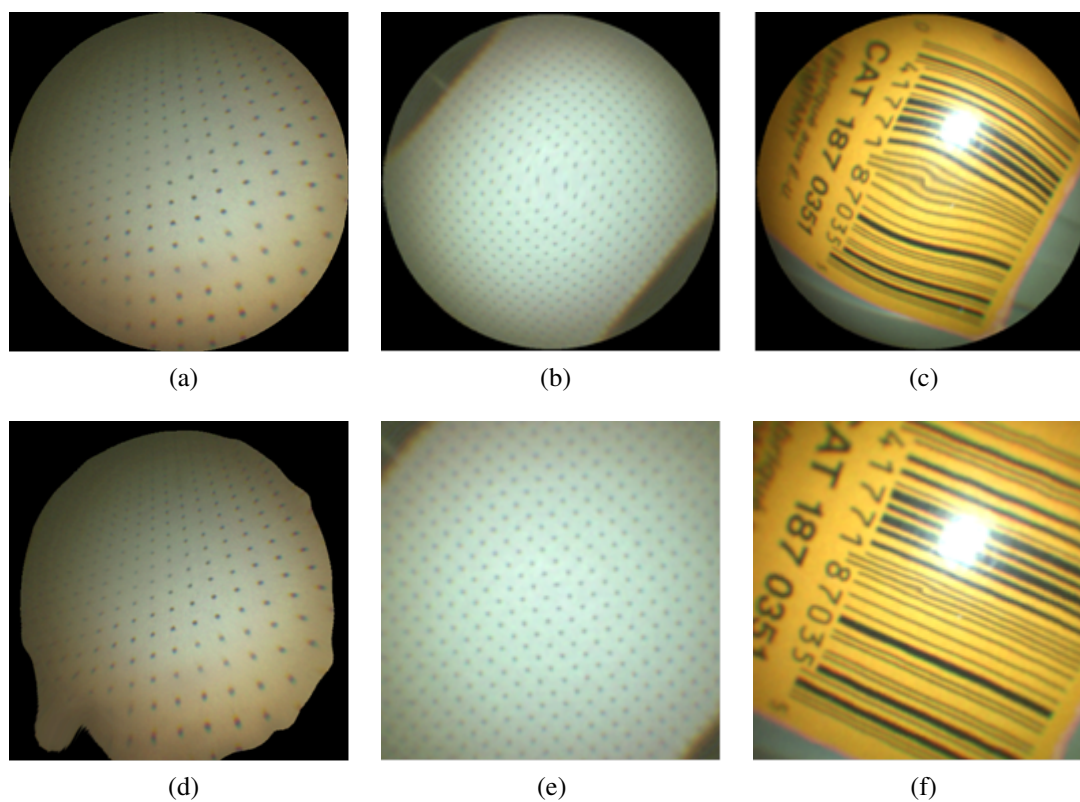


Figure 9.3: Example SFE images before and after nonparametric distortion correction. Images are paired column-wise. The first pair (a&d) are from an SFE probe that exhibits only a modest level of distortion. The remaining image pairs (b&e and c&f) are from an SFE probe with a more appreciable level of central scan distortion.

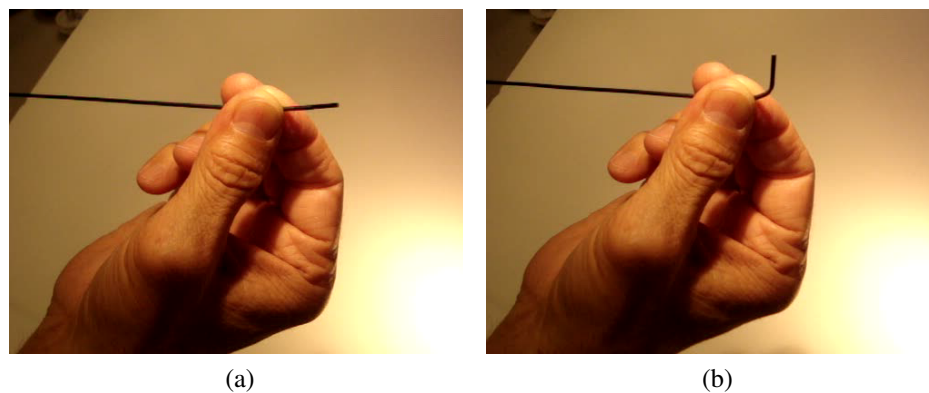


Figure 9.4: Demonstration of the first generation tip-bending mechanism.

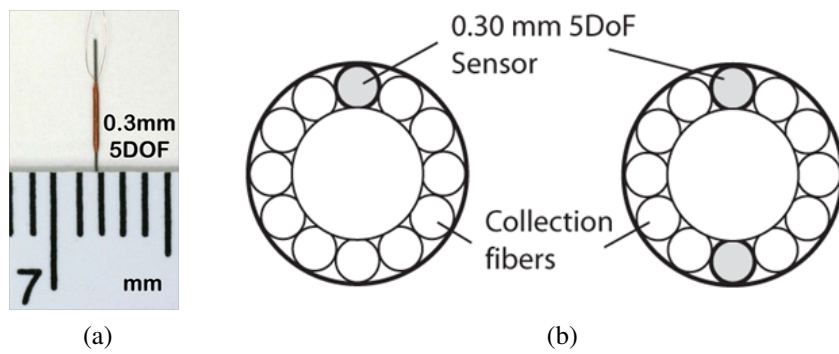


Figure 9.5: The new 0.30 mm 5 DoF Ascension sensor (a) will be integrated into the guided SFE design. By replacing a single fiber with a sensor a 5 DoF configuration is achieved (b-left), while two sensors can be used in a full 6 DoF configuration (b-right).

BIBLIOGRAPHY

- [1] F. Asano, Y. Matsuno, N. Shinagawa, K. Yamazaki, T. Suzuki, and H. Moriya. A virtual bronchoscopic navigation system for pulmonary peripheral lesions. *Chest*, 130:559–566, 2006.
- [2] I. Atmosukarto, T. D. Soper, R. W. Glenny, E. J. Seibel, and L. G. Shapiro. An interactive 3D user interface for guided bronchoscopy. In *Medical Imaging 2007: Visualization and Image-Guided Procedures*, volume 6509, San Diego, CA, USA, 2007.
- [3] D. Aykac, E.A. Hoffman, G. McLennan, and J.M. and Reinhardt. Segmentation and analysis of the human airway tree from three-dimensional x-ray CT images. *IEEE Transactions on Medical Imaging*, 22(8):940–950, 2003.
- [4] P.B. Bach, J.R. Jett, U. Pastorino, M.S. Tockman, S.J. Swensen, and C.B. Begg. Computed tomography screening and lung cancer outcomes. *Journal of the American Medical Association*, 297(9):953–961, 2007.
- [5] D. Bartz, D. Mayer, J. Fischer, S. Ley, A. del Rio, S. Thust, C. P. Heussel, H. U. Kauczor, and W. Strasser. Hybrid segmentation and exploration of the human lungs. In *IEEE Visualization 2003*, pages 177–84, Seattle, WA, USA, 2003.
- [6] H.D. Becker, F. Herth, A. Ernst, and Y. Schwarz. Bronchoscopic biopsy of peripheral lung lesions under electromagnetic guidance. *Journal of Bronchology*, 12(1):9–13, 2005.
- [7] Thomas Bülow, Cristian Lorenz, and Steffen Renisch. A general framework for tree segmentation and reconstruction from medical volume data. In *Medical Image Computing and Computer-Assisted Intervention, MICCAI 2004 - 7th International Conference, Proceedings*, volume 3216, pages 533–540, Saint-Malo, France, 2004.
- [8] V. Boldea, D. Sarrut, and C. Carrie. Comparison of 3D dense deformable registration methods for breath-hold reproducibility study in radiotherapy. In *Medical Imaging 2005: Image Processing*, volume 5747, pages 222–30, San Diego, CA, USA, 2005.
- [9] I. Bricault, G. Ferretti, and P. Cinquin. Registration of real and CT-derived virtual bronchoscopic images to assist transbronchial biopsy. 17(5):703–14, October 1998.

- [10] C.M. Brown. *Scanning Fiber Endoscope Design for In Vivo Imaging of the Gastrointestinal System*. PhD thesis, University of Washington, 2008.
- [11] J. Bulat, K. Duda, M. Socha, P. Turcza, T. Zielinski, and M. Duplaga. Computational tasks in bronchoscope navigation during computer-assisted transbronchial biopsy. In *Computational Science - ICCS 2008. 8th International Conference*, pages 178–87, Krakow, Poland, 2008.
- [12] S. K. Carlson, J.P. Felmlee, C.E. Bender, R.L. Ehman, K.L. Classic, T.L. Hoskin, W.S. Harmsen, and H.H. Hu. CT-fluoroscopy-guided biopsy of the lung or upper abdomen with a breath-hold monitoring and feedback system: A prospective randomized controlled clinical trial. *Radiology*, 237(2):701–708, 2005.
- [13] M.D. Cham, M.E. Lane, C. I. Henschke, and D.F. Yankelevitz. Lung biopsy: special techniques. *Seminars in Respiratory and Critical Care Medicine*, 29(4):335–349, 2008.
- [14] G. E. Christensen and H. J. Johnson. Invertibility and transitivity analysis for non-rigid image registration. 12(1):106–17, January 2003.
- [15] J.A. Christensen, M.A. Nathan, B.P. Mullan, T.E. Hartman, S.J. Swensen, and V.J. Lowe. Characterization of the solitary pulmonary nodule: 18F-FDG PET versus nodule-enhancement CT. *American Journal of Roentgenology*, 187(5):1361–1367, 2006.
- [16] Adrian J. Chung, Fani Deligianni, Pallav Shah, Athol Wells, and Guang-Zhong Yang. Patient-specific bronchoscopy visualization through BRDF estimation and disocclusion correction. 25(4):503–513, April 2006.
- [17] S. Connor, J. Dyer, and P. Guest. Image-guided automated needle biopsy of 106 thoracic lesions: a retrospective review of diagnostic accuracy and complication rates. *European Radiology*, 10(3):490–494, 2000.
- [18] M.M. Coselmon, J.M. Balter, McShan D.L., and Kessler M.L. Mutual information based CT registration of the lung at exhale and inhale breathing states using thin-plate splines. *Med. Phys.*, 31:2942–2948, 2004.
- [19] J. S. Day, D. J. Murdoch, and G. A. Dumas. Calibration of position and angular data from a magnetic tracking device. *J Biomech*, 33:1039–1045, Aug 2000.
- [20] Daisuke Deguchi, K. Ishitani, T. Kitasaka, Kensaku Mori, Y. Suenaga, H. Takabatake, M. Mori, and H. Natori. A method for bronchoscope tracking using position

sensor without fiducial markers. In *Medical Imaging 2007: Physiology, Function, and Structure from Medical Images*, volume 6511, San Diego, CA, USA, 2007.

- [21] Daisuke Deguchi, Kensaku Mori, Jun-Ichi Hasegawa, Junichiro Toriwaki, Hirotsugu Takabatake, and Hiroshi Natori. Camera motion tracking of real bronchoscope using epipolar geometry analysis and CT derived bronchoscopic images. In *Medical Imaging 2002: Physiology and Function from Multidimensional Images*, volume 4683, pages 30–41, San Diego, CA, United states, 2002.
- [22] F. Deligianni, A. Chung, and G.Z. Yang. Patient-specific bronchoscope simulation with pq-space-based 2D/3D registration. *Computer Aided Surgery*, 9(5):215–226, 2004.
- [23] F. Deligianni, A. J. Chung, and Guang-Zhong Yang. Non-rigid 2D-3D registration with catheter tip EM tracking for patient specific bronchoscope simulation. In *Medical Image Computing and Computer-Assisted Intervention - MICCAI 2006. 9th International Conference. Proceedings, Part I*, pages 281–8, Copenhagen, Denmark, 2006.
- [24] L. Dougherty, J.C. Asmuth, and W.B. Gefter. Alignment of CT lung volumes with an optical flow method. *Academic Radiology*, 10:249–254, 2003.
- [25] F. Duru. CARTO three-dimensional non-fluoroscopic electroanatomic mapping for catheter ablation of arrhythmias: a useful tool or an expensive toy for the electrophysiologist? *Anadolu Kardiyol Derg*, 2:330–337, Dec 2002.
- [26] R. Eberhardt, D. Anantham, F. Herth, D. Feller-Kopman, and A. Ernst. Electromagnetic navigation diagnostic bronchoscopy in peripheral lung lesions. *Chest*, 131:1800–1805, Jun 2007.
- [27] R. Eberhardt, A. Ernst, and F. J. Herth. Ultrasound-guided transbronchial biopsies of solitary pulmonary nodules less than 20 mm. *Eur. Respir. J.*, May 2009.
- [28] L. Fan, Chang Wen Chen, J. M. Reinhardt, and E. A. Hoffman. Evaluation and application of 3d lung warping and registration model using HRCT images. In *Medical Imaging 2001: Physiology and Function from Multidimensional Images*, volume 4321, pages 234–243, Sandiego, CA, United states, 2001.
- [29] C. I. Fetita, F. Preteux, C. Beigelman-Aubry, and P. Grenier. Pulmonary airways: 3-d reconstruction from multislice CT and clinical investigation. 23(11):1353–64, November 2004.

- [30] J. M. Fitzpatrick and J. B. West. The distribution of target registration error in rigid-body point-based registration. 20(9):917–927, September 2001.
- [31] J. Michael Fitzpatrick, Jay B. West, and Calvin R. Maurer Jr. Predicting error in rigid-body point-based registration. 17(5):694–702, October 1998.
- [32] D. D. Frantz, A. D. Wiles, S. E. Leis, and S. R. Kirsch. Accuracy assessment protocols for electromagnetic tracking systems. *Phys Med Biol*, 48:2241–2251, Jul 2003.
- [33] K. Furuya, S. Murayama, H. Soeda, J. Murakami, Y. Ichinose, H. Yabuuchi, Y. Katsuda, M. Koga, and K. Masuda. New classification of small pulmonary nodules by margin characteristics on high-resolution CT. *Acta Radiol*, 40:496–504, Sep 1999.
- [34] B. Geiger, A. P. Kiraly, D. P. Naidich, and C. L. Novak. Virtual bronchoscopy of peripheral nodules using arteries as surrogate pathways. In *Medical Imaging 2005: Physiology, Function, and Structure from Medical Images*, volume 5746, pages 352–60, San Diego, CA, USA, 2005.
- [35] B. Geiger, G. M. Weiner, K. Schulze, J. Bilger, P. Krebs, K. J. Wolf, and T. Albrecht. Virtual bronchoscopy guidance system for transbronchial needle aspiration. In *Medical Imaging 2005: Physiology, Function, and Structure from Medical Images*, volume 5746, pages 361–8, San Diego, CA, USA, 2005.
- [36] L. Gepstein, G. Hayam, and S. A. Ben-Haim. A novel method for nonfluoroscopic catheter-based electroanatomical mapping of the heart. In vitro and in vivo accuracy results. *Circulation*, 95:1611–1622, Mar 1997.
- [37] J. D. Gibbs, M. W. Graham, Kun-Chang Yu, and W. E. Higgins. Integrated system for planning peripheral bronchoscopic procedures. In *Medical Imaging 2008: Physiology, Function, and Structure from Medical Images*, volume 6916, pages 1–15, San Diego, CA, USA, March 2006.
- [38] M.S. Ginsberg, S.K. Griff, B.D. Go, H.H. Yoo, L.H. Schwartz, and D.M. Panicek. Pulmonary nodules resected at video-assisted thoracoscopic surgery: etiology in 426 patients. *Radiology*, 213:277–282, 1999.
- [39] J. Gong, G. Mohr, and J. L. Vézina. Endoscopic pituitary surgery with and without image guidance: an experimental comparison. *Surg Neurol*, 67:572–578, Jun 2007.
- [40] M.K. Gould, A. Ananth, and P.G. Barnett. A clinical model to estimate the pretest probability of lung cancer in patients with solitary pulmonary nodules. *Chest*, 131:383–388, 2007.

- [41] M.K. Gould, G.D. Sanders, C.E. Barnett, P.G. Rydzak, and C.C. Maclean. Cost-effectiveness of alternative management strategies for patients with solitary pulmonary nodules. *Annals of Internal Medicine*, 238(9):724–735, 2003.
- [42] M. W. Graham, J. D. Gibbs, and W. E. Higgins. Robust system for human airway-tree segmentation. In *Progress in Biomedical Optics and Imaging: Medical Imaging 2008: Image Processing*, volume 6914, pages 1–18, San Diego, CA, USA, 2008.
- [43] T. Guerrero, K. Sanders, J. Noyola-Martinez, E. Castillo, Y. Zhang, R. Tapia, R. Guerra, Y. Borghero, and R. Komaki. Quantification of regional ventilation from treatment planning CT. *Int. J. Radiation Oncology Biol. Phys.*, 62:630–634, 2005.
- [44] N.C. Gupta, J. Maloof, and Gunel E. Probability of malignancy in solitary pulmonary nodules using fluorine-18-FDG and PET. *Journal of Nuclear Medicine*, 37:943–948, 1996.
- [45] J.W. Gurney. Determining the likelihood of malignancy in solitary pulmonary nodules with Bayesian analysis. Part I. Theory. *Radiology*, 186(2):405–413, 1993.
- [46] André Guézic. *Handbook of Medical Imaging, Volume 2. Medical Image Processing and Analysis*. SPIE Press, 2000.
- [47] P. Haignon, M. E. Bellemare, O. Acosta, C. Goksu, C. Kulik, K. Rioual, and A. Lucas. Depth-map-based scene analysis for active navigation in virtual angiography. 23(11):1380–90, November 2004.
- [48] A. Hartov, S.D. Eisner, D.W. Roberts, K.D. Paulsen, L.A. Platenik, and M.I. Miga. Error analysis for a free-hand three-dimensional ultrasound system for neuronavigation. *Neurosurgery Focus*, 6(3), 1999.
- [49] H. Hautmann, A. Schneider, T. Pinkau, F. Peltz, and H. Feussner. Electromagnetic catheter navigation during bronchoscopy: validation of a novel method by conventional fluoroscopy. *Chest*, 128:382–387, Jul 2005.
- [50] J. P. Helferty, E. A. Hoffman, G. McLennan, and W. E. Higgins. CT-video registration accuracy for virtual guidance of bronchoscopy. In *Medical Imaging 2004. Physiology, Function, and Structure from Medical Images*, volume 5369, pages 150–64, San Diego, CA, USA, 2004.
- [51] J. P. Helferty, A. J. Sherbondy, A. P. Kiraly, and W. E. Higgins. System for live virtual-endoscopic guidance of bronchoscopy. In *Computer Vision and Pattern Recognition, 2005 IEEE Computer Society Conference on*, pages 68–68, San Diego, CA, USA, June 2005.

- [52] C. I. Henschke, D. F. Yankelevitz, R. Mirtcheva, G. McGuinness, D. McCauley, and O. S. Miettinen. CT screening for lung cancer: frequency and significance of part-solid and nonsolid nodules. *AJR Am J Roentgenol*, 178:1053–1057, May 2002.
- [53] C.I. Henschke, D.F. Yankelevitz, D.M. Libby, M.W. Pasmantier, and J.P. Smith. Survival of patients with stage I lung cancer detected on CT screening. *The New England Journal of Medicine*, 355(17):1763–1771, 2006.
- [54] F. J. Herth, A. Ernst, and H. D. Becker. Endobronchial ultrasound-guided transbronchial lung biopsy in solitary pulmonary nodules and peripheral lesions. *Eur. Respir. J.*, 20:972–974, Oct 2002.
- [55] C.M. Heyer, S. Reichelt, S.A. Peters, J.W. Walther, K.M. Muller, and V. Nicolas. Computed tomography -navigated transthoracic core biopsy of pulmonary lesions: which factors affect diagnostic yield and complication rates? *Academic Radiology*, 15(8):1017–1026, 2008.
- [56] W. E. Higgins, L. Rai, S. A. Merritt, K. Lu, N. T. Linger, and K. C. Yu. 3d image fusion and guidance for computer-assisted bronchoscopy. In *Three-Dimensional TV, Video, and Display IV*, volume 6016, Boston, MA, United states, 2005.
- [57] W.E. Higgins, J.P. Helferty, and D.R. Padfield. Integrated bronchoscopic video tracking and 3D CT registration for virtual bronchoscopy. *SPIE Medical Imaging 2003:Physiology and Function - Methods, Systems and Applications*, 5031:80–89, 2003.
- [58] P. Hildebrand, V. Martens, A. Schweikard, S. Schlichting, A. Besirevic, M. Klee-mann, U. Roblick, L. Mirow, C. Bürk, and H. P. Bruch. Evaluation of an online navigation system for laparoscopic interventions in a perfused ex vivo artificial tumor model of the liver. *HPB (Oxford)*, 9:190–194, 2007.
- [59] Michael P. Hlasta and Albert J. Berger. *Physiology of Respiration*. Oxford University Press, 2001.
- [60] J. D. Hoisak, K. E. Sixel, R. Tirona, P. C. Cheung, and J. P. Pignol. Correlation of lung tumor motion with external surrogate indicators of respiration. *Int. J. Radiat. Oncol. Biol. Phys.*, 60:1298–1306, Nov 2004.
- [61] B. K. P. Horn. Closed-form solution of absolute orientation using unit quaternions. 4(4):629–42, April 1987.

- [62] S. Hu, E. A. Hoffman, and J. M. Reinhardt. Automatic lung segmentation for accurate quantitation of volumetric X-ray CT images. 20(6):490–498, June 2001.
- [63] J. Hummel, M. Figl, W. Birkfellner, M. R. Bax, R. Shahidi, C. R. Maurer, and H. Bergmann. Evaluation of a new electromagnetic tracking system using a standardized assessment protocol. *Phys Med Biol*, 51:N205–210, May 2006.
- [64] J. Hummel, M. Figl, W. Birkfellner, M. Hafner, C. Kollmann, and H. Bergmann. Navigation system for flexible endoscopes. In *Medical Imaging 2003 Visualization, Image-Guided Procedures, and Display*, volume 5029, pages 303–10, San Diego, CA, USA, 2003.
- [65] Johann1 Hummel, Michael Figl, Michael Bax, Ramin Shahidi, Helmar Bergmann, and Wolfgang Birkfellner. Evaluation of dynamic electromagnetic tracking deviation. In *Medical Imaging 2009: Biomedical Applications in Molecular, Structural, and Functional Imaging*, volume 7261, Lake Buena Vista, FL, United states, 2009.
- [66] K. Ishitani, D. Daisuke, T. Kitasaka, K. Mori, Y. Suenaga, H. Takabatake, M. Mori, and H. Natori. Easy and stable bronchoscope camera calibration technique for bronchoscope navigation system. In *Medical Imaging 2007: Visualization and Image-Guided Procedures*, volume 6509, San Diego, CA, USA, 2007.
- [67] M.F. Jimenez. Prospective study on video-assisted thoracoscopic surgery in the resection of pulmonary nodules: 209 cases from the Spanish Video-Assisted Thoracic Surgery Study Group. *European Journal of Cardiothoracic Surgery*, 19(5):562–565, 2001.
- [68] H. J. Johnson and G. E. Christensen. Consistent landmark and intensity-based image registration. In *17th International Conference on Information Processing in Medical Imaging (IPMI'01)*, volume 21, pages 450–461, Davis, CA, United states, May 2002.
- [69] R.E. Kalman. A new approach to linear filtering and prediction problems. *Transactions of the ASME - Journal of Basic Engineering*, pages 35–45, 1960.
- [70] K. Kanoh, T. Miyazawa, N. Kurimoto, Y. Iwamoto, Y. Miyazu, and N. Kohno. Endobronchial ultrasonography for transbronchial needle aspiration using a double-channel bronchoscope. *Chest*, 128:388–393, 2005.
- [71] N.F. Khouri, Stitik. F.P., Y.S. Erozan, P.K. Gupta, W.S. Kim, U.M. Scott, W.W. Hamper, R.B. Mann, J.C. Eggleston, and R.R. Baker. Transthoracic needle aspiration biopsy of benign and malignant lung lesions. *American Journal of Roentgeneology*, 144(2):281–288, 1985.

- [72] Y.H. Kim, K.S. Lee, S.L. Primack, H. Kim, O.J. Kwon, T.S. Kim, E.A. Kim, J. Kim, and Y.M. Shim. Small pulmonary nodules on CT accompanying surgically resectable lung cancer: likelihood of malignancy. *Journal of Thoracic Imaging*, 17:40–46, 2002.
- [73] J. Kindblom, A. M. Ekelund-Olvenmark, H. Syren, R. Iustin, K. Braide, I. Frank-Lissbrant, and B. Lennernäs. High precision transponder localization using a novel electromagnetic positioning system in patients with localized prostate cancer. *Radiother Oncol*, 90:307–311, Mar 2009.
- [74] A. P. Kiraly, J. P. Helferty, E. A. Hoffman, G. McLennan, and W. E. Higgins. Three-dimensional path planning for virtual bronchoscopy. 23(11):1365–79, November 2004.
- [75] A. P. Kiraly, W. E. Higgins, E. A. Hoffman, G. McLennan, and J. M. Reinhardt. 3d human airway segmentation for virtual bronchoscopy. In *Medical Imaging 2002: Physiology and Function from Multidimensional Images*, volume 4683, pages 16–29, San Diego, CA, USA, 2002.
- [76] Tassilo Klein, Joerg Traub, Hubert Hautmann, Alireza Ahmadian, and Nassir Navab. Fiducial-free registration procedure for navigated bronchoscopy. In *10th International Conference on Medical Image Computing and Computer-Assisted Intervention, MICCAI 2007*, volume 4791, pages 475–482, Brisbane, Australia, 2007.
- [77] W. Konen, S. Tombrock, and M. Scholz. Robust registration procedures for endoscopic imaging. *Medical Image Analysis*, 11:526–539, 2007.
- [78] B. Kuehn, S. Mularski, S. Schoenherr, S. Hammersen, R. Stendel, T. Kombos, S. Suess, and O. Suess. Sensor-based neuronavigation: evaluation of a large continuous patient population. *Clin Neurol Neurosurg*, 110:1012–1019, Dec 2008.
- [79] T. Laisaar, T. Vooder, and T. Umbleja. Thoracoscopic resection of a solitary pulmonary nodule in patients with a known history of malignancy. *The Thoracic and Cardiovascular Surgeon*, 56(7):418–421, 2008.
- [80] S. Lam, B. Standsh, C. Baldwin, A. McWilliams, J. leRiche, A. Gazdar, A.I. Vitkin, V. Yang, N. Ikeda, and C. MacAulay. In vivo optical coherence tomography imaging of preinvasive bronchial lesions. *Clinical Cancer Research*, 14(7):2006–2011, 2008.
- [81] D. F. Leotta, P. R. Detmer, and R. W. Martin. Performance of a miniature magnetic position sensor for three-dimensional ultrasound imaging. *Ultrasound Med Biol*, 23:597–609, 1997.

- [82] P. Lo, , and M. de Bruijne. Voxel classification based airway tree segmentation. In *SPIE Medical Imaging: Image Processing*, volume 6914, San Diego, CA, USA, 2008.
- [83] S. Loncaric, T. Markovinovic, T. Petrovic, D. Ramljak, and E. Sorantin. Construction of virtual environment for endoscopy. 1:475–480, 1999.
- [84] William E. Lorensen and Harvey E. Cline. Marching cubes: A high resolution 3D surface construction algorithm. *Computer Graphics*, 21(4)(4):163–169, July 1987.
- [85] Kongkuo Lu and W. E. Higgins. Improved 3d live-wire method with application to 3d CT chest image analysis. In *Medical Imaging 2006: Image Processing*, volume 6144, pages 1–15, San Diego, CA, USA, 2006.
- [86] Andrew R. Lumb. *Nunn's Applied Respiratory Physiology*. Elsevier Butterworth Heinemann, 2005.
- [87] G. S. Mageras, A. Pevsner, E. D. Yorke, K. E. Rosenzweig, E. C. Ford, A. Hertanto, S. M. Larson, D. M. Lovelock, Y. E. Erdi, S. A. Nehmeh, J. L. Humm, and C. C. Ling. Measurement of lung tumor motion using respiration-correlated CT. *Int. J. Radiat. Oncol. Biol. Phys.*, 60:933–941, Nov 2004.
- [88] D. Mayer, D. Bartz, J. Fischer, A. Ley, S. del Rio, S. Thust, Kauczor H.U., and Heussel C.P. Hybrid segmentation and virtual bronchoscopy based on CT images. *Academic Radiology*, 11:551–565, 2004.
- [89] H. P. McAdams, P. C. Goodman, and P. Kussin. Virtual bronchoscopy for directing transbronchial needle aspiration of hilar and mediastinal lymph nodes: a pilot study. *AJR Am J Roentgenol*, 170:1361–1364, May 1998.
- [90] G. McLennan, E. A. Hoffman, R. D. Swift, and W. E. Higgins. Virtual bronchoscopic assessment of major airway obstructions. 3660:313–320, 1999.
- [91] H. McMahon, J.H. Austin, G. Gamsu, Herold. C.J., D.P. Jett, J.R. and Naidich, E.F. Patz, and S.J. Swensen. Guidelines for management of small pulmonary nodules detected on CT scans: a statement from the Fleischner Society. *Radiology*, 237(2):395–400, 2005.
- [92] S. A. Merritt, L. Rai, J. D. Gibbs, Kun-Chang Yu, and W. E. Higgins. Method for continuous guidance of endoscopy. In *Medical Imaging 2007: Physiology, Function, and Structure from Medical Images*, volume 6511, San Diego, CA, USA, 2007.

- [93] S. A. Merritt, L. Rai, and W. E. Higgins. Real-time CT-video registration for continuous endoscopic guidance. In *Medical Imaging 2006: Physiology, Function, and Structure from Medical Images*, volume 6143, pages 614313–1, San Diego, CA, USA, 2006.
- [94] R. Miranda-Luna, Y. Hernandez-Mier, Ch. Daul, W. C. P. M. Blondel, and D. Wolf. Mosaicing of medical video-endoscopic images: Data quality improvement and algorithm testing. In *2004 1st International Conference on Electrical and Electronics Engineering, ICEEE*, pages 530–535, Acapulco, Mexico, 2004.
- [95] T. Miyoshi, K. Kondo, H. Fujino, S. Sakiyama, and A. Tangoku. Fluoroscopy-assisted thorascopic resection of pulmonary nodules after computed tomography-guided bronchoscopic metallic coil marking. *The Journal of Thoracic and Cardiovascular Surgery*, 131:704–710, 2006.
- [96] K. Mori, D. Deguchi, K. Akiyama, T. Kitasaka, Jr. Maurer, C. R., Y. Suenaga, H. Takabatake, M. Mori, and H. Natori. Hybrid bronchoscope tracking using a magnetic tracking sensor and image registration. In *Medical Image Computing and Computer-Assisted Intervention-MICCAI 2005. 8th International Conference. Proceedings, Part II*, pages 543–50, Palm Springs, CA, USA, 2005.
- [97] K. Mori, D. Deguchi, K. Ishitani, T. Kitasaka, Y. Suenaga, Y. Hasegawa, K. Imaizumi, and H. Takabatake. Bronchoscope tracking without fiducial markers using ultra-tiny electromagnetic tracking system and its evaluation in different environments. In *10th International Conference on Medical Imaging and Computer-Assisted Intervention, MICCAI 2007*, volume 4792, pages 644–651, Brisbane, Australia, 2007.
- [98] K. Mori, D. Deguchi, Y. Sugiyama, J. Toriwaki, C.R. Maurer, H. Takabatake, and H. Natori. Tracking of a bronchoscope using epipolar geometry analysis and intensity-based image registration and virtual endoscopic images. *Medical Image Analysis*, 6:321–336, 2002.
- [99] K. Mori, T. Enjoji, D. Deguchi, T. Kitasaka, Y. Suenaga, J. Toriwaki, H. Takabatake, and H. Natori. New image similarity measures for bronchoscope tracking based on image registration between virtual and real bronchoscopic images. In *Medical Imaging 2004. Physiology, Function, and Structure from Medical Images*, volume 5369, pages 165–76, San Diego, CA, USA, 2004.
- [100] K. Mori, J. Hasegawa, J. Toriwaki, H. Anno, and K. Katada. Recognition of bronchus in three-dimensional X-ray CT images with applications to virtualized bronchoscopy

- system. In *Proceedings of 13th International Conference on Pattern Recognition*, pages 528–32, Vienna, Austria, 1996.
- [101] Kensaku Mori, Yasuhito Suenaga, Jun-ichiro Toriwaki, Jun-ichi Hasegawa, Kazuhiro Katada, Hirotsugu Takabatake, and Hiroshi Natori. Method for tracking camera motion of real endoscope by using virtual endoscopy system. 3978:122–133, 2000.
- [102] Kensaku1 Mori, Jun-Ichi1 Hasegawa, Yasuhito1 Suenaga, and Jun-Ichiro1 Toriwaki. Automated anatomical labeling of the bronchial branch and its application to the virtual bronchoscopy system. 19(2):103–114, 2000.
- [103] Christopher Nafis, Vern Jensen, Lee Beauregard, and Peter Anderson. Method for estimating dynamic em tracking accuracy of surgical navigation tools. In *Medical Imaging 2006: Visualization, Image-Guided Procedures, and Display*, volume 6141, San Diego, CA, United states, 2006.
- [104] J. Nagao, K. Mori, T. Enjouji, D. Deguchi, T. Kitasaka, Y. Suenaga, J. Hasegawa, J. Toriwaki, H. Takabatake, and H. Natori. Fast and accurate bronchoscope tracking using image registration and motion prediction. In *Medical Image Computing and Computer-Assisted Intervention - MICCAI 2004. 7th International Conference. Proceedings*, pages 551–8, Saint-Malo, France, 2004.
- [105] Y. Ohno, H. Hatabu, D. Takenaka, T. Higashino, H. Watanabe, C. Ohbayashi, and K. Sugimura. CT-guided transthoracic needle aspiration biopsy of small (< or= 20mm) solitary pulmonary nodules. *American Journal of Roentgeneology*, 180(6):1665–1669, 2003.
- [106] Kalman Palagyi, Juerg Tschirren, and Milan Sonka. Quantitative analysis of three-dimensional tubular tree structures. In *Medical Imaging 2003: Image Processing*, volume 5032, pages 277–287, San Diego, CA, United states, 2003.
- [107] Y. Pan, D. Kumar, E. A. Hoffman, G. E. Christensen, G. McLennan, Joo Hyun Song, A. Ross, B. A. Simon, and J. M. Reinhardt. Estimation of regional lung expansion via 3d image registration. In *Medical Imaging 2005: Physiology, Function, and Structure form Medical Images*, volume 5746, pages 453–64, San Diego, CA, USA, 2005.
- [108] Wonkyu Park, Eric A. Hoffman, and Milan Sonka. Segmentation of intrathoracic airway trees: A fuzzy logic approach. 17(4):489–497, August 1998.

- [109] T. Popa, L. Ibanez, K. Cleary, and K. H. Wong. ITK implementation of deformable registration methods for time-varying (4d) imaging data. In *Medical Imaging 2006: Visualization, Image-Guided Procedures, and Display*, volume 6141, pages 1–10, San Diego, CA, USA, 2006.
- [110] H. Prosch, G. Strasser, E. Oschatz, E. Schober, B. Schneider, and G.H. Mostbeck. Management of patients with small pulmonary nodules: a survey of radiologists, pulmonologists, and thoracic surgeons. *American Journal of Roentgenology*, 187:143–148, 2006.
- [111] Lav Rai and William E. Higgins. Method for radiometric calibration of an endoscope’s camera and light source. In *Medical Imaging 2008 - Visualization, Image-Guided Procedures, and Modeling*, volume 6918, San Diego, CA, United states, 2008.
- [112] Lav Rai and William E. Higgins. Fusion of MDCT-based Endoluminal Renderings and Endoscopic Video. In *Medical Imaging 2009: Biomedical Applications in Molecular, Structural, and Functional Imaging*, volume 7261, Lake Buena Vista, FL, United states, 2009.
- [113] H.U. Rashid and P. Burger. Differential algorithm for the determination of shape from shading using a point light source. *Image and Vision Computing*, 10(2):119–127, 1992.
- [114] Joseph M. Reinhardt, Wonkyu Park, Eric A. Hoffman, and Milan Sonka. Intrathoracic airway wall detection using graph search and scanner PSF information. In *Medical Imaging 1997: Physiology and Function from Multidimensional Images*, volume 3033, pages 93–101, Newport Beach, CA, USA, 1997.
- [115] M.P. Rivera, Deetterbeck. F., and A.C. Mehta. Diagnosis of lung cancer. the guidelines. *Chest*, 123:129S–136S, 2003.
- [116] C.P. Rooney, K Wolf, and G. McLennan. Ultrathin bronchoscopy as an adjunct to standard bronchoscopy in the diagnosis of peripheral lung lesions. *Respiration*, 69:63–68, 2002.
- [117] P.K. Saha, B.B. Chaudhuri, and D.D. Majumder. A new shape preserving parallel thinning algorithm for 3D digital images. *Pattern Recognition*, 30(12):1939–1955, 1997.
- [118] D. Sarrut, V. Boldea, M. Ayadi, J. N. Badel, C. Ginestet, S. Clippe, and C. Carrie. Nonrigid registration method to assess reproducibility of breath-holding with ABC in lung cancer. *Int. J. Radiat. Oncol. Biol. Phys.*, 61:594–607, Feb 2005.

- [119] M. Schneider and C. Stevens. Development and testing of a new magnetic-tracking device for image guidance. In *Medical Imaging 2007: Visualization and Image-Guided Procedures*, volume 6509, San Diego, CA, USA, 2007.
- [120] Y. Schwarz, A.C. Mehta, A. Ernst, F. Herth, A. Engel, D. Besser, and H.D. Becker. Electromagnetic navigation during flexible bronchoscopy. *Interventional Pulmonology*, 70:516–522, 2003.
- [121] M. D. Seemann, A. Staebler, T. Beinert, H. Dienemann, B. Obst, M. Matzko, C. Pistitsch, and M. F. Reiser. Usefulness of morphological characteristics for the differentiation of benign from malignant solitary pulmonary lesions using HRCT. *Eur Radiol*, 9:409–417, 1999.
- [122] E. J. Seibel, R. E. Carroll, J. A. Dominitz, R. S. Johnston, C. D. Melville, C. M. Lee, S. M. Seitz, and M. B. Kimmey. Tethered capsule endoscopy, a low-cost and high-performance alternative technology for the screening of esophageal cancer and Barrett’s esophagus. 55(3):1032–42, March 2008.
- [123] E. J. Seibel and Q. Y. Smithwick. Unique features of optical scanning, single fiber endoscopy. *Lasers Surg Med*, 30:177–183, 2002.
- [124] E. Shen, G. Shechter, J. Kruecker, and D. Stanton. Quantification of AC electromagnetic tracking system accuracy in a CT scanner environment. In *Medical Imaging 2007: Visualization and Image-Guided Procedures*, volume 6509, San Diego, CA, USA, 2007.
- [125] Anthony J. Sherbondy, Atilla P. Kiraly, Allen L. Austin, James P. Helferty, Shu-Yen Wan, Janice Z. Turlington, Tao Yang, Chao Zhang, Eric A. Hoffman, Geoffrey McLennan, and William E. Higgins. Virtual bronchoscopic approach for combining 3d CT and endoscopic video. 3978:104–116, 2000.
- [126] N. Shinagawa, K. Yamazaki, and Y. Onodera. CT-guided transbronchial biopsy using an ultrathin bronchoscope with virtual bronchoscopic navigation. *Chest*, 125:1138–1143, 2004.
- [127] H. Shirato, T. Harada, T. Harabayashi, K. Hida, H. Endo, K. Kitamura, R. Onimaru, K. Yamazaki, N. Kurauchi, T. Shimizu, N. Shinohara, M. Matsushita, H. Dosaka-Akita, and K. Miyasaka. Feasibility of insertion/implantation of 2.0-mm-diameter gold internal fiducial markers for precise setup and real-time tumor tracking in radiotherapy. *Int. J. Radiat. Oncol. Biol. Phys.*, 56:240–247, May 2003.

- [128] American Cancer Society. Cancer facts & figures 2008. Atlanta: American Cancer Society, 2006.
- [129] O. V. Solberg, T. Langø, G. A. Tangen, R. Mårvik, B. Ystgaard, A. Rethy, and T. A. Hernes. Navigated ultrasound in laparoscopic surgery. *Minim Invasive Ther Allied Technol*, 18:36–53, 2009.
- [130] S.B. Solomon, P. White, D.E. Acker, J. Strandberg, and A.C. Venbrux. Real-time bronchoscope tip localization enables three-dimensional CT image guidance for transbronchial needle aspiration in swine. *Chest*, 114:1405–1410, 1998.
- [131] S.B. Solomon, P. White, C.M. Wiener, J.B. Orens, and K.P. Wang. Three-dimensional CT-guided bronchoscopy with a real-time electromagnetic position sensor. *Chest*, 118:1783–1787, 2000.
- [132] Milan Sonka, Wonkyu Park, and Eric A. Hoffman. Rule-based detection of intrathoracic airway trees. 15(3):314–326, June 1996.
- [133] T. D. Soper, D. R. Haynor, R. W. Glenny, and E. J. Seibel. A model of respiratory airway motion for real-time tracking of an ultrathin bronchoscope. In *Medical Imaging 2007: Physiology, Function, and Structure from Medical Images*, volume 6511, San Diego, CA, USA, 2007.
- [134] T. D. Soper, D. R. Haynor, R. W. Glenny, and E. J. Seibel. In vivo validation of a hybrid tracking system for navigation of an ultrathin bronchoscope within peripheral airways. *IEEE Transactions in Biomedical Engineering*, In Press, 2009.
- [135] Timothy D. Soper, David R. Haynor, Robb W. Glenny, and Eric J. Seibel. Validation of CT-video registration for guiding a novel ultrathin bronchoscope to peripheral lung nodules using electromagnetic tracking. In *Medical Imaging 2009: Biomedical Applications in Molecular, Structural, and Functional Imaging*, volume 7261, Lake Buena Vista, FL, United states, 2009.
- [136] C. Studholme, D.L.G. Hill, and D.J. Hawkes. An overlap invariant entropy measure of 3D medical image alignment. *Pattern recognition*, 32:71–86, 1999.
- [137] O. Suess, S. Suess, S. Mularski, B. Kühn, T. Picht, S. Schönherr, and T. Kombos. [Evaluation of a DC pulsed magnetic tracking system in neurosurgical navigation: technique, accuracies, and influencing factors]. *Biomed Tech (Berl)*, 52:223–233, 2007.

- [138] Takamasa Sugiura, Daisuke Deguchi, Marco Feuerstein, Takayuki² Kitasaka, Yasuhito¹ Suenaga, and Kensaku¹ Mori. A method for accelerating bronchoscope tracking based on image registration by using GPU. In *Medical Imaging 2009: Biomedical Applications in Molecular, Structural, and Functional Imaging*, volume 7261, Lake Buena Vista, FL, United states, 2009.
- [139] R.M. Summers, D.H. Feng, M.C. Holland, S.M. Sneller, and J.H. Shelhamer. Virtual bronchoscopy: Segmentation method for real-time display. *Radiology*, 200:857–862, 1996.
- [140] T.A. Sundaram and J.C. Gee. Towards a model of lung biomechanics: pulmonary kinematics via registration of serial lung images. *Medical Image Analysis*, 9:524–537, 2005.
- [141] M. Suter, J. M. Reinhardt, E. A. Hoffman, and G. McLennan. 3d pulmonary airway color image reconstruction via shape from shading and virtual bronchoscopy imaging techniques. In *Medical Imaging 2005: Image Processing*, volume 5747, pages 755–63, San Diego, CA, USA, 2005.
- [142] J.L. Swischuk, G. Castaneda, J.C. Patel, R. Li, K.W. Fraser, T.M. Brady, and R.E. Bertino. Percutaneous transthoracic needle biopsy of the lung: review of 612 lesions. *Journal Vascular and Interventional Radiology*, 9(2):347–352, 1998.
- [143] A. Szymczak and J. Vanderhyde. Airway segmentation by topology-driven local thresholding. In *SPIE Medical Imaging: Image Processing*, volume 6914, San Diego, CA, USA, 2008.
- [144] M. Tachihara, T. Ishida, K. Kanazawa, A. Sugawara, K. Watanabe, K. Uekita, H. Moriya, K. Yamazaki, F. Asano, and M. Munakata. A virtual bronchoscopic navigation system under X-ray fluoroscopy for transbronchial diagnosis of small peripheral pulmonary lesions. *Lung Cancer*, 57:322–327, Sep 2007.
- [145] G. Taubin. A signal processing approach to fair surface design. In *Proceedings of SIGGRAPH '95*, pages 351–8, Los Angeles, CA, USA, 1995.
- [146] M. H. Tawhai, M. P. Nash, and E. A. Hoffman. An imaging-based computational approach to model ventilation distribution and soft-tissue deformation in the ovine lung. *Acad Radiol*, 13:113–120, Jan 2006.
- [147] J.P. Thirion. *Fast Non-Rigid Matching of 3D Medical Images*. PhD thesis, Institut National de Recherche en Informatique et en Automatique, 1995.

- [148] J.P. Thirion. Image matching as a diffusion process: an analogy to Maxwell's demons. *Medical Image Analysis*, 2:243–260, 1998.
- [149] H. Timinger, S. Krueger, J. Borgert, and R. Grewer. Motion compensation for interventional navigation on 3d static roadmaps based on an affine model and gating. 49(5):719–32, March 2007.
- [150] R.Y. Tsai. A versatile camera calibration technique for high-accuracy 3D machine vision metrology using off-the-shelf TV cameras and lenses. *IEEE Journal of Robotics and Automation*, RA-3(4):323–344, 1987.
- [151] E.A. Tschirren, J. and Hoffman, G. McLennan, and M. Sonka. Airway tree segmentation using adaptive regions of interest. In *SPIE Medical Imaging*, volume 5369, pages 117–124, San Diego, CA, USA, 2004.
- [152] K. Tsushima, S. Sone, T. Hanaoka, F. Takayama, Honda T., and K. Kubo. Comparison of bronchoscopic diagnosis for peripheral pulmonary nodule under fluoroscopic guidance with CT guidance. *Respiratory Medicine*, 100:737–745, 2006.
- [153] M. Urschler and H. Bischof. Assessing breathing motion by shape matching of lung and diaphragm surfaces. In *Medical Imaging 2005: Physiology, Function, and Structure from Medical Images*, volume 5746, pages 440–52, San Diego, CA, USA, 2005.
- [154] D. J. Vining, K. Liu, R. H. Choplin, and E. F. Haponik. Virtual bronchoscopy. Relationships of virtual reality endobronchial simulations to actual bronchoscopic findings. *Chest*, 109:549–553, Feb 1996.
- [155] H. Wang, L. Dong, J. O'Daniel, R. Mohan, A. Garden, K. Ang, D. Kuban, M. Bonnen, J. Chang, and R. Cheung. Validation of an accelerated 'demons' algorithm for deformable image registration in radiation therapy. *Phys. Med. Biol.*, 50:2887–2905, 2005.
- [156] I. Wegner, J. Biederer, R. Tetzlaff, I. Wolf, and H. P. Meinzer. Evaluation and extension of a navigation system for bronchoscopy inside human lungs. In *Medical Imaging 2007: Visualization and Image-Guided Procedures*, volume 6509, San Diego, CA, USA, 2007.
- [157] Ingmar Wegner, Ralf Tetzlaff, Juergen Biederer, Ivo Wolf, and Hans-Peter Meinzer. An evaluation environment for respiratory motion compensation in navigated bronchoscopy. In *Medical Imaging 2008 - Visualization, Image-Guided Procedures, and Modeling*, volume 6918, San Diego, CA, United states, 2008.

- [158] G. M. Weiner, K. Schulze, B. Geiger, H. Ebhardt, K. J. Wolf, and T. Albrecht. CT bronchoscopic simulation for guiding transbronchial needle aspiration of extramural mediastinal and hilar lesions: initial clinical results. *Radiology*, 250:923–931, Mar 2009.
- [159] W. Weiss. Tumor doubling time and survival of men with bronchogenic carcinoma. *Chest*, 65:3–8, 1974.
- [160] Gary. Welch and Gary Bishop. An Introduction to the Kalman Filter. In *SIGGRAPH 2001 course 8. Computer Graphics, Annual Conference on Computer Graphics & Interactive Techniques*. ACM Press, Addison-Wesley, Los Angeles, CA, USA (August 12-17), 2001.
- [161] L. Weruga, J. Morales, L. Nunez, and R. Verdu. Estimating volumetric motion in human thorax with parametric matching constraints. *IEEE Trans. Med. Imag.*, 22:766–772, 2003.
- [162] Onno Wink, Wiro J. Niessen, and Max A. Viergever. Fast delineation and visualization of vessels in 3-d angiographic images. 19(4):337–346, April 2000.
- [163] K. H. Wong, J. Tang, H. J. Zhang, E. Varghese, and K. R. Cleary. Prediction of 3d internal organ position from skin surface motion: results from electromagnetic tracking studies. In *Medical Imaging 2005: Visualization, Image-Guided Procedures, and Display*, volume 5744, pages 879–87, San Diego, CA, USA, 2005.
- [164] Mason Woo, Jackie Neider, Tom Davis, and Dave Shreiner. *OpenGL Programming Guide Third Edi*. Addison-Wesely, 1999.
- [165] Zhiyong Xie, Lydia Ng, and J. C. Gee. Two algorithms for non-rigid image registration and their evaluation. In *Medical Imaging 2003. Image Processing*, volume 5032, pages 157–64, San Diego, CA, USA, 2003.
- [166] S. Xu, J. Kruecker, B. Turkbey, N. Glossop, A. K. Singh, P. Choyke, P. Pinto, and B. J. Wood. Real-time MRI-TRUS fusion for guidance of targeted prostate biopsies. *Comput. Aided Surg.*, 13:255–264, Sep 2008.
- [167] S. Yamamoto, K. Ueno, F. Imamura, H. Matsuoka, I. Nagatomo, Y. Omiya, M. Yoshimura, and Y. Kusunoki. Usefulness of ultrathin bronchoscopy in diagnosis of lung cancer. *Lung Cancer*, 46:43–48, 2004.
- [168] Z. Yaniv, R. Stenzel, K. Cleary, and F. Banovac. A realistic simulation framework for assessing deformable slice-to-volume (CT-fluoroscopy/CT) registration. In *Medical*

Imaging 2006: Visualization, Image-Guided Procedures, and Display, volume 6141, pages 1–8, San Diego, CA, USA, 2006.

- [169] Z. Yaniv, E. Wilson, D. Lindisch, and K. Cleary. Electromagnetic tracking in the clinical environment. *36(3):876–92*, March 2009.
- [170] Ziv Yaniv and Kevin Cleary. Fluoroscopy based accuracy assessment of electromagnetic tracking. In *Medical Imaging 2006: Visualization, Image-Guided Procedures, and Display*, volume 6141, San Diego, CA, United states, 2006.
- [171] D. F. Yankelevitz, A. P. Reeves, W. J. Kostis, B. Zhao, and C. I. Henschke. Small pulmonary nodules: volumetrically determined growth rates based on CT evaluation. *Radiology*, 217:251–256, Oct 2000.
- [172] Kun-Chang Yu, W. E. Higgins, and E. L. Ritman. 3d model-based vascular tree analysis using differential geometry. In *2004 2nd IEEE International Symposium on Biomedical Imaging: Macro to Nano*, pages 177–80, Arlington, VA, USA, 2004.
- [173] Y. Yuan, T. Matsumoto, A. Hiyama, G. Miura, N. Tanaka, T. Emoto, T. Kawamura, and N. Matsunaga. The probability of malignancy in small pulmonary nodules co-existing with potentially operable lung cancer detected by CT. *European Radiology*, 13:2447–2453, 2003.
- [174] E.A. Zerhouni, F.P. Stitik, S.S. Siegelman, D.P. Naidich, S.S. Sagel, A.V. Proto, J.R. Muhm, J.W. Walsh, C.R. Martinez, Heelan T.R., P. Brantley, and R.E. Bozeman. CT of the pulmonary nodule: a cooperative study. *Radiology*, 160:319–327, 1986.
- [175] Z. Zhang. A flexible new technique for camera calibration. *IEEE Transactions on Pattern Analysis and machine Intelligence*, 22(11):1330–1334, 2000.
- [176] B. Zheng and J.K Leader. Automated detection and quantitative assessment of pulmonary airways depicted on CT images. *Medical Physics*, 34(7):2844–2852, 2007.

CURRICULUM VITAE

TIMOTHY SOPER

mail: 314 NE 56th St.
Seattle, WA 98105
e-mail: tim_d_soper@yahoo.com

EDUCATION

- 2009 UNIVERSITY OF WASHINGTON, SEATTLE, WA
Doctor of Philosophy in Bioengineering, September 2009 (expected)
Thesis: A Navigation System for an Ultrathin Scanning Fiber Bronchoscope
in the Peripheral Airways
- 2001 UNIVERSITY OF CALIFORNIA, SAN DIEGO, LA JOLLA, CA
Bachelor of Science in Bioengineering, June 2001
Graduate with Honors

EMPLOYMENT HISTORY

- 2002–2009 Graduate Research Appointment in Bioengineering Department, University of
Washington, Seattle, WA
- 2000–2002 Research Engineer, Metrixion, San Diego, CA
- 1998–2000 Machinist Assistant, Scripps Institute of Oceanography, La Jolla, CA

ACADEMIC EXPERIENCE

Human Photonics Laboratory, University of Washington, Seattle, WA

- Developed a novel tracking methodology for an ultrathin bronchoscope using an electromagnetic sensor and 2D/3D registration of CT-reconstructed and video images.
- Designed and implemented user interface software for a bronchoscopic guidance system.
- Characterized respiratory induced motion of airways in swine by deformable image registration of chest CT images.

- Planned and staged first animal studies investigating *in vivo* performance of an ultrathin bronchoscope.

Radiology Department, University of Washington, Seattle, WA

- Developed automated pattern classification and quantitative evaluation of Interstitial Pulmonary Fibrosis in CT scans based on expert classification.

JOURNAL PUBLICATIONS

- Soper, T.D. Haynor, D.R., Glenny, R.W., and Seibel, E.J. (2009) In Vivo Validation of a Hybrid Tracking System for Navigation of an Ultrathin Bronchoscope within Peripheral Airways, *IEEE Transactions in Biomedical Engineering* (accepted).
- Seibel, E.J., Soper, T.D., Johnston R.S., and Glenny, R.W. (2005) Ultrathin laser scanning bronchoscope and guidance system for the peripheral lung, *Lung Cancer*, vol. 49, S162-S162 (2005).

CONFERENCE PROCEEDINGS (ORAL)

- Soper, T.D. Haynor, D.R., Glenny, R.W., and Seibel, E.J. (2009) Tracking an ultrathin bronchoscope to reach peripheral nodules with laser-based diagnostics, *13th World Conference on Lung Cancer*, August- 2009, San Francisco, USA. (in press)
- Soper, T.D., Haynor, D.R., Glenny, R.W., and Seibel, E.J. (2009) Validation of CT-video registration for guiding a novel ultrathin bronchoscope to peripheral lung nodules using electromagnetic tracking, *Medical Imaging 2009: Visualization, Image-Guided Procedures, and Modeling*, Proc. SPIE 7261:72610C-1-13.
- Seibel, E.J., Soper, T.D., Haynor, D.H., and Glenny, R.W. (2008) 1-mm video bronchoscope with future laser diagnostics and therapies, *Proceedings from the 15th World Congress for Bronchology and 15th World Congress for Bronchoesophagology*, March 30 – April 2, 2008, Tokyo, Japan, 143-149.
- Soper, T.D., Haynor, D.R., Glenny, R.W., and Seibel, E.J. (2007) A model of respiratory airway motion for real-time tracking of an ultrathin bronchoscope. *Medical Imaging 2007: Physiology, Function, and Structure from Medical Images*, ed. A. Manduca & X.P. Hu, Proc. SPIE vol. 6511: 65110M-1-12.
- Atmosukarto, I., Soper, T.D., Glenny, R.W., Seibel, E.J., and Shapiro, L.G. (2007) An interactive 3D user interface for guided bronchoscopy. *Medical Imaging 2007: Visualization and Image-Guided Procedures*, ed. K.R. Cleary & M.I. Miga, Proc. SPIE vol. 6509: 65091G-1-13.

CONFERENCE PROCEEDINGS (POSTER)

- Atmosukarto, I., Soper, T.D., Glenny, R.W., Seibel, E.J., and Glenny, R.W. (2005). Interactive 3D Interface for Guiding an Ultrathin Catheterscope in the Peripheral Lung, presented at: *ACM Symposium on User Interface Software and Technology (UIST)*.
- Seibel, E.J., Soper, T.D., Johnston, R.S., Glenny, R.W. (2005) Ultrathin laser scanning bronchoscope and guidance system for peripheral lung, presented at: 11th World Conference on Lung Cancer, Barcelona, Spain, July- 2005

PATENTS

US11009699 Catheterscope and 3D Guidance Interface System (*filed 12/2004, awaiting issue*)

US11342074 Catheterscope and 3D Guidance Interface System (*filed 01/2007, awaiting issue*)

US11465988 Optical Fiber Scope With Both Non-Resonant Illumination and Resonant Collection/Imaging for Multiple Modes of Operation (*filed 08/2006, awaiting issue*)

HONORS AND AWARDS

2009 Invited Speaker, at the Canary Foundation Quarterly Meeting. February 12, 2009, Woodinville, WA

2005 Recipient of the Bioengineering in Cardiology Training Grant, University of Washington, Seattle, WA

2005 Invited Speaker, An ultrathin laser scanning fiber endoscope for diagnosis and treatment of disease in peripheral airways at 16th International Society for Laser Surgery in Medicine (ISLSM), September 2005, Tokyo Japan.